Title
Development and Translation of 3D Dynamic Hyperpolarized 13C-MR Metabolic and Perfusion Imaging - From Mice to Patients

Permalink
https://escholarship.org/uc/item/7rn0d6p7

Author
Chen, Hsin-Yu

Publication Date
2017

Peer reviewed|Thesis/dissertation

Development and Translation of 3D Dynamic Hyperpolarized ^{13}C-MR Metabolic and Perfusion Imaging - From Mice to Patients

by

Hsin-Yu Chen

DISSERTATION

Submitted in partial satisfaction of the requirements for the degree of

DOCTOR OF PHILOSOPHY

in

Bioengineering

in the

GRADUATE DIVISION

of the

UNIVERSITY OF CALIFORNIA, SAN FRANCISCO

AND

UNIVERSITY OF CALIFORNIA, BERKELEY

Acknowledgments

First and foremost, I would like to thank my PI and mentor, Dr. Dan Vigneron. Dan created an open and collaborative environment that allowed me to work together with this great research team at UCSF on all the exciting patient and preclinical studies. Dan showed me the right attitude toward scientific research. I was never blamed for a rookie mistake, a broken instrument, or an experiment that didn't work out. Instead, Dan always encouraged me to try harder. "If you don't break things, it means you are not using it," as he always says. Dan also taught me a lot on how to present science in a clear and concise manner, and as importantly, he ensured that I can focus on my work without ever having to worry about the funding situation.

I am also indebted to Dr. John Kurhanewicz, who not only shares his great insight and in-depth knowledge about prostate cancer, but invested a serious amount of time editing and rewriting my TRAMP imaging manuscript as well as many abstracts.

I greatly appreciate Dr. Bob Bok for his endless patience with all the help on animal studies; especially with the extremely challenging mouse catheterization. Bob is also a great trainer who taught me all about lab animal handling and care.

I wanted to thank Dr. Peder Larson for all the help with technical aspects of MRI - pulse sequences, reconstruction and dynamic modeling. Peder's suggestion and feedback about my research was invaluable.

Finally, I need to give thanks to my Lord, for He is good; His love endures forever. Pursuing a PhD is a long and arduous journey. There are times of joy, times of laugh, times of frustration, and times of tears. But even though I walked through the darkest valley, I fear no evil - I know that He watches over me every step of the way.

Abstract

Hyperpolarized carbon-13 (HP-^{13}C) is emerging as a powerful new molecular imaging technique utilizing specialized instrumentation and dynamic nuclear polarization (DNP) to provide a signal enhancement of over 5 orders of magnitude. HP-^{13}C MRI has made possible quantitative detection of metabolism and perfusion *in vivo* with ^{13}C-labelled biomarkers, which are safe, non-radioactive and nontoxic. Prostate cancer is the second deadliest cancer in US men, and has become a healthcare problem worldwide. A major challenge in the clinical management of prostate cancer is to determine its aggressiveness.

Through this dissertation project, a 3D dynamic compressed sensing MRSI technique was advanced from preclinical imaging to phase II clinical trial prostate cancer research. I conducted simultaneous metabolic and perfusion imaging on a transgenic mouse model of prostate cancer (TRAMP) using co-polarized ^{13}C pyruvate and urea. Pyruvate to lactate flux (k_{PL}) was significantly higher ($p<0.001$, 0.056 ± 0.005 versus 0.019 ± 0.001 sec^{-1}) for high- versus low-grade TRAMP tumors, urea AUC significantly reduced ($p<0.01$, 640 ± 94 versus 1407 ± 221 AU), while k_{trans} significantly increased ($p<0.01$, 358 ± 38 versus 180 ± 24 ml/dL/min). The HP-^{13}C MRI outcomes strongly correlates with histological, gene expression and LDHA activity findings.

Translation from mice to humans requires overcoming challenges of larger imaging volume, reduce peak RF power, and decreased sensitivity. These challenges

were addressed by designing new RF pulses that reduced 67% peak power, and transitioning from DSE to FID acquisitions without SNR loss. The improved sequence allows $0.5cm^3$ spatial and 2s temporal resolution, and enables reproducible human prostate acquisitions. "Goodness" of dynamic models was compared using Akaike's information criteria. Quantitative accuracy was improved using a B_1-insensitive variable flip angle scheme. Also investigated was the impact of pulse sequence design and parameter on k_{PL} estimation.

New sampling patterns are proposed for larger coverage or finer resolution, and an SVD-based algorithm was applied to allow parallel reconstruction of multichannel brain data. Finally, I investigated the response of androgen deprivation therapy from a prostate cancer patient, and found substantial decrease in k_{PL} , which indicates the clinical potential of quantitative 3D dynamic HP-^{13}C MRI for the detection of early treatment response.

Table of Contents

Table of Figures

Chapter 1 Introduction

This dissertation describes my research developing new bioengineering techniques, and applying such new technique to biomedically-relevant preclinical and clinical patient imaging research studies.

Hyperpolarized ^{13}C (HP-^{13}C) is emerging as a powerful new imaging technique that utilizes specialized instrumentation and an approach called dynamic nuclear polarization (DNP) to provide a signal enhancement of over 5 orders of magnitude (1,2). Meanwhile, the HP-^{13}C-labelled molecular probes are safe, endogenous and nonradioactive. The Warburg effect, as described by Otto Warburg half a century ago, states that high LDH isoenzyme activity drives high lactate production in cancers (3,4). Particularly, prior studies suggest that the pyruvate-to-lactate conversion in prostate cancer is strongly correlated to the aggressiveness of prostate cancer (5,6). By injecting HP-^{13}C pyruvate and observing its conversion to lactate, such change of metabolism can be observed with high SNR, which translates to good spatial, spectral and temporal resolutions. Overall in these graduate studied, I sought to develop new bioengineering techniques using HP-^{13}C MRI in order to establish a non-invasive way of assessing prostate cancer aggressiveness in patients. The background for this dissertation research, including the hyperpolarized ^{13}C techniques and prostate cancer, is outlined in Chapter 2.

I applied this new technique to prostate cancer, which has become the second deadliest cancer in men in the US, and is a major healthcare problem

worldwide. In 2015, approximately 220,000 cases were diagnosed in the US (that is 1 out of 6 men), and more than 27,000 men died of prostate cancer(7). A tremendous challenge for the clinical management lies in the diversity of prostate cancer, which leads to a wide variety of treatment options – from the aggressive surgical and focal therapies to the so-called "active surveillance" used for indolent disease(8-10).

The main contribution of this work was to develop and test 3D dynamic HP-^{13}C acquisition methods for quantitative assessment of prostate cancer in preclinical models, and to translate such methods for robust clinical prostate cancer imaging with high spatiotemporal resolution. My dissertation includes in chapters 3-6, research reports consisting of published manuscripts, those under review process, or in preparation for submission.

In Chapter 3, I applied the 3D dynamic HP-^{13}C MRSI(11,12) in order to assess the prostate cancer aggressiveness in transgenic mouse with prostate cancer (TRAMP). Previously, high lactate production has been reported in TRAMP models, and the lactate/pyruvate ratio correlated to the histological grading data(5). However, no prior HP-^{13}C study dynamically imaged cancer metabolism and perfusion in 3D. This chapter described the first study that injected co-polarized HP 1-[^{13}C] pyruvate and [^{13}C] urea, in order to simultaneously image metabolism and perfusion in five-dimensions (3 spatial, 1 temporal and 1 spectral). The technical advancement on the acquisition side was an inclusion of many previous efforts into one final, complete pulse-sequence. These designs include the RF excitation pulse that features multiband spectral-spatial profile for independent excitation of each

metabolic compound (12), and a variable flip angle scheme that ensured efficient usage of magnetization (13). The adiabatic double spin-echo pulses were applied to refocus off-resonance effects and regulate phase for reconstruction (14). The readout was a compressed-sensing EPSI with random blips encoding in the phase encode (x-y) direction to achieve rapid 3D dynamic acquisition (15). I imaged (N=20) TRAMP mice with high- or low-grade tumor and found high correlation between the HP-^{13}C metabolism and the histochemical, gene expression and enzyme activity assays. Significantly higher pyruvate-to-lactate conversion rates (k_{PL}) were found in high-grade tumors, which correlated well with the high LDH expression and activity. Significantly reduced urea distribution was also found in high-grade, in agreement with the highly hypoxic IHC assay. Metabolism-perfusion mismatch in high-grade tumor can be an indication of more aggressive cancer phenotype and thus poor prognosis. The animal data showed great potential of this 3D dynamic imaging method for clinical translation.

In the project descried in Chapter 4, I investigated the improvements needed on experimental setup, sequence design, acquisition and reconstruction to translate the 3D dynamic method for clinical prostate cancer imaging. The key translational challenges were larger imaging volume, reduced peak RF power for the human RF exciter, and increased B_1 field inhomogeneity. First, new spectral-spatial pulses were designed that significantly decreased the required peak RF power. FID acquisition mode was applied, DSE refocusing pulses were removed, and spatial resolution was optimized to fit human prostate. Secondly, phantom testing and animal studies were conducted to investigate SNR and quantitation in the context of

clinical setup and modified 3D CS-EPSI sequence. I found that the FID acquisition mode was not only less susceptible to reduced transmit power and B_1 inhomogeneities, but provided comparable SNR performance to the DSE acquisition. Moreover, increasing the imaging volume did not deteriorate, and even improved, the *in vivo* image quality and SNR from animal studies, suggesting that the 3D CS-EPSI acquisition was robust to clinical translation with modification of sequence design and parameters. It also demonstrated the scalability in acquisition, reconstruction and quantitative analysis.

For the research in Chapter 5, I focused on quantitative methods for estimation of cancer metabolism and perfusion. As is evident from human and animal HP-^{13}C studies, quantitation of *in vivo* pathophysiology and pharmacokinetic parameters provide invaluable information on cancer aggressiveness and likely clinical outcomes. Here I proposed a design strategy for variable flip angle schedule that, as compared to prior methods, is substantially less sensitive to B_1 field inhomogeneities, while retaining the desirable characteristics of previous designs such as SNR. This scheme was validated through simulations, animal studies, and finally applied on patient exams with excellent SNR performance. Secondly, good kinetic models and fitting are also crucial to optimally extract information from the temporal evolution of HP-^{13}C signal. I compared the "goodness" of different kinetic modeling strategies for k_{PL} using datasets from clinical and preclinical studies. Lastly, MR acquisition methods may also introduce systematic factors into quantitation. Here I identified and investigated several sequence components and design parameters that can impact k_{PL} estimation on the acquisition end. These

factors are especially important in the context of clinical translation, where sequence modification are commonly needed for transmit power and B_1 homogeneity considerations.

Chapter 2 Background

2.1 Introduction to Hyperpolarized ^{13}C MRI

2.1.1 Introduction to Nuclear Magnetic Resonance

Many atoms with odd numbers of protons possess an intrinsic quantum property called *nuclear spin(16,17)*. Atom nuclei, such as ^{1}H, ^{13}C, ^{31}P and ^{35}Cl, that have an angular momentum **I**, enable observation via nuclear magnetic resonance (NMR) absorption spectra. First I use proton(^{1}H), the most commonly used nucleus for NMR, as an example. Proton has two spin states, which are 1/2(spin-up) and -1/2(spin-down). When no external magnetic field present, the spin population are aligned randomly, making the net magnetic moment μ zero. However, when an external magnetic field B_0 is present, the two spin states no longer have a same energy and the resulting energy difference causes more spins to align parallel with B_0, creating a net magnetic moment vector. These spins "resonate" at a specific frequency called Larmor frequency ω, which is defined as

$$\omega = \gamma B_0.$$

where γ is the gyromagnetic ratio of the nucleus. In another word, when a radiofrequency pulse B_1 is applied right at the Larmor frequency, the spins will be excited by the pulse, and emit a radiofrequency wave that can be picked up by NMR

detectors. Such magnetic resonance phenomenon forms the basis of modern NMR spectroscopy and MRI imaging. The most commonly used nucleus is proton, since humans consist of 70% water, and so do many other living organisms. The abundance of proton provides a strong signal for NMR detection.

MRI has become a standard diagnostic modality that is widely available in medical center and institutions around the world. MRI has excellent soft tissue contrast and can be advantageous for imaging regions such as brain, abdomen and pelvis. Many specialized techniques and applications have been developed for MRI. For example, MR angiography(18,19), functional MRI(20,21), MR-guided ultrasound(22,23), MR spectroscopy(24,25) and diffusion MRI are some advances used clinically and/or for scientific research.

2.1.2 Physics Concepts of Dynamic Nuclear Polarization
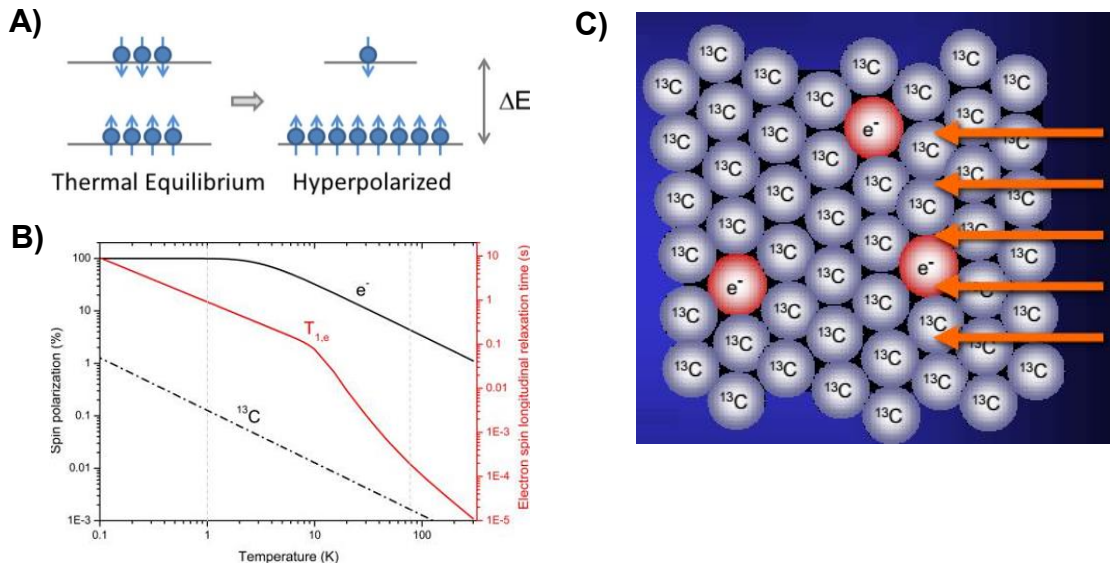
Figure 2.1 A) The DNP technique transiently transforms the nuclear spin into an excited state, giving more than 10,000x SNR enhancement compared to thermal equilibrium. B) Illustration of electron and ^{13}C nuclear polarization as a function of

*temperature. The DNP process is most efficient with subkelvin temperature. (26) **C)** DNP utilizes Nuclear Overhauser Effect to transfer polarization from free radical electrons to the ^{13}C nuclei.*

Carbon is the fourth abundant chemical atom in the universe. A fundamental element that composed all organic molecules, it is said to be the basis of life. The capability to image carbon using magnetic resonance is a gateway to understanding organic phenomena of living systems, for instance, physiology, metabolism, biochemical processes, and even diseases such as cancer. Approximately ~20% of weight in human body is carbon. Also, 99% of the carbon is the MR-inactive ^{12}C nucleus due to its natural abundance, and only 1% of the carbon is the detectable ^{13}C. Moreover, the gyromagnetic ratio of carbon is about 1/4 compared to proton, further limiting the sensitivity of ^{13}C MRI.

Recently, the emerging technique of dissolution dynamic nuclear polarization (DNP) has enabled the new molecular imaging approach known as hyperpolarized $^{13}C(HP-^{13}C)$ NMR spectroscopy and HP-^{13}C MRI. DNP is a nuclear-physics process which increases the nuclear spin polarization by up to 50,000 fold or more compared to that of thermal state (Figure 2.1A)[1,2]. Back in 1953, Albert Overhauser proposed the theoretical phenomena where nuclear polarization can be transferred from one spin species to another via cross-relaxation[27,28]. More specifically, he hypothesized that the nuclear spin can be enhanced when the conducting electrons are irradiated by a microwave source in some metals, which is now known as the Nuclear Overhauser Effect.

The modern DNP process is build off the concepts of Nuclear Overhauser Effect. First, the subject solid-state compound is "doped" with free radicals with

their unpaired electron spins. The electrons are driven to high polarization state when irradiated by a microwave source under an external magnetic field, and the polarization was transferred from radicals to the subject compound. Such polarization and transfer process is most efficient under very low temperature, typically below 1K, where the electron polarization can reach ~100%, and a long relaxation T_1 for both electrons (10-100s) and the solid-state compound (>1000s), as illustrated in Figure 2.1(B). Another factor that affects the polarization level is the magnetic field strength, and it is shown that 4.6-5T field optimizes the polarization(1,26,29).

The second step of dissolution DNP is dissolving the solid-state compound using superheated water. The dissolution process yields a solution of the hyperpolarized compound at body temperature, and is available for direct injection into preclinical or clinical subjects. The dissolution DNP process was first demonstrated by Ardenkjaer-Larsen et al in 2003(1). Since then, several models of polarizers has been developed for HP-^{13}C MRI studies, and strong polarization level has been demonstrated on many ^{13}C-labelled compounds by optimizing the polarizer design and polarization conditions.

2.1.3 Polarizer Instruments for Clinical and Preclinical DNP

A)

B)
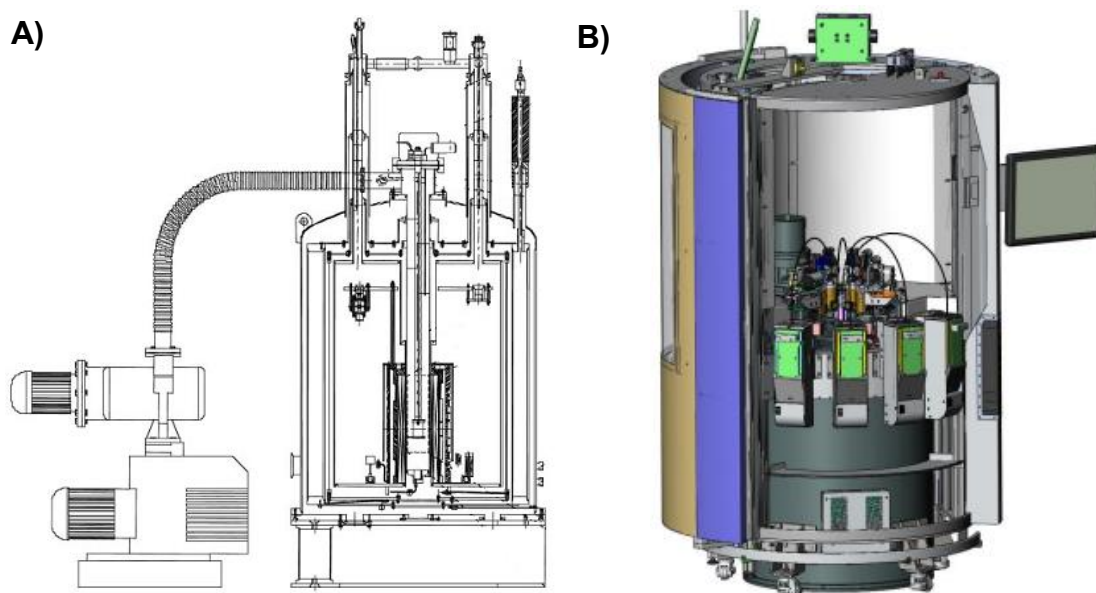
Figure 2.2 *Here some DNP polarizer instruments are depicted **A)** The prototype alpha polarizer is the pioneer dissolution DNP instrument. Its design combined ease-of-use and reliability, and was and still is a workhorse for both in vitro and in vivo animal studies. **B)** The Clinical Spinlab polarizer features paralleled polarization. With the sterile fluid path and QC system, it was designed for human injection.*

Several models of polarizers have been developed since the advent of dissolution DNP. The aim of each design had been to reach higher polarization, paralleled polarization of multiple samples, larger quantity per sample, sterilization of the DNP process, and the ability to produce HP-^{13}C tracers with robustness. Ultimately, the biomedical goal of this research is to perform HP-^{13}C MR studies using dissolution DNP on human subjects in the clinical setting to benefit patient care.

The earliest version of the dissolution DNP polarizer was described by Ardenkjaer-Larsen et al[1], as shown in Figure 2.2(A). The "alpha" system consists

of a cryostat, a narrow-bore high field magnet, a variable temperature insert (VTI), and a microwave source. The HP-^{13}C prep was first loaded into a sample cup, which was lowered into the VTI, to the center of the magnet bore. The cryogenic temperature in VTI was maintained at ~1.3 K by the supply of liquid helium at low pressure to achieve high polarization efficiency. The sample was constantly irradiated by the microwave source during the buildup process, and a small NMR coil allows monitoring of polarization process. Prior to dissolution, the sample was lifted out of the helium bath. Subsequently, boiling-hot solvent was rapidly discharged into the solid-state sample to quickly dissolve and mix, and the HP-^{13}C solution was dispensed into a receiver flask.

Since the first models built, the "alpha" polarizer was made into a commercial product (HyperSense, Oxford Instruments, UK) and has been used globally by many research sites for HP-^{13}C studies. While the HyperSense polarizer is a workhorse for *in vitro* NMR studies and preclinical animal scans, the demand for clinical translation of the HP-^{13}C MRI calls for a new instrument design that can produce clinical dose HP-^{13}C boluses that is safe for human injection.

A prototype polarizer for clinical HP-^{13}C studies was developed by GE healthcare (Waukesha, WI) (30,31). The polarizer, named SpinLab, has 4 channels for simultaneous buildup of multiple samples (Figure 2.2B). The solid-state sample and dissolution media were packaged into a "fluid path" system, which essentially forms a semi-closed system that is isolated from the polarizer instrument. This allows the fluid path to be prepared in a clean room environment, in order to meet the sterility and safety requirements of investigational new drug (IND) program of

the FDA. While the overall system design is drastically different from the "alpha"

polarizer, the Spinlab instrument retains the essential elements of a hyperpolarizer,

namely a cryostat, a high-field magnet, a microwave source and a NMR buildup

monitor.

Another essential compartment for clinical studies is the quality control (QC)

system. Upon dissolution, the QC system measures key parameters including the

polarization level, solution pH, concentration, temperature and radical

concentration. This allows a pharmacist to determine whether the solution is to be

accepted or rejected for human injection.

The SpinLab polarizer operates on an "airlock" system, which is similar to the

DNP insert on HyperSense. After loading the fluid path into the Spinlab, the cryo vial

that holds solid-state sample was lowered through the airlock into the cryostat for

buildup. The dissolution media, on the other hand, stays in a syringe inside a heater-

pressure chamber, where the liquid is superheated to 130° C. When the dissolution

commences, the cryo vial was lifted from the cryostat, and superheated media was

discharged into the solid-state sample through the inner tube of the fluid path. The

dissolved sample is then chased out via the outer tube to the receiver assembly.

2.1.4 Hyperpolarized ^{13}C Imaging

The development of the dissolution DNP technique provides more than

10,000 fold increase of polarization on ^{13}C-based tracers. The high polarization,

combined with the ease to label ^{13}C onto biochemical molecules, has created a new

field in MRI that previously had not been possible using natural abundance,

thermally-polarized ^{13}C imaging. HP-^{13}C imaging has since become a powerful tool that finds applications as an *in vivo* probe for a wide range of physiological and pathological phenomenon.

One key application of HP-^{13}C MRI is to detect cancer metabolism safely and noninvasively with high spatiotemporal resolution. The Warburg effect, as proposed by Otto Warburg et al. half a century ago, states a biochemical process where cancer cells exhibits high LDH enzymatic activity, which drives highly accelerated conversion of pyruvate to lactate(3,32). Injecting HP [1-^{13}C] pyruvate and imaging the HP lactate production enables the visualization of such cancer metabolism. Nowadays it is widely accepted that cancer metabolism is strongly associated with the survival, growth, progression and metastasis of many types of cancer, and can be a good predictor of cancer aggressiveness (33-35).

Another important physiological parameter in cancer is perfusion. Poor perfusion and hypoxia was known to associate with aggressive tumor phenotypes and poor clinical outcomes (36-38). In high-grade tumor, the rapid cellular export of lactate, in addition to poor perfusion, give rise to an acidic tumor microenvironment. The acidification promotes cancer aggressiveness and metastasis by degradation of extracellular matrix, increasing angiogenesis and inhibiting immune responses.
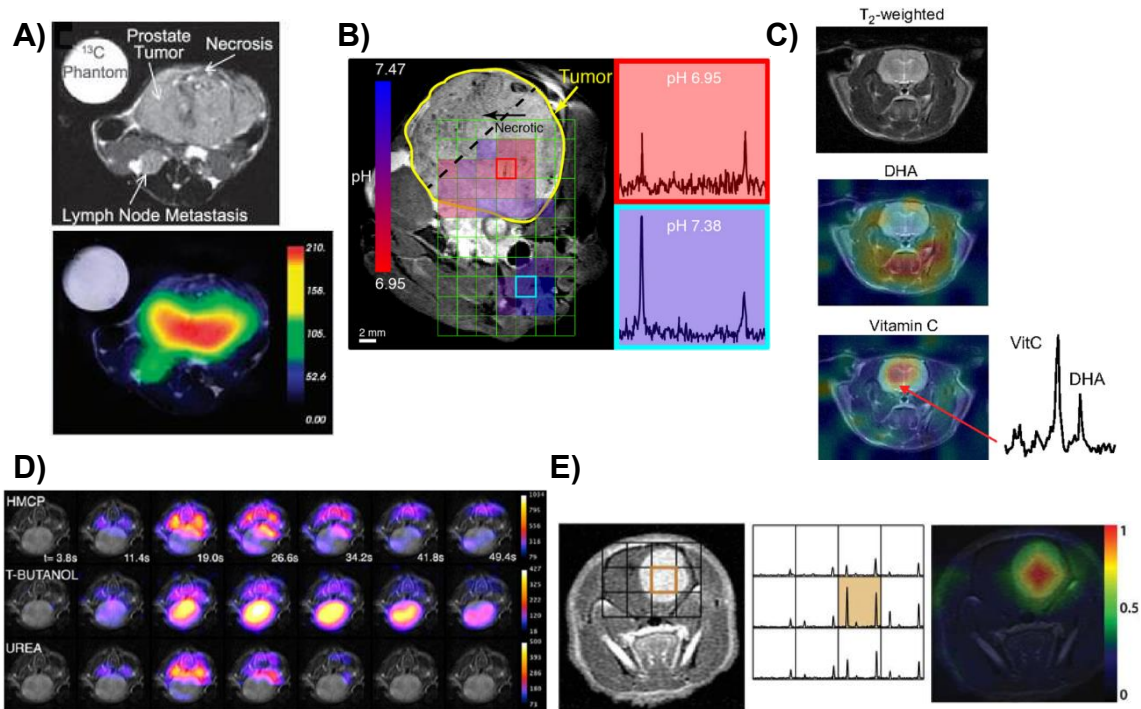
Figure 2.3 *Examples of HP-^{13}C images from prior studies.* **A)** *Lactate map overlaid on T$_2$-w references on a TRAMP tumor (5) .* **B)** *pH imaging of TRAMP tumor using HP-^{13}C bicarbonate buffer suggested acidification of tumor microenvironment. (39)* **C)** *Imaging of in vivo redox potential using HP-^{13}C dehydroascorbate and vitamin C. (40)* **D)** *Perfusion imaging of mouse brain using tripolarized HP-001, t-butanol and urea can be used to differentiated perfusion versus permeability. (41)* **E)** *Lac/pyr map of treated xenograft tumor in rat brain showed significantly altered metabolism. (42)*

A good perfusion tracer has to be metabolically inactive and has low toxicity. Compared to proton perfusion imaging, signals generated by HP ^{13}C tracers is relatively proportional to tracer concentration, with the SNR enhancement by hyperpolarization. Beyond cancer, HP ^{13}C has been applied to renal functional imaging(43,44), brain perfusion(42,45) and cardiac imaging(46,47). Several HP ^{13}C tracers have been investigated for perfusion imaging, such as ^{13}C urea, [^{13}C]HMCP and [^{13}C]t-butanol(41).

The microenvironment has a pivotal role in cancer progression and invasiveness. Several works has reported HP ^{13}C-based pH probe, such as ^{13}C-bicarbonate(39,48,49). The chemical equilibrium between bicarbonate and carbon dioxide is dictated by *in vivo* pH, and the exchange is very rapidly driven by carbonic anhydrase.

$$HCO_3^- + H^+ \leftrightarrow CO_2 + H_2O$$
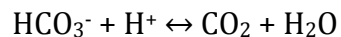
pH value offers invaluable information about changes in tumor microenvironment. The high lactate production and rapid excretion of lactate, combined with poor perfusion creates an acidic microenvironment. Such environment promotes cancer invasiveness by degradation of tumor extracellular matrix, and may induce its chemo-resistance.

Other than its significance in cancer microenvironment, pH is also an important in reflecting pathologic conditions such as ischemia, inflammation and infection. HP-^{13}C probes provide the high SNR for *in vivo* pH imaging which enabled high resolving power.

2.1.5 Imaging Methods for HP-^{13}C MRI

Imaging of HP-^{13}C species is inherently limited by the spin-lattice relaxation (T_1) rate of the ^{13}C-labelled biochemical molecules. For many commonly used molecules in HP-^{13}C MRI, such as pyruvate and lactate, T_1 is primarily limited by chemical shift anisotropy (CSA), and is approximately ~ 60 seconds *ex vivo* in a 3T magnet. CSA is proportional to the square of main field (B_0^2)(50). While dipolar coupling is arguably the most important factor that affects T_1 of ^{13}C compounds,

those molecules with strong dipolar coupling, such as a direct C-H bond on the labelled carbon, will have a very short T_1, and render them unsuitable for HP-^{13}C imaging.
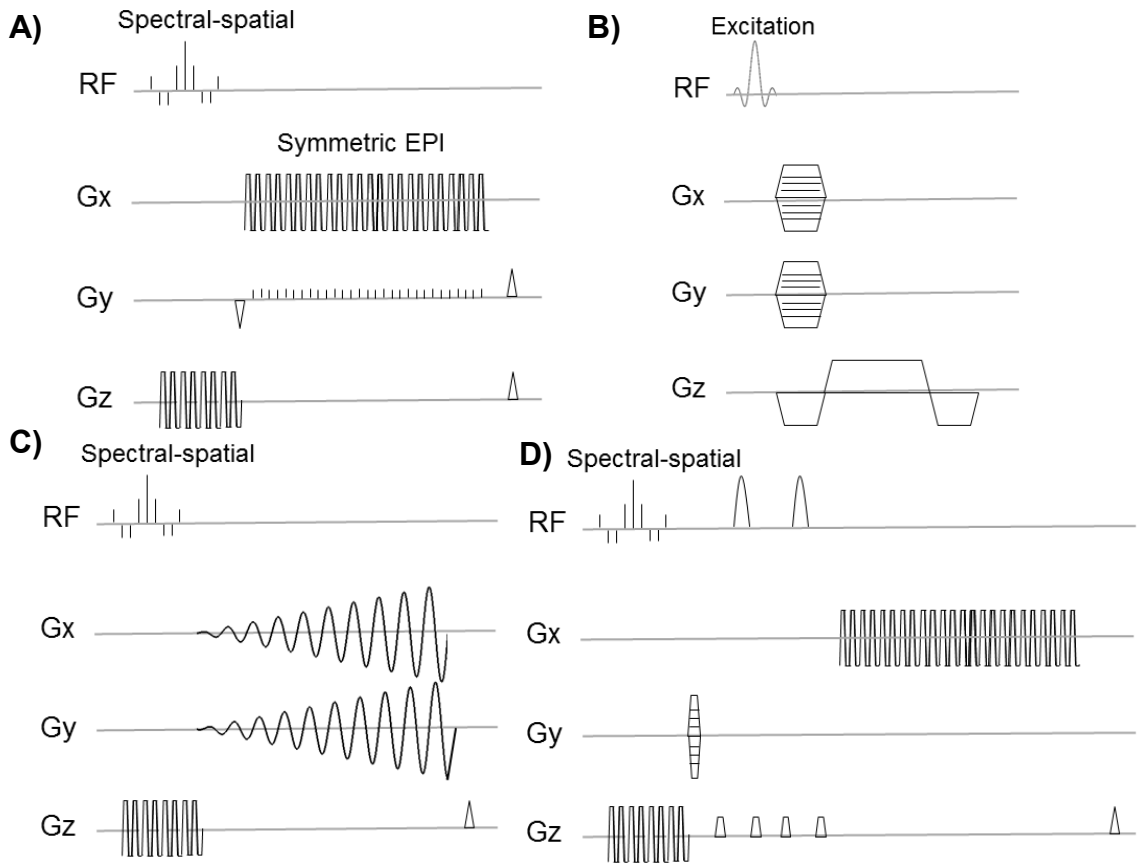
Figure 2.4 *A few types of pulse sequences for rapid HP-13C acquisition as examples. **A)** 2D multislice EPI sequence. **B)** balanced SSFP sequence. **C)** Spiral CSI sequence. **D)** 2D EPSI sequence.*

A variety of acquisition strategies have been proposed for HP-^{13}C MRI used in different applications. One family is the purely imaging-based sequence, such as single-shot or multi-shot echo-planar imaging (EPI, Figure 2.4A) (51,52), multislice spiral sequence (Figure 2.4C) (47), and balanced steady-state free precession

(bSSFP, Figure 2.4B) sequences (53,54). Another family is the spectroscopic-imaging

sequences, also known as chemical shift imaging (CSI), that acquire spatially-

resolved spectroscopy data. Examples of CSI-based sequence include the

conventional phase-encode CSI, the 2D and 3D echo-planar spectroscopic imaging

(EPSI, Figure 2.4D)(55,56), spiral CSI(57,58) and concentric acquisition(59). A

group of specialized acquisition strategy has also been reported, such as

IDEAL(60,61) and k-t spiral sequences (62).

The imaging-based sequences are fast and relatively robust to motion. These

sequences utilize a spectral-spatial excitation followed by readout imaging

gradients. Imaging each metabolite separately means that flip angle scheme can be

designed and optimized individually for each resonance. For the 2D multislice EPI

sequence, the Nyquist ghosting can be reduced by applying a phase correction

derived from a reference ^{1}H scan using the same EPI readout trajectory (52). The

EPI sequence is also relatively robust to off-resonance and gradient trajectory

distortions. The 2D multislice EPI sequence shows excellent performance on both

human and animal trials. The spiral sequence is SNR efficient and less sensitive to

flow and motion (63), making it particular suitable for cardiac imaging. Several

studies have demonstrated imaging of pyruvate, lactate and bicarbonate in porcine

and human heart using the multislice spiral sequence(46,64). The bSSFP sequence,

on the other hand, takes advantage of the long T_2 relaxation times of ^{13}C species to

effectively use magnetization. Just like its proton counterpart, HP-[13]C bSSFP

sequence achieves high SNR efficiency and provides good spatial resolution.

16

Preclinical rat and tumor mice imaging has been demonstrated using bSSFP with high spatiotemporal resolution (44,53).

The spectroscopic imaging technique acquires spectral information for each spatial voxel. Such spectral information reduces the need for *a priori* knowledge or assumptions about the spectral resonances of hyperpolarized compounds. It makes the CSI sequences relatively robust to off-resonances, and the amplitude and shape of each peak can spatially reveal information about the chemical behavior and spin coupling of each compound (65). Moreover, it enables detection of all ^{13}C resonances across the spectral bandwidth, which can potentially reveal secondary or new metabolic pathways. The conventional CSI encodes for each spatial k-space location, which allows for good spectral bandwidth. However, such method requires numerous phase encodes, making it challenging to image dynamically.

One basic way of accelerating spectroscopic imaging can be achieved by interleaving spectral and spatial encoding using techniques such as EPSI and spiral CSI (62). This type of sequence has reduced bandwidth compared to conventional phase-encoded CSI due to the shortened echo-spacing, or effectively a coherent undersampling in the spectral dimension. Fortunately, the sparsity of HP-^{13}C spectrum and a priori knowledge of resonances can be utilized to resolve the peaks even in the presence of spectral aliasing.

An interesting acceleration strategy fully utilizes the a priori knowledge about ^{13}C chemical species to design the undersampling parameters and reconstruction methods. The IDEAL method (61), similar to fat-water DIXON imaging (66), uses spiral readouts with carefully-designed echo time shifting to

encode in the spectral dimension. An FID acquisition was applied separately to extract the spectral prior knowledge. With the predefined HP-^{13}C resonances frequencies, the reconstruction reduces to a matrix inversion problem. A k-t spiral acquisition trajectory further eliminates the need for interleaves, enabling extraction of spatial and spectral information within a single-shot excitation. Reconstruction was performed by jointly solving for spatial and spectral encoding using a similar mathematical theory.

2.1.6 Randomly-undersampled Acquisition and Compressed-sensing Reconstruction for Accelerated HP-^{13}C MRI

Lustig et al, *MRM*, 2007
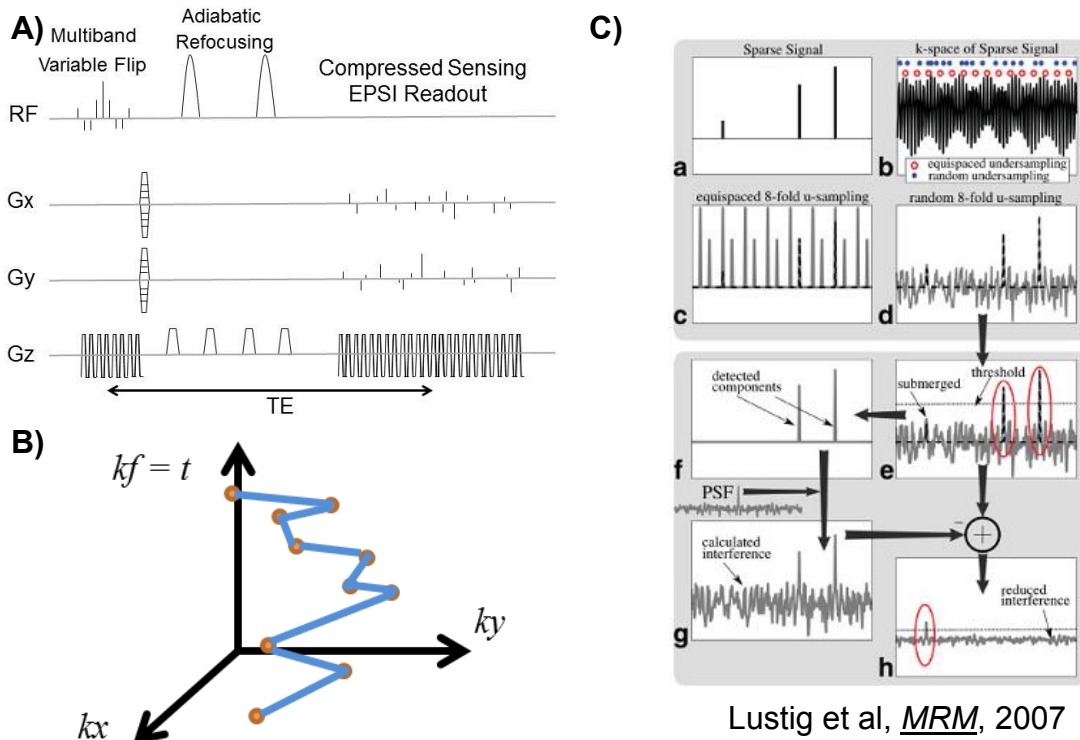
Figure 2.5 A) The 3D dynamic compressed sensing EPSI (3D CS-EPSI) sequence offers 5D acquisition (3 spatial, 1 spectral and 1 temporal) with high spatiotemporal resolution. The sequence features a spectral-spatial RF pulses using variable flip angle scheme and multiband excitation. It was followed by double spin-echo refocusing and

*compressed sensing readout using random blips encoding. **B)** An illustration of k-space trajectory demonstrates the undersampling method by random walk in the kx-ky space. **C)** Illustration of under-sampled reconstruction, reproduced here from Lustig's work. (67)*

Since the first paper of sparsely-sampled MRI by Lustig et al.(67), compressed sensing (CS) has been implemented as a built-in feature for the proton sequences on almost all the commercial MRI scanners. Accelerated acquisition not only means less patient discomfort, but reduces the total cost of scan considering the high MRI operation cost per hour. This fast imaging technique can be particularly advantageous to HP-^{13}C MRI sequence (12,15), where the imaging window is restricted by the inherent hyperpolarized T_1 to about one minute.

Compressed sensing exploits the sparsity in some MR image domains. There are several key requirements to apply the CS, excerpted as follows. 1) The data must be sparse in some domains. 2) Undersampling pattern has to create incoherent aliasing in the sparse-transform domain. 3) A non-linear reconstruction algorithm that enforces both sparsity and data consistency. 4) Sufficient data SNR.

Lustig et al provided an excellent illustration how CS works in their seminal paper(67), which is reproduced here in Figure 2.5(C). A equispaced undersampling creates artifact of wrapped-around and repeated signal peaks. Incoherent undersampling, on the other hand, creates an interference pattern that contains the both the signal and interference component. If the signal is of sparse nature in some domains, the stronger signal peaks can be "detected" using a thresholding. The detected peaks are then applied to back-calculate the interference pattern. The interference pattern can be subtracted from the signal, exposing the weaker signal

peaks (equivalently enforcing data consistency). After a given numbers of iterations, both the strong and weak components can be picked up by CS.

Lustig mathematically formulated the reconstruction algorithm as follows.

$minimize \ \|\Psi m\|_1 \ s.t. \ \|F_u m - y\|_2 < \epsilon$

where m is the image of interest, Ψ is the sparsifying transform, F_u is the undersampled Fourier transform, and y is the measured k-space signal with undersampling.

A 3D compressed-sensing EPSI sequence (3D CS-EPSI), originally developed by Hu et al. (11,15), was used throughout this dissertation(Figure 2.5A). The sparsity criterion is fulfilled by the sparse nature of HP-^{13}C spectrum. Moreover, the continuity in time domain can be converted into sparsity using a wavelet-in-time transform. The incoherent undersampling criterion is fulfilled by a randomly-blipped sampling pattern in the k_x and k_y direction (Figure 2.5B), paired with the flyback EPSI readout that fully samples the k_z-k_f dimensions. An iterative nonlinear sparsity/consistency algorithm enforces L1-minimization on the undersampled dataset. The final criteria call for the SNR, which is consistently at the order of 30 for pyruvate and lactate in TRAMP prostate tumor, compared to the minimum requirement of 3.

A recently published work (68,69) utilizes undersampled phase-encoding, coupled with rapid 2D EPI readout to create a highly accelerated 3D EPI sequence. It was further integrated with multichannel imaging using a SAKE-type calibration-less reconstruction algorithm. A 4 fold undersampled 3D image with FOV = 3.2 x 3.2 x 3.2 (cm), matrix size = 48x48x48 (spatial resolution = 6.7mm isotropic) was

reported using the 3D EPI. Another recent work (53) develops a HP-^{13}C bSSFP

sequence that undersamples in the two phase-encode dimensions. An FOV =

3x3x2.5(cm), matrix size = 20x20x17 dynamic acquisition was reported with 2 fold

undersampling, giving 1.4 s temporal resolution.

Yet another recent work (70) further extended the 2D EPSI sampling pattern

to incorporate a stochastic time delay in addition to the random-blipped

undersampling in k_x-k_y for incoherent undersampling in k-t space. The stochastic

time delay creates a pseudo-long readout time, which effectively increases the

spectral bandwidth. A 3.8x undersampled 2D EPSI was reported with FOV = 24x24

(mm) and matrix size = 8x8 and spectral bandwidth = 5kHz, giving 3 s temporal

resolution.

In general, distributing the random undersampling along more numbers of

dimensions creates higher incoherence. For example, 2 fold undersampling along 3

dimensions creates higher incoherence than 8 fold undersampling in a single

dimension. As incoherence aliasing is a requirement for CS reconstruction scheme,

designing for multiple-dimension undersampling improves CS performance, and

potentially allows for higher undersampling ratio. In the stochastically-delayed 2D

EPSI sequence, the random undersampling was across 4 dimensions (k_x, k_y, k_f,

dynamic). The 3D CS-EPSI sequence has 3 dimensions (k_x, k_y, dynamic), and 3D

bSSFP (k_x, k_y, dynamic) and 3D EPI (k_x, dynamic) each have 3 and 2 dimensions of

undersampling, respectively.

2.2 Prostate cancer

2.2.1 Introduction to prostate cancer

Since the first diagnosis of prostate cancer in the early 1850s, the disease has developed into a serious health clinical management problem facing the US male population, as well as a global healthcare burden. In 2016, an estimated 180,000 new cases of prostate cancer have been diagnosed, and 26,000 men died of the malignancy in the United States(7). Prostate cancer is prevalent in older men, with 6 out of 10 incidences among population over age 65.

Looking at the epidemiology, the incidence of prostate cancer also differs among regions of the world(8). For instance, high incidence is found in North America, Northern and Western Europe, Australia and New Zealand. Lowest incidence is found in Asian regions such as China and Japan. A part of such variation can be accounted for by the difference in population age structure between developed and developing countries. Nevertheless, variation still exists after age standardization.
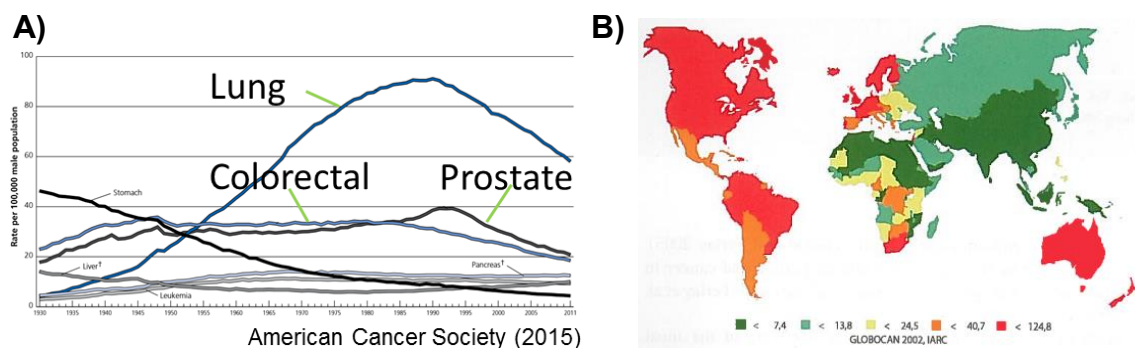
Figure 2.6 A) Prostate cancer is the 2nd most deadly cancer in men. B) Global incidence of prostate cancer by country.

2.2.2 Screening and diagnosis of prostate cancer

Screening of prostate cancer was designed with the goal to improve the clinical outcome by early detection and diagnosis of the malignancy at an early, asymptomatic stage for the population at risk (8,71). The most common measures of prostate cancer screening are serum prostate-specific antigen (PSA) and digital rectal exam (DRE)(72). PSA is a glycoprotein produced by prostate epithelial cells. Elevation of PSA can suggest pathological conditions, where tissue barrier between lumen and capillary is disrupted, allowing higher PSA to be released into the blood. DRE remains a standard clinical practice for prostate cancer diagnosis due to its easy accessibility and usefulness to detect nodules, fibrosis or abnormal masses and asymmetry in prostate. Although DRE detection is limited to posterior and lateral aspects of the prostate gland due to anatomical restrictions, the fact that 85% of prostate malignancy arise from the peripheral zone (PZ) ensures that DRE is still an effective tool. While serum PSA test have lower positive predictive value (PPV) and DRE is low in sensitivity, combination of the two methods has suggested improvements in early detection rate.

The effectiveness of prostate cancer screening remains controversial. Some randomized, multi-site studies found improvement in patient survival at follow-up in subsequent years (73,74); however, some similar studies did not find any significance between the screened and control groups. In general, there is no definitive evidence so far that screening and early treatment reduces mortality.

Despite the controversies, prostate cancer screening programs are implemented in many regions worldwide as a healthcare measure, especially in

developed countries such as US and in Europe, as the incidence rate in these regions are higher than developing countries. The practice and sub-population subjected to screening, however, differs based on the healthcare policies in each country.

2.2.3 Clinical management of prostate cancer

Prostate cancer demonstrates a tremendous biodiversity, and the result is a broad range of clinical management options accordingly. For more indolent diseases, the "active surveillance" or "watchful waiting" approach has been the standard of care, where patients, who do not need active therapy, are closely monitored using measures such as PSA, DRE, and imaging (24,75,76). The monitoring approaches and frequencies depend on symptoms that the patient presents with, and also accounts for other health conditions and chronic diseases, especially among older patients, in order to improve overall life quality and life expectancy. A variety of treatment options are available for more aggressive cancers, including androgen-deprivation therapy (ADT), prostatectomy, focal therapy, radiation therapy, chemotherapy and many more.

ADT is a standard-of-care therapy for metastatic and recurrent prostate cancer. The growth and progression of prostate cancer can be heavily driven by androgens. A variety of strategies has been developed, including inhibiting the production of androgen precursors, inhibition of androgen, androgen receptors, or combination of the above. One common form of chemotherapy targets the luteinizing hormone-releasing hormone (LHRH). This type of drugs works by either serving as a LHRH homolog or antagonist, and in turn inhibits testosterone

production. The anti-androgens, on the other hand, blockade androgens from binding to the androgen receptors on prostate cells (77). The likelihood of developing castration-resistant prostate cancer (CRPC) is high for patients treating with ADT (78).

Radical prostatectomy is the surgical approach to treat localized or locally-advanced prostate cancer. Some common ways for radical prostatectomy includes retropubic prostatectomy, radical perineal prostatectomy, and robotic-assisted laparoscopic prostatectomy (RALP) (79,80). RALP is currently the most common surgical approach in USA, which features significantly less blood loss and pain compared to other types of prostatectomy. Advantage of the surgical approach is the availability of tumor tissue for a comprehensive pathological analysis which is can significantly improve evaluation, staging and prediction of prognosis.

Many more options, such as external beam radiation therapy, chemotherapy and brachytherapy are also often chosen either as a primary treatment or in the context of adjuvant therapy depending on the stage, extent and Gleason score in the clinic (8,76).

2.2.4 Staging and Pathology of prostate cancer

Early diagnosis is an important, if not the most important factor to clinical management of prostate cancer. Following a confirmed diagnosis, assignment of prostate cancer stages on individual patients is the key not only to find out the extent of cancer to predict prognosis, but to evaluate and formulate a most appropriate treatment plan for the patient.

25

The TNM classification system, developed by Union for International Cancer Control (UICC), has been globally accepted as a standard for staging cancer (81). The TNM staging is assigned based on the extent of primary tumor site (T), the regional lymph node involvement (N), and the presence and extent of distant metastatic sites. The information leading toward TNM classification is based on finding from previous clinical exams, physical exam (e.g DRE), lab tests (e.g PSA), biopsy, pathology and imaging, which are used to better define the location, extent and metastasis of prostate cancer.

The Gleason grading system is the most common way to assign pathological grades of prostate cancer (82). The Gleason grade, which provides valuable information regarding cancer prognosis and guiding therapy, was integrated into the classification of cancer stages. The Gleason score consists of the addition of two numbers. The first number represents the differentiation level of the most common pattern (primary) found in tissue biopsy, and the second number being the second most common (secondary) pattern. The differentiation level for each pattern ranges from 1-5, with 1 being the most well- differentiated and 5 being the most poorly- differentiated tissue. For instance, Gleason score 4+3 means the primary pattern is 4, and secondary pattern is 3. The criteria for Gleason score assignment is summarized in Table I (82,83).
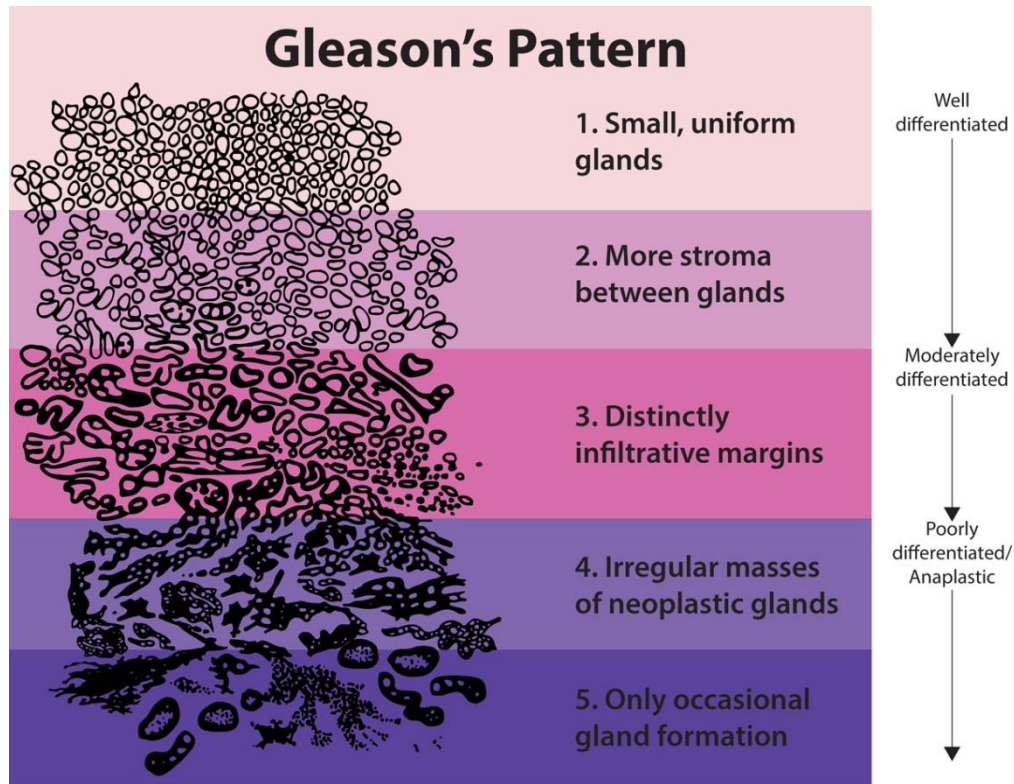
Figure 2.7 *Gleason pattern was defined by the differentiation level of the prostate tumor pathology, with 1 being the most well-differentiated and 5 the most poorly-differentiated pattern. Gleason score is assigned as the addition of most common pattern and second most common pattern.*
https://training.seer.cancer.gov/prostate/abstract-code-stage/morphology.html

Table I.

Gleason pattern	Description
1	Very well-differentiated growth of closely packed but separate, uniform, rounded to oval, medium-sized acini.
2	Circumscribed nodule of small acini, with some variation in size, which are less tightly packed than in pattern 1 and may show minimal peripheral invasion into stroma but never into benign lobules.
3	Glands infiltrating benign lobules and stroma. These glands are discreet microacinar and occasionally macroacinar structures, frequently with irregular contours.
4	High-grade and poorly differentiated

	carcinoma growth, with raggedly infiltrative masses, or chains or cords of malignant epithelial cells. The cellular arrangements can be fused microacinar, cribriform, or papillary.
5	The highest grade, constituting an essentially undifferentiated adenocarcinoma. Glandular architecture is completely lost, and the tumor cells grow in single file, nests, and sheets.

The current clinical practice of prostate biopsy is done using MR-guided transrectal ultrasound (TRUS) (84,85). It consists of transrectal sampling of 10-14 bilateral biopsy cores of prostate tumor tissue. However, the predictive value of biopsy Gleason score still remains controversial. While some studies found high correlations between the biopsy Gleason score and that from radical prostatectomy (RP), others suggest a high percentage of discrepancy between the two (86-88). The discrepancies were more commonly found in low- and moderate- grade patients. Several reasons can possibly account for the discrepancies, including sampling bias, inter-pathologist variability, the borderline features and regions of transition between two grades. Upgrades (46%) were found to be more usual than downgrade (18%) in one study. (87)

Even with the abundance of diagnostic information we can gather on individual patients, including DRE, PSA, biopsy/pathological and imaging data, there's still substantial debate over the accuracy of diagnosis due to the relative high variation and hence the low predictive value. Controversies also exist with the prostate cancer management. The debates partly translate from the limited diagnostic abilities. More important issues stems from the efficacy of treatments, in

addition to side effects and the advances in new type of therapy, such as immune therapy and personalized medicine (89,90). Therefore, in this dissertation research I aimed to advance the clinical HP-^{13}C imaging of prostate cancer, especially the acquisition techniques and quantitation methods. The overall goal of this bioengineering research is to develop non-invasive diagnostic tools for evaluating prostate cancer aggressiveness, in order to help both the clinical process of diagnosis and outlining a treatment plan for individual patients.

2.3 Multi-parametric Imaging of Prostate Cancer

MRI is becoming a standard clinical tool in diagnosis and grading of prostate cancer (76,91). Integrated with other diagnostic tool such as DRE, PSA and TRUS-guided multi-core biopsy, MRI offers visualization of the entire prostate gland, including the central zone (CZ), transition zone (TZ) and peripheral zone (PZ). In this sense, MRI complements other imaging modalities in resolving intra- and periprostatic anatomy. The standard MRI protocol for prostate cancer consists of T$_2$-weighted imaging (Figure 2.8 A,B), diffusion-weighted imaging (DWI, Figure 2.8 D,E) and dynamic contrast-enhanced (DCE, Figure 2.8 F,G) scans. At UCSF, proton spectroscopy (Figure 2.8C) is also a standard imaging practice for prostate patients. This dissertation will focus on the hyperpolarized ^{13}C spectroscopy and imaging, which is shown to be promising for both preclinical and clinical prostate cancer MRI.

2.3.1 Proton Imaging

T_2-weighted sequence provides detailed anatomical information, such as zonal anatomy, prostate capsule, periprostatic soft tissue, and urethra (24,76). Importantly, it also highlights prostatic abnormalities at the same time. Normal prostate PZ tends to have high signal intensity due to its high ductal volume, while the tumor in those regions tend to have lower signal due to higher cellularity and reduced free-water. The low signal is most likely due to the loss of ductal structure of the normal prostate gland. PZ prostate cancer nodules often appears as a round-shaped low signal region; however, central gland tumors tend to be more amorphous with ill-defined margins, and are therefore more challenging to diagnose using T_2-weighted images alone. Moreover, benign prostate hyperplasia (BPH) can exhibit a loss of ductal structure and hypointensity on T_2w images, thereby limiting the sensitivity. Nevertheless, T_2w is still a center piece of prostate cancer imaging, especially for detection of cancer invasion beyond the prostate. One T_2-weighted MRI sequence commonly used in the clinic is T_2-FSE.

DWI detects the microscopic diffusion motion of water molecules. Pathologic conditions may change the normal ductal structure and cellularity in the prostate, thereby changing the diffusion phenomena (76,92). The DWI acquisition is normally done using a single-shot EPI or single-shot FSE sequence in the presence of diffusion gradients. Diffusion is quantified using apparent diffusion coefficient (ADC), with higher ADC indicating higher freely-diffusible water or less dense tissue component.

DCE is a common imaging sequence to detect blood flow, perfusion and permeability (91,93). Gadolinium is a contrast agent that is typically only

extracellular. The injection of Gadolinium-based contrast agents (e.g. Gd-DTPA) enhances the signal intensity in the vasculature and perfused tissue. Pharmacokinetic parameters, such as k_{trans}, can be calculated based on the difference between pre-contrast (without Gd) and post-contrast images.
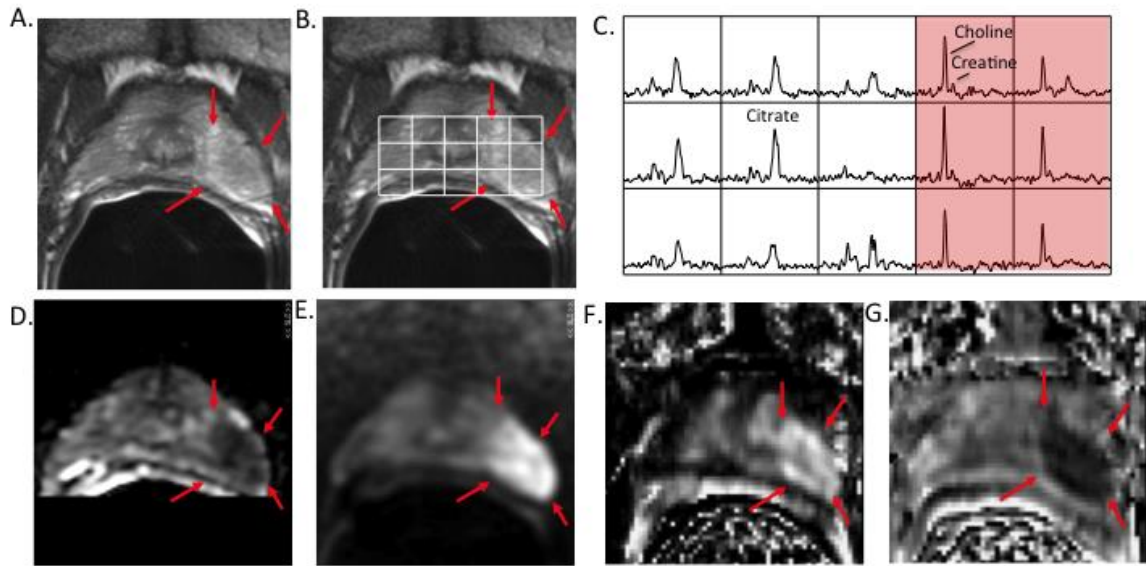
Figure 2.8 *Examples of multiparametric proton imaging of prostate cancer.* *A) and B) depicts T$_2$-weighted images of cancer at left apex. C) Proton spectroscopy suggest higher choline+creatine/citrate ratio in cancer versus contralateral. D) and E) are ADC and high b-values images, showing low ADC and high intensity in high-b maps, respectively. F) and G) shows DCE uptake and washout images. Figures excerpted from Kurhanewicz's review article. (76)*

2.3.2 Proton Spectroscopy

Changes of proton spectroscopic information from benign prostate tissue to cancer involves alteration of both ductal morphology and cellular function. Healthy prostate epithelial cells are known to synthesize and secrete citrate, while the high choline content is associated with prostate cancer. This is due to the high expression

of zinc transporters in the epithelial cells, and zinc in turn suppresses the citrate-degradation enzymes. In cancer, loss of zinc and increased oxidation of citrate elevate the energy production (76,91).

Choline and its derivatives are important for the synthesis of phospholipid membranes, which is strongly linked to tumor growth and metastasis (76). The (Choline+Creatine)/Citrate ratio has been widely accepted as a proton spectroscopic biomarker for prostate cancer, as strong link was found with high CC/C ratio and prostate malignancies (76,91). The acquisition typically utilizes the PRESS + 3D CSI sequence (94,95), where a spatially-resolved spectroscopy is obtained, and the 3D coverage is important to cover the zonal anatomy of the prostate gland, including both the central gland and peripheral zone. Technical challenges of ^{1}H MRSI include air-tissue interface and lipid suppression that requires accurate voxel-selection and magnet shimming.

2.3.3 HP-[13]C Spectroscopy

Hyperpolarized-^{13}C has found a wide range of interest in prostate cancer imaging in both scientific research and potential clinical applications. Ex-vivo bioreactor studies found high lactate production in human prostate tissue, which was driven by high LDH enzymatic activity and increased expression of monocarboxylate transporters MCT1 and MCT4 (6). TRAMP prostate tumor mimics human prostate cancer both pathologically and metabolically. In vivo HP-^{13}C MRSI of TRAMP prostate cancer was able to detect high lactate/pyruvate ratio and high-grade versus low-grade tumor (5).

Furthermore, in 2013, Nelson et al. conducted the first-in-human HP-^{13}C MRSI using new RF coils, improved pulses sequences and clinically-safe polarizer (96). A range of acquisition strategies has been applied, including 1D dynamic MRSI, 2D dynamic MRSI and 3D time-averaged MRSI. Regions of high lactate/pyruvate ratio agrees with findings of multi-parametric proton MRI data and biopsy results.

These promising results suggest that the translational HP-^{13}C MRI may be clinically significant and highlights the need to integrate HP-^{13}C imaging in multi-parametric MRI of prostate cancer. With new multi-element coil design, accelerated pulse sequences, and a multi-channel clinical polarizer, it is now the time to advance HP-^{13}C MRI as a powerful diagnostic tool.

Chapter 3 Assessment of Prostate Cancer Aggressiveness with Hyperpolarized Dual-Agent 3D Dynamic Imaging of Metabolism and Perfusion

3.1 Abstract

This study applied a 3D dynamic dual-agent hyperpolarized ^{13}C magnetic resonance spectroscopic imaging (MRSI) approach with ^{13}C-pyruvate and ^{13}C-urea to investigate differences in urea AUC and metabolism between low and high grade tumors in the TRAMP transgenic mouse model of prostate cancer. Dynamic MR data were corrected for T_1 relaxation and RF excitation and modeled to provide quantitative measures of pyruvate-to-lactate flux (k_{PL}), urea k_{trans} and urea area under the curve (AUC) and correlated these parameters with TRAMP tumor histologic grade. Significantly higher k_{PL} values were measured for high-grade TRAMP tumors. The increase in k_{PL} flux correlated significantly with higher lactate dehydrogenase activity and mRNA expression of *Ldha*, *Mct1* and *Mct4* as well as with more proliferative disease. There was a significant reduction in urea AUC in high-grade tumors that was associated with increased hypoxia and mRNA expression of *Hif1α* and *Vegf* and increased k_{trans}. In 90% of the high-grade TRAMP tumors, a mismatch in urea AUC and k_{PL} was observed, with low urea AUC being associated with increased k_{PL}. This urea AUC-metabolism mismatch was also associated with lymph node and liver metastases. These findings set the stage for using this new dual hyperpolarized agent imaging approach to investigate the ability of urea AUC and k_{PL} to image aggressive prostate cancer in patient studies.

3.2 Introduction

A pressing need facing the clinical management of prostate cancer patients is an accurate method for distinguishing aggressive, potentially lethal prostate cancer from indolent disease. Prostate cancer (PCa) is the second most prevalent cancer in American men, with 1 in 6 being diagnosed, but is fatal in only 12% of these cases (97). Active surveillance has emerged as an appropriate management technique for patients in whom disease is likely to be indolent (tumors ≤ 0.5 cc and Gleason grade ≤ 3+3)(98). New focal therapy approaches are also being considered for men with defined regions of localized intermediate risk PCa (moderate size cancers with secondary Gleason 4 pattern) that can be clearly identified on imaging (99,100), while patients with more aggressive but localized disease are treated with surgical or radiation therapy. Therefore, the ability to localize and provide a non-invasive imaging assessment of cancer aggressiveness has become critically important for clinical management of men with prostate cancer. The current state-of-the-art for imaging localized prostate cancer, multiparametric ^{1}H MRI, has demonstrated the ability to localize tumors for subsequent biopsy and treatment, but cannot consistently grade tumor aggressiveness accurately in individual patients (100).

Increasing evidence points to prostate cancer being a disease strongly linked to abnormal metabolism due to changes in key metabolic enzymes (101). Also, tumor microenvironment factors such as perfusion (102) have been associated with the presence and aggressiveness of prostate cancer. In this study a new dual agent hyperpolarized (HP) ^{13}C MRI approach was investigated to characterize aggressive cancers based on their metabolic and perfusion abnormalities and

applied to a preclinical mouse model of prostate cancer. The development and progression of prostate cancer in the Transgenic Adenocarcinoma of Mouse Prostate (TRAMP) model mimics many aspects of human prostate cancer (103). Specifically, cancer development in the TRAMP model is targeted to the prostate and tumors progress from primary androgen dependent to large androgen independent tumors with metastases. Additionally, most male TRAMP mice develop tumors that are pathologically similar to human prostate cancer and are large enough for MRI studies (104). Metabolically, the TRAMP model has demonstrated changes in TCA metabolism and glycolysis associated with the evolution and progression of prostate cancer in patients (103).

Hyperpolarized ^{13}C MRI is a powerful new metabolic imaging method which uses specialized instrumentation to provide signal enhancements of over 10,000-fold for ^{13}C enriched, safe, endogenous, non-radioactive compounds (105). While prostate cancer is often inadequately evaluated using FDG-PET (which assesses glucose uptake and phosphorylation) (106,107), HP ^{13}C MR detects down-stream metabolism, specifically the metabolic flux of HP ^{13}C-pyruvate to lactate (k_{PL}) catalyzed by lactate dehydrogenase (LDH). This method has shown great potential for not only detecting prostate cancer, but for also assessing the aggressiveness (pathologic grade) of the cancer (5). The "Warburg effect", an elevation in glycolysis and lactate production in the presence of oxygen, occurs in prostate cancer and is due to multiple factors, including oncogenic modulations, mitochondrial dysfunction, as well as an adaptive response to the tumor microenvironment to promote proliferation (108). A prior single time-point ^{13}C MRSI study of

hyperpolarized ^{13}C-pyruvate metabolism in the TRAMP model demonstrated a significant increase in hyperpolarized ^{13}C-lactate in high- versus low- grade prostate tumors (5). The unprecedented gain in sensitivity provided by hyperpolarization can be combined with fast spectroscopic ^{13}C MRSI techniques to provide spatially resolved dynamic data of hyperpolarized pyruvate metabolism (109). This dynamic data can be fit to kinetic models (110) to obtain the flux of HP ^{13}C-pyruvate to lactate catalyzed by lactate dehydrogenase rather than a single-time point measurement of hyperpolarized ^{13}C-lactate which is very sensitive to differences in the timing of probe delivery and when the imaging data is acquired. Another important feature of HP ^{13}C MRSI is that it encodes chemical as well as spatial information, thereby providing the potential for using multiple hyperpolarized ^{13}C-labeled agents to detect several metabolic and/or physiologic processes simultaneously after the injection of a single bolus (111). HP ^{13}C-urea is not taken up and metabolized by most tissues and prior publications have demonstrated that hyperpolarized ^{13}C-urea provides a reproducible and accurate assessment of blood perfusion in animal cancer models (111,112). Methods for co-polarizing ^{13}C-pyruvate and ^{13}C-urea have been developed, successfully polarized, and injected in pre-clinical models to simultaneously measure perfusion and metabolism (111).

The goal of this study was to use a 3D dynamic, dual-agent, ^{13}C-pyruvate and ^{13}C-urea, HP ^{13}C MRSI approach to investigate differences in perfusion and metabolism metrics between high- and low-grade tumors in the TRAMP model.Increasing evidence points to prostate cancer being a disease strongly linked to abnormal metabolism due to changes in key metabolic enzymes (101). Also,

37

tumor microenvironment factors such as perfusion (102) have been associated with the presence and aggressiveness of prostate cancer. In this study a new dual agent hyperpolarized (HP) ^{13}C MRI approach was investigated to characterize aggressive cancers based on their metabolic and perfusion abnormalities and applied to a preclinical mouse model of prostate cancer. The development and progression of prostate cancer in the Transgenic Adenocarcinoma of Mouse Prostate (TRAMP) model mimics many aspects of human prostate cancer (103). Specifically, cancer development in the TRAMP model is targeted to the prostate and tumors progress from primary androgen dependent to large androgen independent tumors with metastases. Additionally, most male TRAMP mice develop tumors that are pathologically similar to human prostate cancer and are large enough for MRI studies (104). Metabolically, the TRAMP model has demonstrated changes in TCA metabolism and glycolysis associated with the evolution and progression of prostate cancer in patients (103).

Hyperpolarized ^{13}C MRI is a powerful new metabolic imaging method which uses specialized instrumentation to provide signal enhancements of over 10,000-fold for ^{13}C enriched, safe, endogenous, non-radioactive compounds (105). While prostate cancer is often inadequately evaluated using FDG-PET (which assesses glucose uptake and phosphorylation) (106,107), HP ^{13}C MR detects down-stream metabolism, specifically the metabolic flux of HP ^{13}C-pyruvate to lactate catalyzed by lactate dehydrogenase (LDH). This method has shown great potential for not only detecting prostate cancer, but for also assessing the aggressiveness (pathologic grade) of the cancer (5). The "Warburg effect", an elevation in glycolysis and lactate

production in the presence of oxygen, occurs in prostate cancer and is due to multiple factors, including oncogenic modulations, mitochondrial dysfunction, as well as an adaptive response to the tumor microenvironment to promote proliferation (108). A prior single time-point ^{13}C MRSI study of hyperpolarized ^{13}C-pyruvate metabolism in the TRAMP model demonstrated a significant increase in hyperpolarized ^{13}C-lactate in high- versus low- grade prostate tumors (5). The unprecedented gain in sensitivity provided by hyperpolarization can be combined with fast spectroscopic ^{13}C MRSI techniques to provide spatially resolved dynamic data of hyperpolarized pyruvate metabolism (109). This dynamic data can be fit to kinetic models (110) to obtain the flux of HP ^{13}C-pyruvate to lactate catalyzed by lactate dehydrogenase rather than a single-time point measurement of hyperpolarized ^{13}C-lactate which is very sensitive to differences in the timing of probe delivery and when the imaging data is acquired. Another important feature of HP ^{13}C MRSI is that it encodes chemical as well as spatial information, thereby providing the potential for using multiple hyperpolarized ^{13}C-labeled agents to detect several metabolic and/or physiologic processes simultaneously after the injection of a single bolus (111). HP ^{13}C-urea is not taken up and metabolized by most tissues and prior publications have demonstrated that hyperpolarized ^{13}C-urea provides a reproducible and accurate assessment of blood perfusion in animal cancer models (111,112). Methods for co-polarizing ^{13}C-pyruvate and ^{13}C-urea have been developed, successfully polarized, and injected in pre-clinical models to simultaneously measure perfusion and metabolism (111).

The goal of this study was to use a 3D dynamic dual-agent, ^{13}C-pyruvate and ^{13}C-urea, HP ^{13}C MRSI approach to investigate differences in perfusion and metabolism metrics between high- and low-grade tumors in the TRAMP model.

3.3 Materials and Methods

3.3.1 Animal protocol and handling

All animal studies were conducted in accordance with the policies of Institutional Animal Care and Use Committee (IACUC) at University of California, San Francisco (UCSF). TRAMP model, supplied by Roswell Park Cancer Institute (Buffalo, NY, USA), was generated in a C57BL/6 background utilizing a transgene consisting of a 7426/28 bp fragment of the rat probasin (rPB) gene directing the tissue-specific expression of simian virus 40 (SV40) early genes (T/t antigens; Tag) to the mouse prostate epithelium to abrogate the activity of the p53 and Rb tumor suppressors(104). The 19 TRAMP mice utilized in this study were cannulated using a 32-gauge IV catheter in the lateral tail vein and anesthetized with 1~1.5% isoflurane/100% oxygen at a rate of 1L/min on a heated water bed to maintain physiological body temperature.

3.3.2 MR Imaging

The imaging studies were performed on a 3T MR scanner (MR750, GE Healthcare, Waukesha WI) using a custom built dual-tuned ^{13}C-proton quadrature murine coil. Dynamic HP ^{13}C spectral data were acquired after a tail vein injection of 350µl of co-polarized 80mM [1-^{13}C]pyruvate and ^{13}C urea (details in Supplementary Material and Methods) using a 3D HP ^{13}C compressed sensing EPSI sequence (109)

with a FOV of 4cm x 4cm x 8.6cm, a spectral BW of 581Hz, with a spatial resolution

of 3.3mm x 3.3mm x 5.4mm, and a temporal resolution of 2 seconds. Eighteen time

points were acquired starting immediately after the 15 s injection. Anatomical

reference images were acquired using a T_2-weighted Fast Spin Echo (FSE) sequence

(spatial resolution: 0.23mm, FOV-6 cm, TE/TR = 102/5821 ms).

3.3.3 Histopathologic analysis

TRAMP mice were euthanized and dissected within 6 hours of the MRI study.

To measure tumor hypoxia, Pimonidazole (PIM) solution was injected

approximately 45 minutes prior to euthanization. Dissection was performed by an

experienced uro-oncologist and digital images were taken as a reference for

localization and registration of tumor specimens. The excised tissue was aliquoted

for histochemical processing, gene expression and activity analyses (details in

Supplementary Material and Methods). The histological index, as defined in Albers

et al. was used to pathologically define high- versus low-grade TRAMP tumors in

this study (5). A histologic index was calculated based on the weighted percentages

of tumor differentiation (normal, well-differentiated, moderately well differentiated

and poorly differentiated) from standard H&E staining. The histologic index ranged

between 0 and 3, where 0 indicated that 100% of the tissue was normal and 3

indicated that 100% of the tissue was poorly differentiated. In the Albers'

publication as in this one, the tumors were dichotomized to be either low grade

(index ≤ 1) or high grade (index ≥ 2) in a manner that reflects the clinical pathologic

situation in which patients with Gleason score ≤ 3+3 are considered to have low

versus Gleason ≥ 3+4 high grade tumors. In all cases, the histological assessments

were determined from what were considered globally representative sections of the tumor masses.

Metastases were detected and enumerated at the time of primary tumor dissection, by careful, systematic, visual inspection and concomitant photography of the abdominal and thoracic cavity contents, starting in the pelvic area with identification/inspection of pelvic and para-aortic lymph nodes, then moving to the mid-abdomen with inspection of the kidneys, peri-renal lymph nodes and mesentery, then moving to the upper abdomen, removing the liver and inspecting the surfaces of all its lobes, and lastly inspecting the thoracic cavity, particularly the lungs for any parenchymal metastases and the mediastinum area for any adenopathy. All visually identified metastatic lesions were confirmed by subsequent histological examination.

3.3.4 Data Processing

The HP MRSI data were reconstructed using a compressed sensing (CS) approach (details in Supplementary Materials and Methods)(113). As shown in Figure 3.1, this processing resulted in 3D arrays (Figure 3.1A) of dynamic HP ^{13}C spectra (Figure 3.1B) demonstrating resonances due to ^{13}C-urea, [1-^{13}C]alanine, [1-^{13}C]pyruvate and [1-^{13}C]lactate. Co-registration of the histological sections and HP ^{13}C MRI data was achieved by cutting multiple sections of tumors in the same axial plane as the MRI images and taking care to mark various surfaces of primary tumors in situ with surgical dyes. Where possible, anatomical landmarks, such as urethra and bladder were also utilized to help register histological cross sections with the MRI sections. Although data were zero filled for display purposes, quantitation of

42

the HP ^{13}C MR data was performed using the native acquisition resolution of the data. The ROI's incorporating the tumor were defined using the anatomical T$_2$w images as reference, and only voxels that were > 85% in the tumor were quantified. Necrotic regions could be also visualized on the T$_2$w images and these voxels were found to have low S/N, so the spectral S/N filter (SNR<4) employed removed necrotic voxels from the analysis. All pre-processing of ^{13}C data, including reorganizing the k-space and ℓ_1-minimization and signal filtering were performed using MATLAB (Mathworks, Nattick MA), and the data was displayed using the open-source SIVIC package (114).

3.3.5 Modeling of k$_{PL}$ and k$_{trans}$

HP [1-^{13}C]pyruvate to [1-^{13}C]lactate flux (K$_{PL}$) was modeled using a 2-compartment model as shown in Figure 3.2(C), described in the following equation

$$\frac{dM_{lac}(t)}{dt} = k_{PL}M_{pyr}(t) - \left(1/T_{1,lac}\right)M_{lac} \tag{i}$$

$$\frac{dM_{pyr}(t)}{dt} = -(k_{PL} + k_{PA})M_{pyr}(t) - \left(1/T_{1,pyr}\right)M_{pyr}(t) \tag{ii}$$

$$M_x{}^+[n] = M_x{}^-[n] \cdot \cos\theta_n \tag{iii}$$

$$S_x[n] = M_x{}^-[n] \cdot \sin\theta_n \tag{iv}$$

where $M_x(t)$ is the longitudinal magnetization of metabolite x, k$_{PL}$ is the pyruvate-to-lactate conversion rate constant, k$_{PA}$ is the pyruvate-to-alanine conversion rate constant (Alanine was included in modeling), and T$_{1,x}$ is the spin-lattice relaxation time. M$_x$$^+$[n] and M$_x$$^-$[n] represent the net HP ^{13}C magnetization before and after the nth RF excitation (with flip angle θ_n), and $S_x[n]$ is the observed metabolite signal.

Quantitatively, perfusion and permeability can be reflected by the dynamic

bio-distribution of HP ^{13}C-urea between blood and tissue *in vivo* similar to the above

equation (Figure 3.2F)

$$\frac{dC_{tissue}(t)}{dt} = k_{trans}C_{blood}(t) - k_2 C_{tissue}(t) \qquad \qquad \text{(v)}$$

where $C_{blood}(t)$ represents the arterial input function (AIF), $C_{tissue}(t)$ is the time-

resolved concentration in tissue, and k_{trans} (115) and k_2 are modified forward and

reverse perfusion coefficients, respectively. In the non-linear numerical fitting, the

reverse perfusion coefficient k_{ep} and the relaxation T_1 are highly linearly-dependent

variables. Therefore, we combined k_{ep} and T_1 into a generalized term k_2. The

coefficient k_2 reflects the combined effect of physiology and longitudinal relaxation.

The summed HP ^{13}C-urea peak area under dynamic curve (AUC), was also calculated

and normalized to kidney urea AUC. Normalized urea area-under-curve (AUC)

provides a measure of tracer distribution in tissue, while k_{trans} provides combined

measure of perfusion and permeability (115). For the AUC metric, although a

rigorous definition of timing requires an offset t_0 in the parameter models, the

definition used should be reasonable given the relatively consistent urea peak

position (±3 seconds) observed (Figure 3.7).

Numerical fitting of the in-vivo dynamic data to the two-compartment model

was performed using non-linear least squares algorithm for both dynamic HP [1-

^{13}C]pyruvate (Figure 3.2B) and HP ^{13}C-urea signals (Figure 3.2E). The multiband

variable flip excitation scheme (θ), and spin lattice (T_1) relaxation times were taken

into account as sources of signal loss using a hybrid continuous-discrete time

dynamical system (110). The reverse flux of HP [1-^{13}C]lactate to HP [1-^{13}C]pyruvate

was excluded from the models since it has been determined to be negligible in TRAMP tumors (116), and a lower number of free variables improves fitting stabilization. The MATLAB-based fitting iterates until a local minimum in object function is arrived from the initial values.

3.3.6 Statistical Analyses

Average values of k_{PL}, urea AUC, and urea k_{trans} were calculated from the entire TRAMP tumor, excluding regions of necrosis, using the T_2 weighted anatomic reference image to identify the tumor. Ki-67 and PIM immunohistochemical staining were reported as the mean fraction of cells (average ± stdev) staining positive. mRNA expression data are reported as relative changes to housekeeping genes. Significance was reported using the standard Mann-Whitney-Wilcoxon test comparing all measured parameters in low- versus high-grade TRAMP tumors (MATLAB) and at 3 significance levels, i.e., p-values of <0.05, $p < 0.01$, $p < 0.001$.

3.4 Results
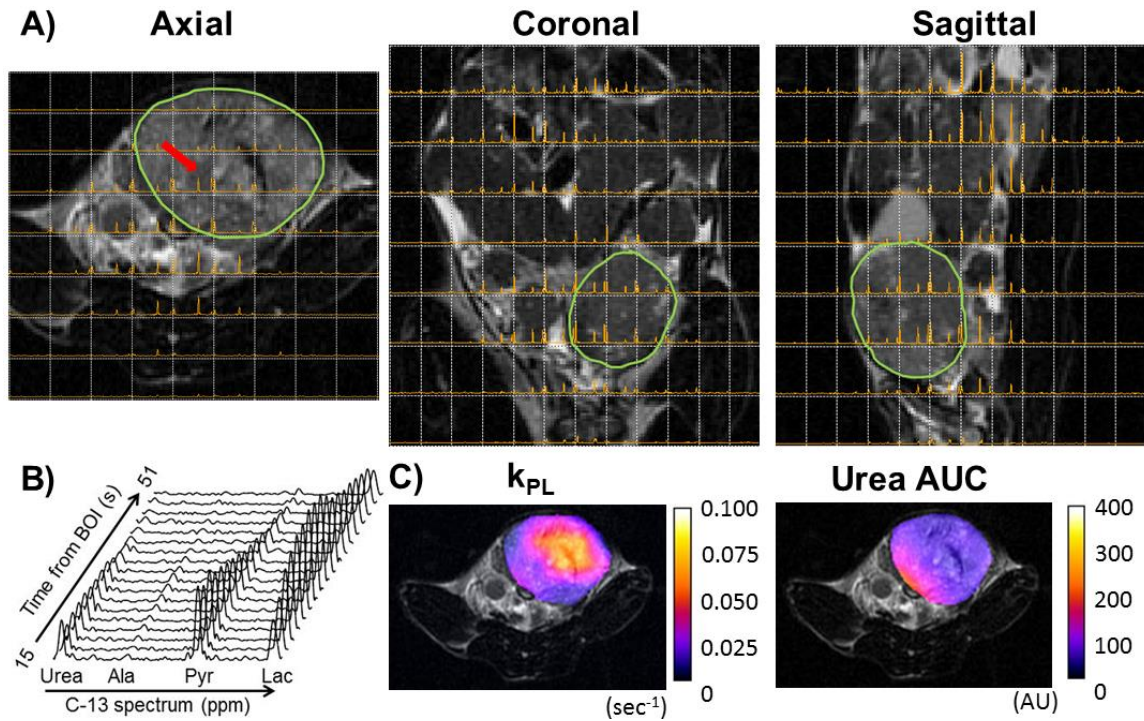
Figure 3.1 A) *In vivo 3D ^{13}C MR spectral arrays shown at a single time point taken 20 seconds after injection of co-polarized HP ^{13}C-pyruvate in the axial, coronal, and sagittal planes overlaid on T_2-weighted anatomical references. The spectra have an anterior-posterior and right-left resolution of 3.3 mm and a superior-inferior resolution of 5.4 mm. The primary tumor is outlined in green.* **B)** *Dynamic data (2s temporal resolution) shown for a representative 0.059 cm^3 voxel in the center of the TRAMP tumor (red arrow) demonstrating resonances of ^{13}C-urea, [1-^{13}C]pyruvate, and the metabolic products [1-^{13}C]lactate, [1-^{13}C]alanine.* **C)** *Corresponding axial pyruvate-to-lactate conversion rate k_{PL} and urea area under curve (AUC) images overlaid on T_2-FSE anatomical references, respectively.*

Hyperpolarized ^{13}C dynamic MRSI data were acquired on a total of 19

TRAMP mice, 10 with high- and 9 with low-grade tumors. The FOV of the dynamic

CS-EPSI sequence (FOV - 4x4x8.6 cm) enabled 3-dimensional detection of

hyperpolarized ^{13}C spectra throughout the primary tumor and from the majority of

mouse abdomen. Figure 3.1A shows representative HP ^{13}C MR spectra in the axial,

coronal and sagittal planes acquired 21 seconds after the injection of HP [1-

[13C]pyruvate. Figure 3.1B, Figure 3.2A and Figure 3.2D show representative

dynamic HP ^{13}C spectra (2 sec. temporal resolution) taken from a single voxel from

the center of the TRAMP tumor shown in Figure 3.1A (red arrow). The dynamic HP

^{13}C spectral acquisition started at ~15s from the start of injection of the

hyperpolarized solution, at which time the HP [1-^{13}C]pyruvate signal was near

maximum (t≈ 15-20 sec). Also at this time point, the metabolic products, HP [1-

^{13}C]lactate and [1-^{13}C]alanine, were already observed in the TRAMP tumor and

reached maximum signal intensity at ≈ 25-30 seconds and 30-35 seconds,

respectively.   Similar to HP [1-^{13}C]pyruvate, HP-^{13}C urea had a maximal signal

intensity at ~15-20 seconds. The timing of the dynamic data acquired for HP [1-

^{13}C]pyruvate, [1-^{13}C]lactate, [1-^{13}C]alanine and ^{13}C-urea was not different between

low- and high-grade tumors.
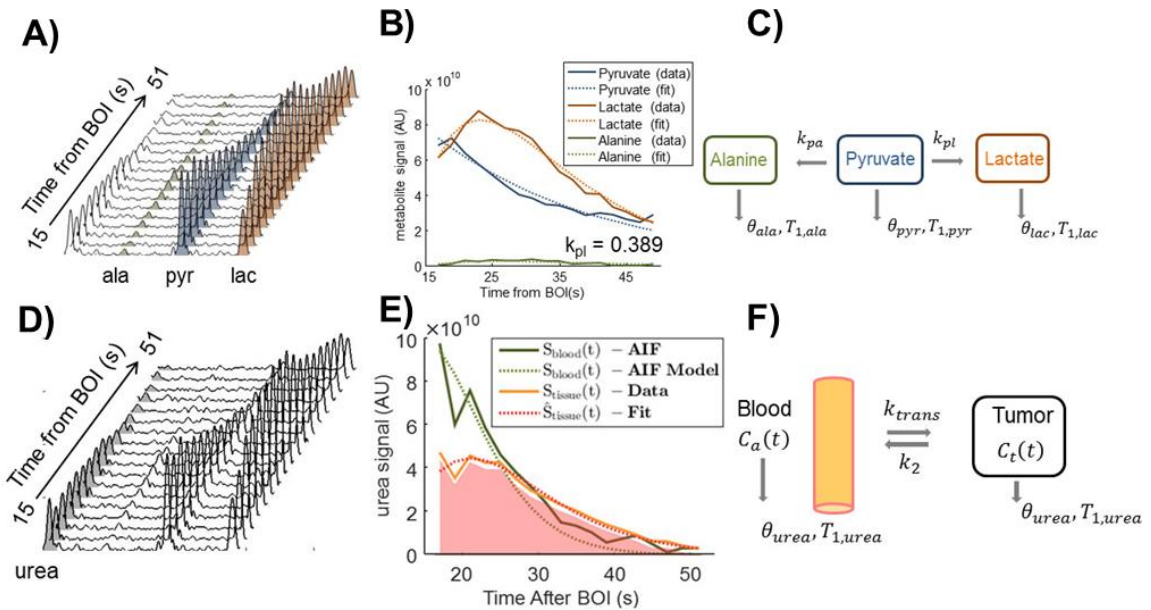
Figure 3.2 A) *Dynamic hyperpolarized spectral data acquired after injection of HP [1-*
^{13}C]pyruvate. ***B)*** *Plot showing the raw signal intensities of pyruvate, lactate, alanine*

*versus time (solid line) and the corresponding modeled metabolic data (dash line) used to determine k_{PL} as shown in the flow diagram **C)** and described in the Methods. **D)** HP ^{13}C- urea signals were extracted from the tumor and from nearby vessels to define an arterial input function (AIF) **E)** Fitting dynamic models to urea perfusion curves, with shaded region showing perfusion area under curve (AUC) **F)** two-compartment model for calculating the rate constant k_{trans}.*

Figure 3.2 depicts the analysis of the dynamic spectral data including correction for T_1 relaxation and flip-angle and modeling to provide quantitative measures of pyruvate-to-lactate rate constants (k_{PL}) and k_{trans}. Representative fits of the dynamic HP [1-^{13}C]pyruvate and HP ^{13}C-urea data to obtain k_{PL} and k_{trans} are shown in Figure 3.2B and E. Spatially interpolated maps of k_{PL} and urea AUC were overlaid on the corresponding anatomic reference image (Figure 3.1C). The k_{PL} and urea overlays were restricted to the region of the tumor as identified on the T_2 weighted anatomic reference image. In Figure 1C, the mismatch between urea AUC and metabolism is clearly seen in comparing the k_{PL} and urea AUC images of the high-grade tumor. Areas of this TRAMP tumor that demonstrated the lowest urea AUC ($\approx$ 75-100 units) also showed the highest k_{PL} (0.055 to 0.075 sec^{-1}). This mismatch between metabolism and urea AUC was observed in 9 out of 10 of the high-grade TRAMP tumors studied, and this mismatch was not observed in any of the low-grade tumors. Additionally, 50% of the high-grade tumors demonstrated either lymph node or liver metastases, with mice having low-grade tumors not demonstrating any metastases.
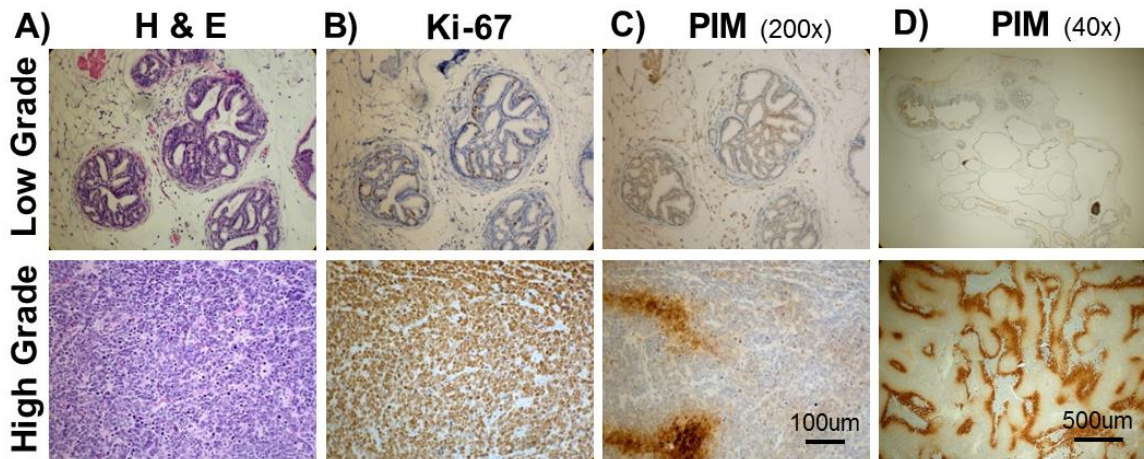
Figure 3.3 *Immunochemical staining of excised representative low- and high-grade TRAMP tumors;* ***A)*** *H&E section,* ***B)*** *Ki-67 staining, and* ***C)*** *PIM staining. The micrographs in A-C were taken under 200x magnification and* ***D)*** *PIM staining under 40x magnification*

Representative immunochemical stained tissue sections from low- and high-grade TRAMP tumors are shown in Figure 3.3. Similar to the human prostate, normal murine prostate histology is highly glandular with secretory epithelial cells lining glands and stromal tissue supporting the glands (not shown). The H&E histologic sections from the low- and high-grade tumors (Figure 3.3A) depict the gradual replacement of the secretory epithelial cells by less differentiated epithelial cells until the glands were completely eliminated and only sheets of pleomorphic cells with irregular nuclei remained in the high-grade tumors. High-grade TRAMP tumors also demonstrated higher Ki-67 (Figure 3.3B) and PIM (Figure 3.3C) staining as compared to low-grade TRAMP tumors.
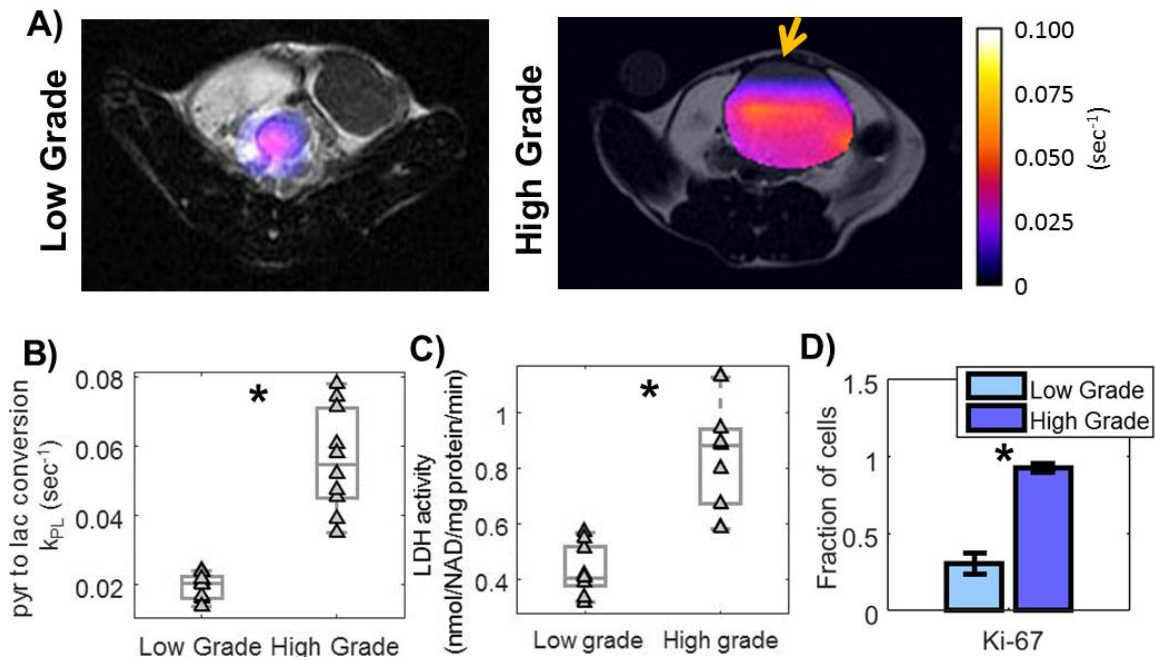
Figure 3.4 A) *Representative calculated pyruvate-to-lactate flux (k_{PL}) images overlaid on corresponding T_2-FSE reference images from a low-grade (left) and a high-grade (right) TRAMP tumor. At pathology, a region of necrosis was observed in the anterior aspect of the tumor (red arrow).* *B)* *Box plots showing individual (diamonds), median and standard deviation k_{PL} flux measurements in the 9 low-grade and 10 high-grade TRAMP tumors.* *C)* *A bar plot showing the fraction of cells staining positive for Ki-67 (mean ± standard error) and* *D)* *LDH activities for the same TRAMP tumors. *significantly different.*

Pyruvate to lactate flux images overlaid on corresponding T_2-FSE anatomical

reference images from a representative low- and a high-grade TRAMP tumor

(Figure 3.4A) demonstrated a heterogeneous but higher k_{PL} flux in the high-grade

tumor. Also in this high-grade tumor, there was a region of necrosis observed at

pathology in the anterior aspect of the tumor associated with undetectable k_{PL} (red

arrow). Pyruvate to lactate flux (k_{PL}) values (Figure 3.4B) were significantly

($p<0.001$) higher (0.056 ± 0.005 sec^{-1} versus 0.019 ± 0.001 sec^{-1}) for high- versus

low-grade TRAMP tumors with no overlap of individual k_{PL} values between the 2

groups in this study. The increase in k_{PL} flux significantly correlated with higher

LDH activity (0.85 ±0.06 vs low-grade: 0.43 ± 0.03, mM/mg protein/min, p<0.001)

in high- versus low-grade tumors (Figure 3.4D). Also, the high-grade TRAMP

tumors were found to be more proliferative with a significantly (p<0.001) larger

portion of the tumor staining positive for Ki-67 than for low-grade tumors (95 ± 3%

versus. 30 ± 7%). The alanine conversion was 1-2 orders of magnitude smaller than

k_{PL}, and there was no difference between high- and low- grade tumors (k_{PA} low-:

0.002 ± 0.001 sec^{-1}, high-grade: 0.004 ± 0.001 sec^{-1}, P>0.4).
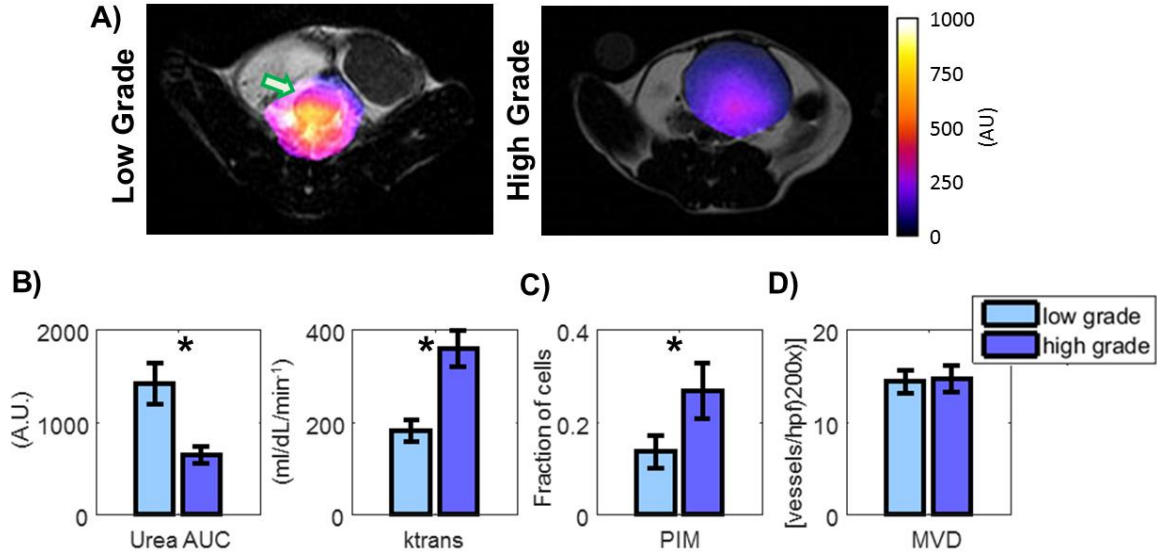
*Figure 3.5 A) Representative calculated urea perfusion images overlaid on the corresponding T_2-FSE anatomical reference images from a low-grade (right) and a high-grade TRAMP tumor. B) Bar plots showing average ± standard error for urea AUC, k_{trans}, and C) fraction of cells staining positive for PIM in the 9 low-grade and 10 high-grade TRAMP tumors studied. D) No difference found in representative microvascular density (MVD) assessed by CD31 IHC staining. (3 high- vs. 3 low-grade) *significantly different.*

Figure 3.5A shows urea AUC images overlaid on reference anatomical images

of the same animals shown in Figure 3.4A, visually demonstrating heterogeneous

but higher urea AUC in the low- versus high-grade tumor. A quantitative comparison of urea AUC and k_{trans} for the low- and high-grade tumors is shown in Figure 3.5B. Urea AUC was significantly reduced ($p<0.01$, 640 ± 94 as compared to the 1407 ± 221 AU), while k_{trans} significantly increased ($p<0.01$, 358 ± 38 as compared to 180 ± 24 ml/dL/min) in high- versus low- grade tumors. The hypoxia was also significantly ($p<0.05$) increased in high- relative to low-grade prostate cancer (27 ± 6% versus 14 ± 4% of the tumor staining positive for PIM, respectively), as measured by PIM immunohistochemical staining (Figure 3.5D). Interestingly, no significant difference was found in micro-vessel density between high- and low-grade TRAMP tumors (high-grade = 14.3 ± 1.7, low-grade = 14.7 ± 2.1 vessels/hpf 200x, P > 0.5).
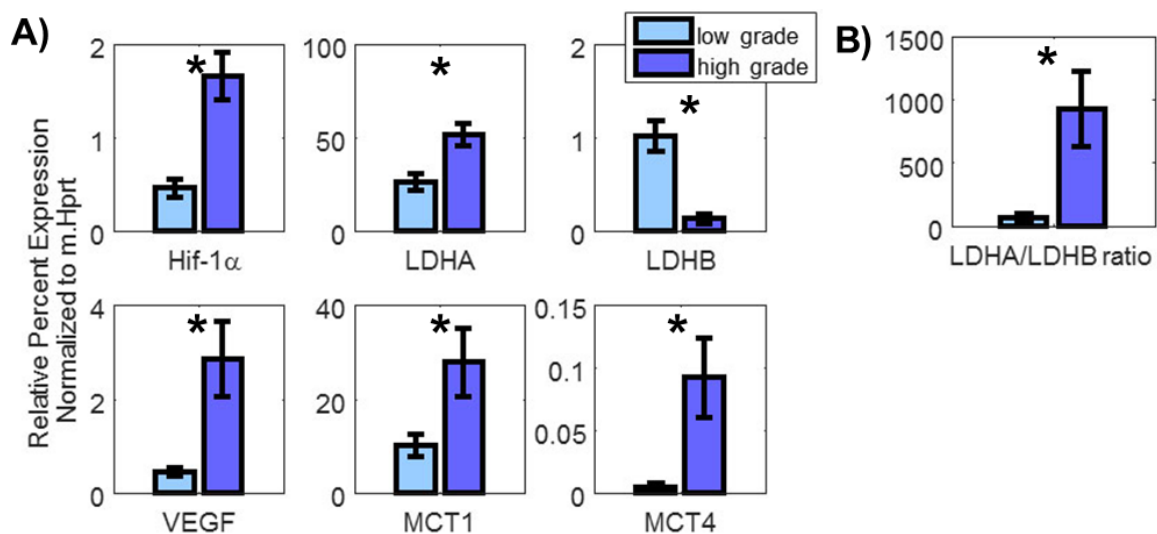
Figure 3.6 A) *mRNA expression level ± standard error of Hif-1a, Ldha, Ldhb, Vegf, Mct1 and Mct4 for the 9 low-grade and 10 high-grade TRAMP tumors studied; values given are relative percent expression normalized to m.Hprt. **B)** Ldha/Ldhb ratio for the same TRAMP tumors. *significantly different.*

Figure 3.6 summarizes the expression of key transporters and enzymes associated with pyruvate transport and metabolism (*Mct1* and *Mct4*, *Ldha* and *Ldhb*) and of factors impacted by the hypoxic tumor microenvironment (*Hif1α* and *Vegf*). Expression of the monocarboxylate transporters *Mct1* and *Mct4* were significantly upregulated (*Mct1*: 2.75 ± 0.72 fold, $p < 0.05$, *Mct4*: 20.7 ± 7.12 fold, $p<0.01$) in high-versus low-grade TRAMP tumors. *Ldha* was significantly increased 1.98 ± 0.22 fold ($p<0.01$) and *Ldhb* significantly decreased to 0.13±0.05 fold ($p<0.01$) leading to a dramatic 15.0 ± 4.8 fold increase ($p<0.001$) in the *Ldha/ Ldhb* ratio in high- versus low-grade TRAMP tumors. Due to increased hypoxia in the tumor microenvironment (higher PIM staining), there was a significant 3.64 ± 0.55 fold ($p<0.01$) and 6.40 ± 1.82 fold ($p<0.01$) increase in *Hif1α* and *Vegf* expression, respectively, in high- versus low-grade TRAMP tumors.
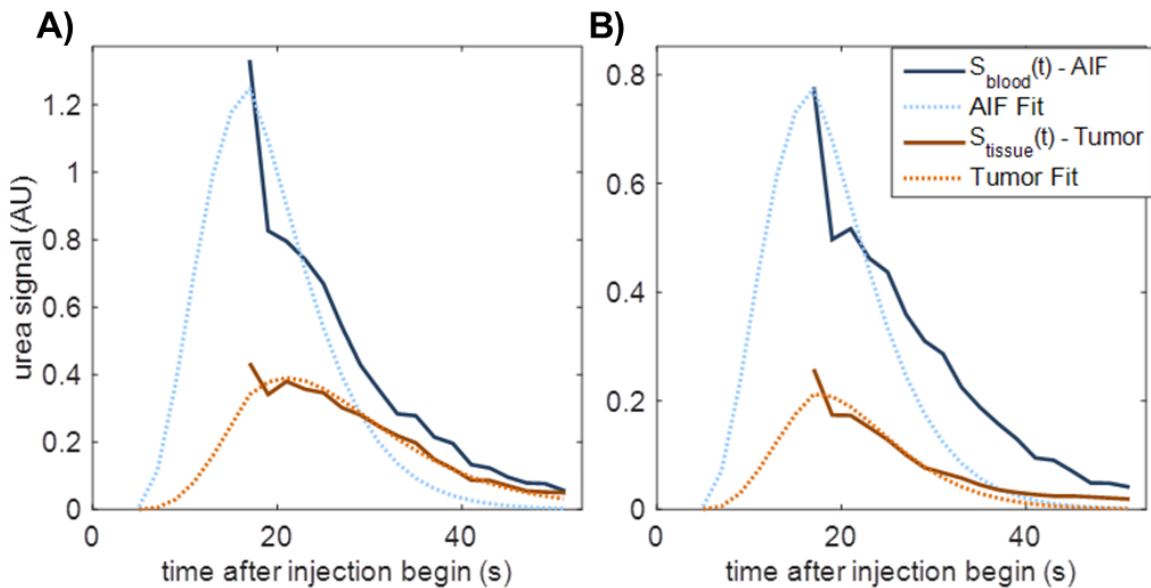
Figure 3.7 Mean urea perfusion data (solid lines, blue - AIF, gold - tumor) for *A)* low-grade and *B)* high-grade TRAMP prostate tumors were fitted and k_{trans} and k_2 parameters calculated (high grade k_{trans} = 344, k_2=4380, low-grade k_{trans} =163, k_2=819). The fit curves were extrapolated to the bolus arrival time at t=5(s). In high-

grade tumors, higher cellularity contributes to more rapid clearance of urea and low AUC.

3.5 Discussion and Conclusions

An accurate assessment of the aggressiveness of prostate cancer requires the complete coverage of the prostate at high spatial resolution due to the often small, multifocal, and biologically diverse nature of this disease. In this study, a volumetric dynamic dual-agent hyperpolarized ^{13}C spectroscopic imaging approach using ^{13}C-pyruvate and ^{13}C-urea to simultaneously image changes in urea AUC and pyruvate metabolism with prostate cancer progression was performed for the first time in a transgenic murine model of prostate cancer. The 20,000 - 40,000 fold enhancement in signal-to-noise relative to the respective thermal MR signals at 3T provided by the co-polarization of ^{13}C-pyruvate and ^{13}C-urea combined with fast volumetric ^{13}C spectroscopic imaging allowed for both high spatial (0.06 cm^3) and temporal (2 sec) resolution imaging data to be acquired throughout the primary prostate tumor and the body of the mouse. This dynamic metabolic and perfusion data were fit to kinetic models (110) to obtain the flux of HP ^{13}C-pyruvate to lactate (k_{PL}) catalyzed by lactate dehydrogenase and k_{trans}, a measure of both perfusion and vascular permeability. In addition, an estimate of tumor urea tissue distribution was calculated using the area under curve of hyperpolarized ^{13}C-urea signal (111,112). Moreover, the ability to dynamically measure urea delivery, tissue distribution and pyruvate metabolism allows for differences in the timing of hyperpolarized probe delivery and metabolism that can occur between individual subjects. While these

differences in dynamics were small (2-5 secs), they can add substantially to the variability of single time point hyperpolarized ^{13}C-lactate to ^{13}C-pyruvate ratio measurements, since the ^{13}C-pyruvate signal is dramatically decreasing due to T_1 relaxation and metabolism during the spectral acquisition (5).

There is growing evidence that the up-regulation of aerobic glycolysis and increased lactate production and efflux is an adaptation of cancer cells that aids in survival, growth, metastasis and often leads to poor response to therapy (117,118). The results of this study indicate that increased hyperpolarized ^{13}C-pyruvate to lactate flux (k_{PL}) is associated with more aggressive prostate cancer. Specifically, the k_{PL} was 3 fold higher in high- relative to low- pathologic grade prostate tumors, with no overlap between k_{PL} values from individual high- and low-grade tumors. High-grade TRAMP tumors were also more proliferative, having 3 fold higher Ki-67 staining than low-grade tumors. In concordance with the HP ^{13}C-pyruvate-to-lactate metabolism data, there was a 2 fold increase in tissue LDH activity, as measured ex vivo, in the same high- relative to low-grade tumors. Since the measurement of HP lactate signal generation is in non-steady state dynamics, increased LDH activity is a major factor contributing to the increase in the observed HP lactate signal in high-grade TRAMP tumors. The increased HP ^{13}C-lactate signal observed in high- versus low-grade prostate cancer was also associated with increased mRNA expression of lactate dehydrogenase-A (*Ldha*), decreased expression of *Ldhb*, as well as increased monocarboxylate transporters (*Mct1* and Mct*4*) that have a role in both pyruvate uptake and lactate export (101). LDHA and B are responsible for encoding the M and H subunits of LDH and the high *Ldha/Ldhb* expression ratio observed in high-

grade TRAMP tumors leads to the production of a predominance of the LDH5

isoenzyme (5M subunits) favoring increased lactate production. In patient studies,

a high serum LDH level is associated with aggressive disease and a poor survival for

a variety of cancers (119,120) including prostate cancer (121), and inhibition of the

LDH catalyzed production of lactate has become a therapeutic target (122,123).

Studies using patient biopsies and prostate tissue slices removed at surgery have

demonstrated increased steady state pools of lactate, HP ^{13}C-lactate production,

increased LDH activity, and increased mRNA expression of *LDHA* and *MCT1* and *4* in

prostate cancer tissues similar to what has been observed in the TRAMP model used

in this study (124). Moreover, the k_{PL} fluxes observed in this pre-clinical study were

in line with what was calculated from 2D dynamic HP ^{13}C MRSI studies in a Phase 1

clinical trial of hyperpolarized [1-^{13}C]pyruvate in patients with prostate cancer

(0.045 ± 0.025 s^{-1}) (125). However no correlation of k_{PL} with tumor grade was

performed in these prior pre-clinical and clinical studies.

The 6-fold increase in *Mct4* observed in high-grade TRAMP tumors results in

increased export of lactate out of the cells which is important to sustaining a high

glycolytic flux (126). Tumor excretion of lactic acid, combined with poor tumor

perfusion, results in an acidic extracellular pH in tumors compared with normal

tissue (111,127), and this acidification of the tumor microenvironment has also

been shown to occur in the TRAMP model (128). The resulting acidic environment

promotes cancer aggressiveness and metastasis by facilitating a degradation of the

extracellular matrix by proteinases (129,130), increasing angiogenesis through the

release of VEGF (131), and inhibiting the immune response to tumor antigens (132).

Extracellular acidification also may render tumors chemo-resistant (132). Taken together, these observations suggest that not only increased lactic acid production, but also its efflux are important parameters associated with aggressive prostate cancer (133,134). Moreover, tumor-specific metabolic shifts, such as increased production and efflux of lactate, can potentially be exploited for cancer therapy with minimal impact on normal tissues (127).

Hypoxia is a feature of many human cancers and has been implicated as an important biologically modulator of aggressiveness, clinical behavior, and treatment response in prostate cancer (38,135). This study found a significant reduction in urea AUC in high- relative to low-grade TRAMP tumors, and an associated significant increase in hypoxia as measured by increased PIM staining. The oxygen-sensitive HIF-1α transcription factor has been found to be up-regulated in regions of tumor hypoxia and increases the expression of angiogenesis factors such as VEGF to increase oxygen delivery as well as increasing aerobic glycolysis through increasing expression and activity of key enzymes in the glycolytic pathway, including LDH (133). Consistent with this scenario, a significant increase was also observed in the mRNA expression of *Hif1α*, *Vegf*, and *Ldha*, as well as an increase in LDH activity in high- versus low-grade TRAMP tumors. Hypoxic prostate cancers, which induce HIF-1α and glycolysis most strongly, tend to be of higher Gleason grade, are more invasive and metastatic, and less responsive to therapy than those with normal oxygen levels (135,136).

Fitting the dynamic HP ^{13}C-urea to a Tofts-like 2-compartment model (115) demonstrated that k_{trans} was significantly increased in high- versus low-grade

prostate cancer. The parameter k_{trans} represents the transfer of the contrast agent, hyperpolarized ^{13}C-urea, from the vasculature into the extravascular space and is therefore a function of both perfusion and permeability. Therefore, the observed increase in k_{trans} is presumably due to vascular hyperpermeability in high-grade TRAMP tumors, which is also consistent with increased expression of *Vegf* in high-grade tumors. The urea k_{trans} data is also consistent with prior gadolinium dynamic contrast-enhanced MRI studies of prostate cancer patients, in which high-grade prostate tumors demonstrated the earliest and greatest rate of enhancement and k_{trans} (137,138). Although k_{trans} significantly increases, urea AUC significantly decreases in high-grade TRAMP prostate cancer tumors. The explanation for the decrease in urea AUC is the higher clearance of urea from high- versus low-grade tumors as observed in Figure 3.7. A and B. The increased rate of urea clearance (k_{ep}) was most likely due to a dramatic increase in the cellularity of high grade TRAMP tumors and a decrease in Extravascular Extracellular Space (EES) and associated urea tissue distribution volume V_T ($V_T = k_{trans}/k_{ep}$). The measurement of k_{ep} was not directly possible in this study due to the fact that k_2 in our modeling was a lumped coefficient, that included urea clearance (k_{ep}) but was also heavily impacted by urea T_1 relaxation and other signal loss mechanisms (Figure 3.7)(112).

   Another important finding of this study was that there was significant heterogeneity (> 2-fold) of k_{PL} and urea AUC in individual TRAMP tumors, with 90% of the high-grade TRAMP tumors demonstrating regions that had areas of the lowest urea AUC having the highest k_{PL}. Moreover, 50% of the high-grade TRAMP tumors demonstrated either lymph node or liver metastases, while none of the low-grade

tumors demonstrated a urea AUC -k_{PL} mismatch nor any metastases. Although

perfusion and metabolism are tightly coupled in most normal tissues, mismatches

have been observed in a variety of tumors including lung, breast, liver, colon, and

head and neck cancers, and this mismatch was associated with more aggressive

disease (36,37). A perfusion-metabolism mismatch, specifically, a high glycolytic

rate relative to low perfusion, has been imaged in locally advanced breast cancer by

^{15}O-water and ^{18}F-FDG PET; this was associated with poor response to treatment

and early relapse or disease progression (36). This study demonstrated that the

urea AUC - k_{PL} mismatch was similarly associated with aggressive prostate cancer in

the TRAMP model. However, the relationship between urea AUC - k_{PL} mismatch and

aggressive prostate cancer needs to be validated and the relationship between urea

AUC and more conventional measurement of perfusion or blood flow needs to be

determined in future patient studies.

      The TRAMP murine model used in this pre-clinical study, like all pre-clinical

models has its limitations. Most importantly, disease progression in this murine

model is faster than what is observed in prostate cancer patients, with prostate

cancer progressing from early stage to late stage disease in a matter of weeks

instead of years. While the pathologic progression of disease in this model mimics

the human situation, it progresses from an admixture of normal glandular tissue and

cancer to large areas of densely packed malignant cells in a much shorter period of

time. Early and late stage disease is more homogenous in the TRAMP model than in

the human situation due to a lower incidence of coexisting benign prostate tissue,

early- and late stage cancer. Additionally, while there are significant lymph node

metastases in the TRAMP model and some liver metastases, similar to the human situation, there are virtually no bone metastases, unlike the human situation. The data acquisition scheme and the compartmental modeling approach used in this study represented a trade-off between several factors. The dynamic data acquisition scheme utilized double spin-echo refocusing (139) in order to provide improved SNR for individual images, but at the expense of saturating signals at the edges of the RF coil, requiring the acquisition to start at the end, and causing loss of the earliest points of the dynamic data. With this acquisition approach, we found that a two-site uni-directional pyruvate-to-lactate model provided the most robust and reproducible fits. Our approach also did not use information from the AIF. There is potential to improve the kinetic modeling of metabolism and perfusion with acquisitions capturing the bolus input signal, incorporating the AIF, and by using advanced modeling methods such as those presented in Kazan et al (140), Khegai et al (141), and Bankson et al (142).

In summary, the pathologic grade dependence of hyperpolarized pyruvate-to-lactate flux, urea k^{trans} and AUC were measured in a single imaging acquisition after administration of hyperpolarized ^{13}C-pyruvate and ^{13}C-urea in a transgenic mouse model of prostate cancer. High HP ^{13}C-pyruvate to ^{13}C-lactate flux, low ^{13}C urea AUC and high forward perfusion coefficient (k_{trans}) were found to be biomarkers of high-grade prostate cancer in this pre-clinical study. Additionally, a substantial mismatch in urea AUC and a high pyruvate to lactate flux observed in this study were associated with highly proliferative disease with increased metastases. These hyperpolarized imaging biomarkers of aggressive prostate

cancer, and their relationship to the perfusion - metabolism mismatch observed in prior studies, will clearly need to be better understood and validated in future patient studies. The likelihood of translating this hyperpolarized dual-agent MR approach is high since HP ^{13}C-pyruvate is already FDA IND-approved for ongoing clinical trials, and ^{13}C-urea has an excellent safety profile and is administered clinically at doses even higher than would be used for hyperpolarized MRI.

Chapter 4 Translational 3D Dynamic Hyperpolarized 13C-MR Metabolic Imaging - From Mice to Patients

4.1 Introduction

Hyperpolarized (HP) ^{13}C MR has been shown in over 100 published animal studies to provide unprecedented information on previously-inaccessible aspects of biological processes by detecting endogenous, nontoxic ^{13}C-labeled probes that can monitor enzymatic conversions through key biochemical pathways (5,29,105,143-149). Since HP ^{13}C MR encodes chemical as well as spatial information, this new molecular imaging technique allows the simultaneous detection of multiple biologic compounds and metabolic products with sensitivity enhancements of >10,000 fold (1). This extraordinary new technique, therefore presents the fields of oncology and medical imaging with an opportunity to dramatically improve our ability to investigate human disease and to ultimately translate these techniques into the clinic for more individualized patient care. HP-DNP technology is becoming increasingly widespread for scientific investigations with over 50 polarizers worldwide including a few custom-built DNP polarizers being used in university preclinical research and commercial polarizers available from Oxford Instruments since 2006 for *in vitro* and animal studies. Also, our recently completed human Phase 1 clinical trial has demonstrated the safety and feasibility of HP ^{13}C-pyruvate MRI in prostate cancer patients (96). Initial cost estimates are equal to or less than current nuclear medicine imaging methods such as positron emission tomography (PET) that is used clinically for other cancers, but has shown limited utility for primary prostate cancer. Unlike FDG-PET that detects minimal changes in glucose

uptake and phosphorylation with prostate cancer, HP ^{13}C-pyruvate MRI can detect

dramatically altered conversion to lactate due to genetic mutations in cancer that

result in greatly increased lactate dehydrogenase (LDH) enzymatic activity that

correlated with cancer grade in animal models (5). This is complementary but very

different from ^{1}H MRSI which has emerged as a useful tool for measuring increased

endogenous choline levels in cancer, but is limited by its coarse spatial resolution

and long acquisition times (150).
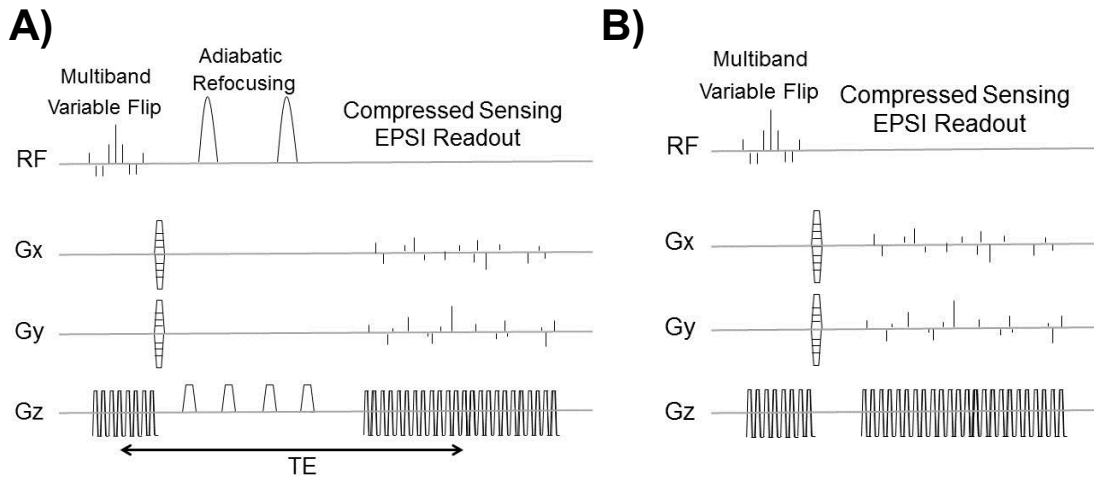
Figure 4.1 *The HP-^{13}C 3D CS-EPSI sequence diagram designed in this project. A) The double spin-echo enabled (DSE mode) was utilized in small animal imaging such as TRAMP prostate tumor studies. B) Another operation mode (FID mode) was applied for larger imaging volumes, such as in rat and clinical studies. The DSE refocusing was removed in order to account for peak B1 limits and increased field inhomogeneity.*

Prostate cancer is a major health concern in the United States with >240,000

new cases per year and >28,000 deaths (7). Due to increased screening using serum

prostate specific antigen (PSA) and extended-template transrectal ultrasound

(TRUS) guided biopsies, patients with prostate cancer are being identified at an

earlier and potentially more treatable stage. Unfortunately, the aggressiveness of

individual tumors cannot be predicted with great confidence in individual patients using currently available clinical and imaging prognostic data (151-155). Preliminary data strongly indicate that hyperpolarized ^{13}C-pyruvate MRI using dynamic nuclear polarization (DNP) has the potential to dramatically improve prostate cancer clinical management. In transgenic prostate cancer mouse models, this method demonstrated the unprecedented ability to separate early stage (low-grade) tumors from late-stage high-grade cancer based on this metabolic parameter (conversion through the LDH pathway) (5). Higher grade prostate cancers, both in transgenic models and human biopsies, have demonstrated several fold increases in LDH expression (5,124). No other imaging method has demonstrated this ability to differentiate low grade, clinically insignificant prostate cancers which are the majority of cases from high-grade disease which kills >28,000 Americans per year.
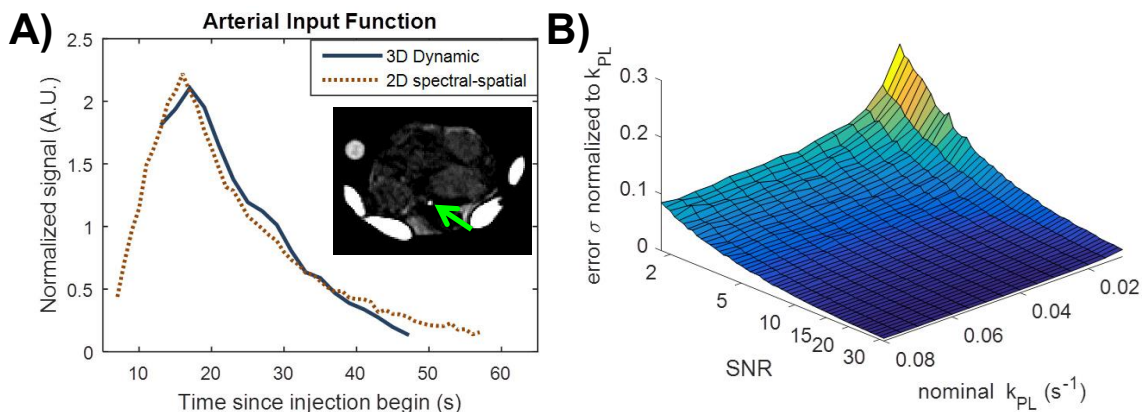
Figure 4.2 *Kinetic modeling for quantitative estimation of key metabolic pathways in TRAMP. **A)** The arterial input function (AIF) using HP-^{13}C urea exhibited high consistency between the acquisition using a constant-flip 2D spectral-spatial excitation and the 3D dynamic CS-EPSI in this study. The 3D dynamic signal was corrected for variable flip angles. A good reference for AIF shape and time course helps defining a model-based AIF profile. **B)** Simulation of error in k_{PL} estimation introduced by data noise. Under a conservative SNR=6, the standard deviation for k_{PL} error was less than ±0.5% for nominal k_{PL} =0.0300.*

The ability to reliably image treatment response is also a critically important unmet clinical need. In our preclinical studies, HP ^{13}C MR detected early response in murine bone metastasis models by 2 days post chemotherapy (156). These preclinical findings are supported by biochemical and gene assays in these models and in human prostate cancer biopsies demonstrating higher expression and activity of the enzyme LDH which catalyzes the conversion of HP ^{13}C-pyruvate to ^{13}C-lactate). The Phase 1 clinical trial of HP ^{13}C-pyruvate in prostate cancer patients demonstrated feasibility and safety through this first human study of hyperpolarized MR metabolic imaging (96) using single-slice 1D dynamic, 2D dynamic and 3D single time point acquisitions. This clinical trial was limited but indicated the potential to characterize the extent and aggressiveness of prostate cancer in individual subjects to ultimately benefit clinical treatment decisions and to monitor treatment response.

The goal of this project was to develop a new dynamic and volumetric acquisition to detect HP pyruvate uptake and enzymatic conversion throughout the prostate with high spatial and temporal resolution. A new 3D dynamic compressed sensing EPSI (3D dynamic CS-EPSI) sequence was developed and comprised of spectral-spatial RF excitation with multiband and variable-flip schemes, followed by a compressed-sensing EPSI readout using random blip encoding. The 3D dynamic imaging protocol was developed and tested in phantoms, transgenic mice of prostate cancer (TRAMPs) and rats before translating this approach for human studies. The translational challenges, including larger imaging volume, reduced peak

RF power and lower B1 inhomogeneity were addressed through the optimization of pulse design and sequence parameters.

4.2 Materials and Methods

4.2.1 Pulse sequences

A 3D dynamic compressed-sensing EPSI (3D CS-EPSI) sequence was designed and optimized to provide more efficient, higher SNR dual-agent metabolic and perfusion hyperpolarized ^{13}C MR scans. The backbone of this sequence consists of spectral-spatial RF excitation pulses, followed by optional double spin echo (DSE) refocusing, and finally the compressed sensing EPSI readout. The RF excitation pulse provided multiband excitation to account for the metabolic conversions between ^{13}C pyruvate and lactate. Moreover, a "variable flip angle" scheme was applied, where the excitation flip angle on each metabolite was progressively increased to account for the loss from previous excitations and the intrinsic T_1 relaxation. The flip angles were calculated based on the T_1-effective scheme, ensuring optimal pyruvate signal-to-noise ratio while maximizing total lactate SNR for robust modeling of metabolic conversion and parameter estimation (13). The spectral-spatial pulses were designed using the SS-RF toolbox developed by Larson et al (55). In TRAMP studies, the DSE refocusing was enabled for high SNR and sharp spectral linewidth (TR = 250ms, TE = 150ms). Nevertheless, the DSE refocusing was disabled in the clinical configuration to limit peak power and account for the increased B_1 inhomogeneity (TR = 150ms, TE = 6.3ms), as shown in Figure 4.1 A) and B).

The three-dimensional readout scheme utilized pseudorandom "blip" encoding in the k_x-k_y directions and flyback echo-planar spectral-imaging (EPSI) in the k_z-k_t dimensions. A pseudorandom undersampling pattern was created in spatial and temporal dimensions, allowing compressed sensing detection to accelerate the acquisition by 18 fold. Another 16 fold acceleration was achieved by the EPSI readout (11,12). A combined 288x acceleration factor condenses a 10-minute fully-sampled acquisition into a 2-second undersampled time interval. Such 2-second temporal resolution enables robust analysis and modeling of metabolic exchange and perfusion dynamics.

A) Pyruvate
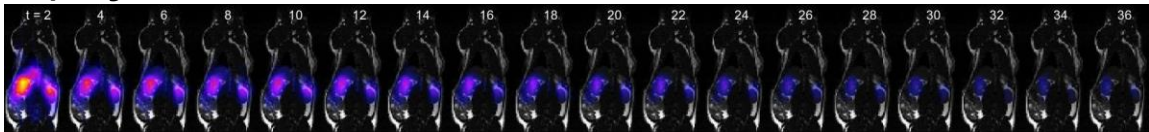
B) Lactate
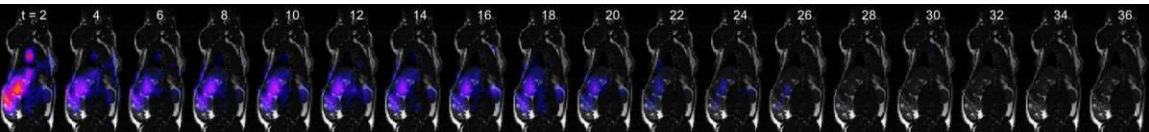
C) Urea
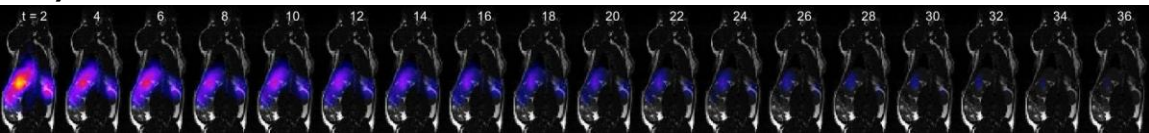
Figure 4.3 *Hyperpolarized ^{13}C dynamics from a healthy Sprague-Dawley rat using the 3D dynamic CS-EPSI sequence in the "FID" mode.* ***A)*** *Pyruvate,* ***B)*** *Lactate and* ***C)*** *Urea as overlaid on a bSSFP reference scan. All the ^{13}C tracer dynamics can be simultaneously acquired within a single injection followed by acquisition with 2s temporal resolution and spatial resolution of 6.7mm x 6.7mm x 10.4mm. The dynamic image series shows high perfusion in the kidney region, rapid pyruvate uptake and conversion to lactate.*

4.2.2 3D Imaging Coverage

The 3D CS-EPSI sequence was designed to offer full 3D coverage for the regions of interest with high spatiotemporal resolution in both preclinical and clinical settings. In TRAMP mice studies, the sequence was configured to cover the entire animal, the advantage of which is twofold. First, the arterial input function (AIF) is included in the FOV and factored into our dynamic models, since AIF is of exceptional importance to estimation of perfusion kinetics. Secondly, it allows not
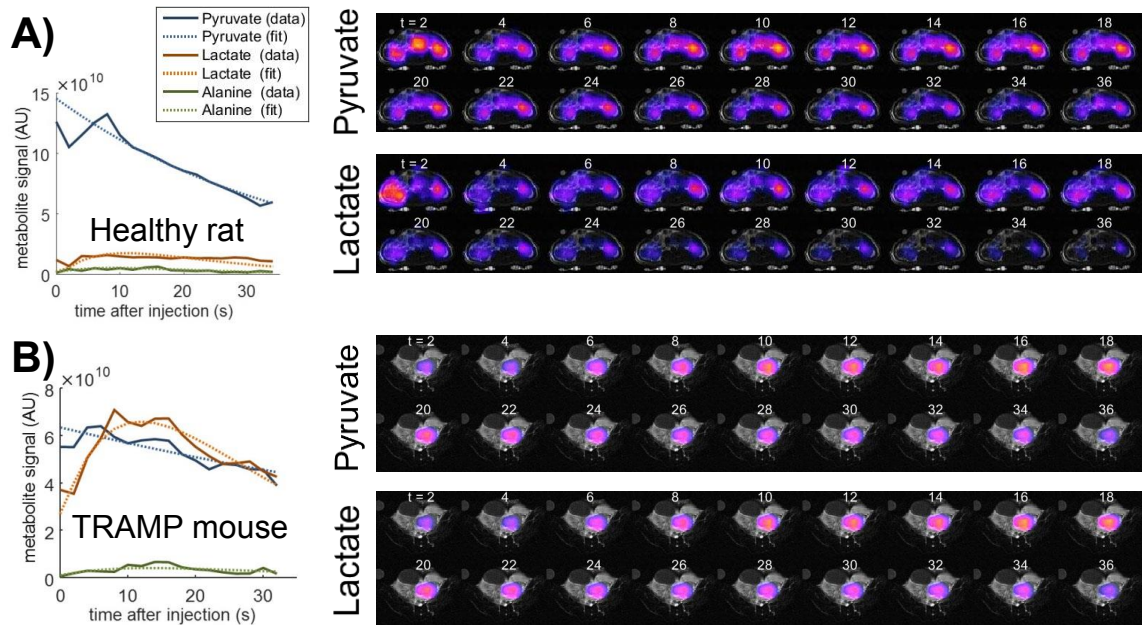
Figure 4.4 *Similar to the "DSE" mode, the in-vivo dynamics of ^{13}C biomarker acquired using the 3D dynamic CS-EPSI "FID" mode can be quantitatively analyzed by compartmental exchange models. **A)** Pyruvate to lactate conversion in the kidneys of healthy rat is visualized in this 13C image overlaid on bSSFP reference. k_{PL} was estimated 0.0058(s^{-1}) **B)** Pyruvate and lactate dynamics overlaid on T2-FSE scan in a low-grade TRAMP tumor. k_{PL} was estimated 0.0297(s^{-1}). Data from mouse and rat agreed well with previous findings.*

only imaging the primary tumor, but sites where there's high likelihood of metastasis, such as PA and PR lymph nodes. In addition, it monitors key

physiological regions such as kidney and liver for possible abnormalities associated

with prostate cancer. In rat studies, the FOV was chosen to extend through the rat
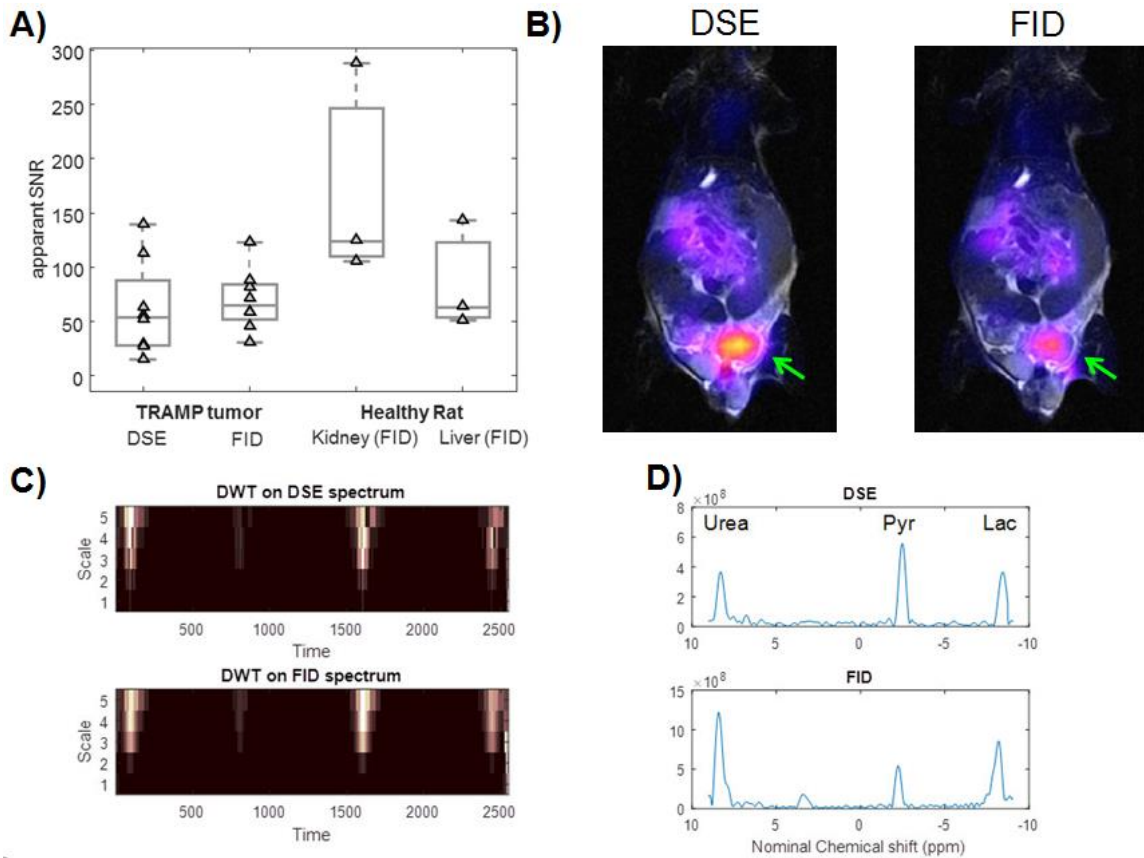
Figure 4.5 *Comparison of the 3D dynamic CS-EPSI "DSE" versus "FID" acquisition mode.* ***A)*** *The mean SNR in vivo acquired using DSE and FID mode was comparable (P>0.3) in TRAMP tumors (N = 8 for each). Good SNR performance was also observed in rat kidney and liver (N = 3).* ***B)*** *This map shows lactate temporal AUC overlaid on T2-FSE reference in a low-grade mouse prostate tumor (arrow). Similar HP-^{13}C distribution pattern and pyruvate-to-lactate conversion dynamics was observed, when acquired with both imaging modes.* ***C)*** *Spectrum in the wavelet-in-time domain indicated that the sparsity criteria in compressed sensing was preserved.* ***D)*** *In-vivo spectra acquired using DSE vs FID sequence has similar widths for pyruvate (Δwidth = 2.1%).*

trunk for similar reasoning. In clinical exams, the sequence covers the full prostate

gland from base to apex, including the PZ, CZ and TZ. The 581Hz-spectral bandwidth

ensures inclusion of the four main biomarkers in this study, namely HP-^{13}C pyruvate, lactate, alanine and urea. Aliasing were introduced to lactate and urea peaks to conserve spectral bandwidth for improved imaging quality, causing these peaks to appear on the opposite edges of the spectrum.

4.2.3 Dynamic Modeling

Hyperpolarized ^{13}C imaging using a dynamic sequence allows quantitative estimation of key metabolic pathways in preclinical TRAMP model of prostate tumor. The pyruvate-to-lactate conversion can be characterized as

$$\frac{dC_{lac}(t)}{dt} = k_{PL}C_{pyr}(t) - k_{LP}C_{lac}(t)$$

where $C_{species}(t)$ is the metabolite concentration, and k_{PL} and k_{LP} are the forward and reverse conversion rate constants, respectively. Similar equation holds for interconversion between HP- ^{13}C pyruvate and alanine.

The signal curves were fitted to the dynamic models using the non-linear least squares analysis, returning estimates of k_{PL} and k_{PA}. RF excitations and relaxation T_1 were included in the model to account for signal loss, where T_1 was assumed to be equal for all ^{13}C metabolites. The reverse conversion rate was assumed to be zero in the model since it is much lower compared to the forward reaction in physiological conditions, and such assumption ensures stability of fitting computation.

Tumor microcirculation can be characterized by perfusion and permeability between blood and tissue. Hyperpolarized ^{13}C urea MR provides a quantitative measurement that not only reflects tumor angiogenesis patterns, but also illustrates

underlying hypoxia and necrosis conditions. Quantitative measures were calculated using the equation describing two-compartment model

$$\frac{dC_{tissue}(t)}{dt} = k_{trans}C_{blood}(t) - k_2 C_{tissue}(t)$$

where $C_{blood}(t)$ represents the arterial input function (AIF), $C_{tissue}(t)$ is the time-resolved concentration in tissue, and k_{trans}, k_2 are modified forward and reverse perfusion coefficients, respectively. A joint fitting scheme was designed to utilize both AIF and tissue dynamics as input, an advantage gained from the whole-animal coverage of the 3D dynamic datasets. The AIF was corrected for intra-voxel partial volume effects. Similar to the metabolic case, perfusion kinetics were fitted to the models using nonlinear least-squares method, with corrections for RF excitations and T_1 decay.

4.2.4 MRI Experiments

11 sets of imaging studies were conducted on 6 transgenic mice of prostate tumor (TRAMP) and 3 healthy Sprague Dawley rats. [1-^{13}C]pyruvate and ^{13}C urea were co-polarized by a GE SPINlab clinical polarizer (GE Healthcare, Waukesha WI) for 2 hours for 20-30% polarization using the DNP technique. The ^{13}C biomarkers were rapidly dissolved and injected into the subject animal through a tail vein catheter. For the TRAMP studies, ~350ul bolus was injected over 15(s), whereas the rats received ~3ml bolus over 12(s). In both cases, the sequence was initiated at t=15 seconds since the beginning of injection. All studies were performed on a 3T clinical scanner (GE750, GE Healthcare). The mouse and rat studies were done using custom-built, dual-tuned ^{1}H and ^{13}C mouse and rat coils, respectively. In the clinical

setup, a clamshell coil was used for ^{13}C transmit, and a dual-tuned endorectal coil served as receiver. Dose per unit weight was approximately 10ml/kg for TRAMP mouse, 6ml/kg for rat, both injected with 80mM solution. For patient it was 0.43mL/kg of 250mM solution.

In the patient study, GMP-grade sterile [1-^{13}C]pyruvate was polarized in Spinlab for ~2 hours, yielding 253mM pyruvate solution with 37% polarization. An automatic post-dissolution QC reported the key parameters of pH, radical concentration, temperature and polarization level, and a pharmacist will determine if the bolus meets the safety standards for injection. Dosage was calculated based on patient weight, such that one receive 0.43mL/kg of pyruvate solution. The injection was conducted using a power injector (Spectris Solaris, Medrad, Saxonburg, PA), followed by flush of saline. Total injection time was around 10-15 seconds.

For TRAMPs, the sequence was chosen to provide a spatial resolution of 3.3mm x 3.3mm x 5.4mm, a temporal resolution of 2s, a FOV of 4cm x 4cm x 8.6cm, a spectral BW of 581Hz, and 18 repetitions in 36 seconds. For rats, the FOV and the spatial voxel size were both doubled to provide larger coverage (spatial resolution = 6.7mm x 6.7mm x 10.8mm, FOV = 8cm x 8cm x 17.2cm), whereas temporal resolution and acquisition window remained the same as TRAMP scans. The resolution for clinical scans is as follows (spatial resolution = 8mm x 8mm x 8mm isotropic, FOV = 9.6cm x 9.6cm x 12.8cm). T$_2$-FSE sequence was prescribed for anatomical reference in TRAMP and patient scans, whereas a bSSFP sequence served as reference in rat studies. The voxel volume for mouse, rat and clinical scans were 0.059, 0.480 and 0.512cm^3, respectively.

4.3 Results

4.3.1 Preclinical studies

Eleven sets of hyperpolarized ^{13}C dynamic MRSI were acquired on a total of 6 TRAMP mice and 3 healthy rats using the 3D dynamic CS-EPSI in "FID" mode. 3 TRAMPs had histologically aggressive late stage, and 3 had early stage tumors in this study. Datasets from 19 TRAMPs acquired using the 3D CS-EPSI "DSE" mode were also retrospectively examined.

Combination of MATLAB and SIVIC image processing software (114) allows examination of the fully-3D spectrum voxel-by-voxel, over a specific slice and orientation, or across a given time frame. Overlay of HP-^{13}C images, image-based statistics or modeled metabolic and perfusion indices such as k_{PL} and k_{trans}, with the anatomical reference scans was performed for better lesion identification and analysis.

The arterial input function (AIF) was calculated using both the 3D dynamic CS-EPSI sequence and a 2D RF excitation sequence with CSI readout immediately at the beginning of hyperpolarized ^{13}C urea injection. The AIF curve (Figure 4.2A) shows monotonically increase of signal until reaching maximum at approximately 15 seconds from the beginning of the injection, reflecting the estimated timing of the HP-^{13}C bolus arrival.

For the cancer metabolic studies, the 3D dynamic sequence began at the end of each injection, which was at t=15s. The pyruvate signal displayed its maximum near the beginning of the sequence, and then decreased over time. The decrease was

slightly slowed toward the end of acquisition. The lactate signal, which was present since the beginning of acquisition, increased and reached maximum approximately between t=25-30 seconds. After that, lactate decreased with relatively constant rate until the end of the sequence. HP-^{13}C alanine, which was also excited by the spectral-spatial RF pulse, showed similar behavior to lactate, but instead approached its maximum around t=30-35 seconds. This timeline reflects a physiological process of accelerated aerobic glycolysis in cancerous tissue.

With the 15-second injection period, the bolus arrived at the ROI approximately by the end. Lactate dehydrogenase (LDH) conversion was observed immediately following the arrival of HP compound and rapidly facilitates the reduction reaction from HP-pyruvate to HP-lactate. Pyruvate suffers signal loss from the aforementioned conversion, the RF excitation pulses and the T_1 relaxation, therefore creating the decay in the dynamic profile. The lactate increased at the beginning of the sequence due to the addition of converted pyruvate to the pool. Inversion of the lactate curve labels the timing where the combined loss from progressively increasing flip angle and T_1 relaxation exceeds the contribution from conversion. Alanine was converted from pyruvate as a key step in gluconeogenesis pathway, which is governed by the alanine transaminase. The amount of alanine production was only a fraction of lactate in the TRAMP tumor, while higher alanine level can be seen in the liver of both cancerous and healthy animals.

The rate coefficient for pyruvate-to-lactate conversion, k_{PL}, was computed by applying the metabolic models to the *in vivo* HP-^{13}C dynamic profile. The mean was taken over the manually-selected tumor ROI for the k_{PL} estimation. Simulation

(Figure 4.2B) of the model fitting showed that under a conservative SNR=6, standard deviation for k_{PL} error was less than $\pm0.5\%$ for nominal k_{PL} =0.0300. Comparison of k_{PL} values was also done between two studies conducted using the same late stage TRAMP on the same day. The interval between the injections was 15 minutes, and the percentage of polarization was comparable from the HP dissolutions. k_{PL} from each study was 0.0389 and 0.0407, respectively, which corresponds to 4.4% difference between the two. Such observation demonstrated consistency in the quantitative modeling of metabolic conversion in the presence of data noise.
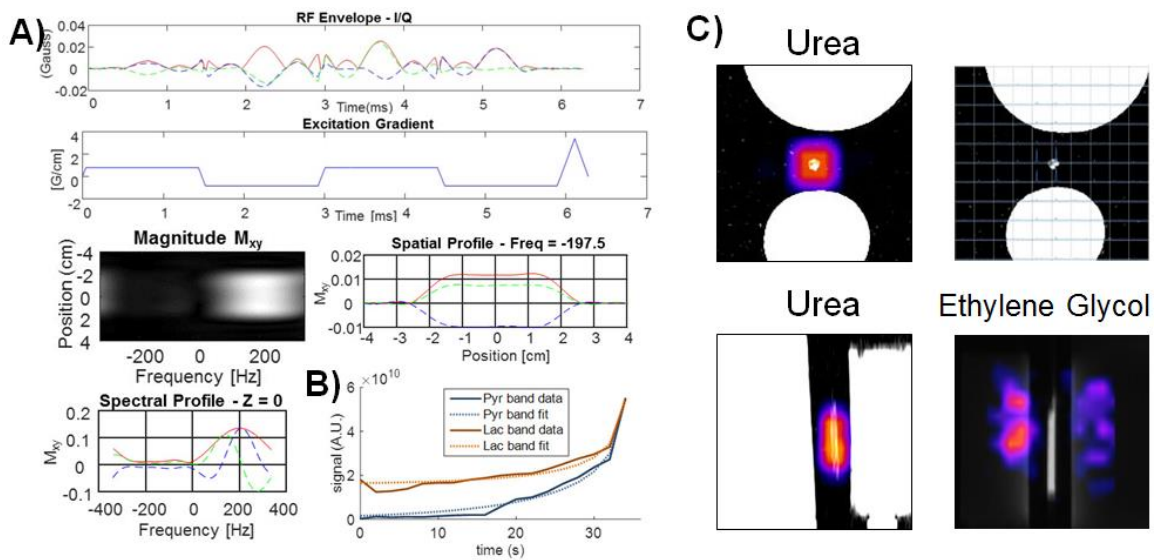
Figure 4.6 A) *The 6.3ms-long RF pulse excites ^{13}C pyruvate and lactate with independent variable flip angles. The peak B_1 of 0.597G is a 67% reduction from that used for preclinical studies **B)** Phantom data excited with progressive-increasing flip RF showed good agreement with simulated profile. **C)** Phantom studies using the clinical setup and sequence shows good spatial homogeneity in a urea syringe.*

In order to investigate the feasibility of imaging larger subjects *in vivo*, we applied the 3D CS-EPSI sequence on 3 healthy rats using the "FID" mode. Rapid urea

perfusion and pyruvate uptake into the kidney was observed since the beginning of the sequence, namely at around ~3 seconds after the end of a 12s-injection. Appreciable amount of lactate exchange was detected there as well (Figure 4.3 and Figure 4.4A). Lactate and alanine production was also found in rat liver (data not shown). These outcomes were highly consistent with the previous observations on HP-^{13}C rat studies.

From TRAMP studies, the mean SNR of total carbon were typically over 30 for tumor, ~100 for vena cava and liver, and ~180 for kidneys across time with ~20-30% polarization on dissolution, as illustrated in Figure 4.5A. Specifically, the mean SNR over the TRAMP tumor was comparable (P>0.3) between the "DSE" mode (61.6±43.6) and the "FID"mode (69.3±28.4). In the rat scans, both FOV and voxel size were doubled from mice. High SNR was found in both rat kidney (172.5±100.3) and liver (85.7±50.1). Such SNR was adequate for both direct data visualization and dynamic modeling of metabolic interconversion. Figure 4.5B depicts the map of lactate temporal AUC overlaid on T_2-FSE reference in a low-grade mouse prostate tumor. Similar HP-^{13}C distribution pattern and pyruvate-to-lactate conversion dynamics was observed from acquisitions using both imaging modes.

One most discernible artifact moving from the "DSE" to "FID" version of the pulse sequence observed was the line-broadening and phasing effect due to the half-echo readout and the shifted TE. Simulation of the spectrum was done using a Lorentzian lineshape. The "FID" mode exhibited a 9.2% wider spectral linewidth than the "DSE" mode in simulation (Figure 4.5D). Actual datasets acquired using "DSE" and "FID" mode were also compared, where spectral linewidth in "FID" mode

was 2.1% wider than that in the "DSE" mode (Figure 4.5E). The sparsity of the ^{13}C

spectra was preserved by the wavelet-in-time sparsifying transformation, as shown

by the wavelet decomposition of the simulated data in Figure 4.5C. By satisfying the

sparsity condition in our compressed-sensing algorithm, it is ensured the

undersampling and reconstruction scheme used for "DSE" imaging mode is

applicable in the "FID" scenario.
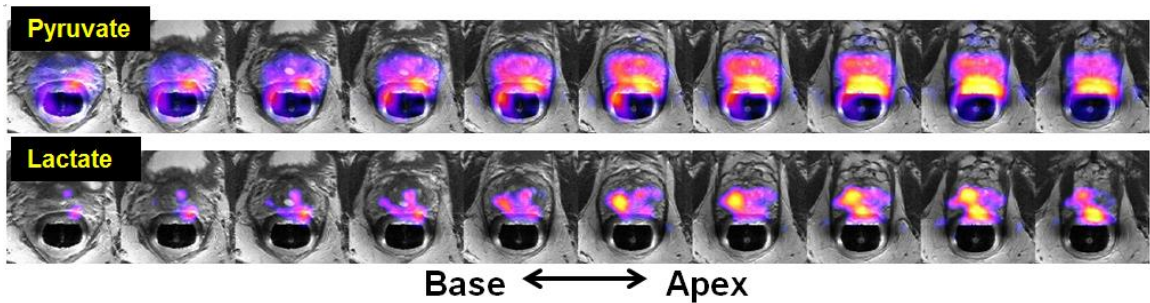
Figure 4.7 *Prostate cancer patient 3D dynamic CS-EPSI data with volumetric coverage from base to apex of HP pyruvate and its conversion to lactate (AUC through time). Spatial resolution=0.5cm3, temporal=2s, 18 timepoints, starting 5s after injection of HP (37%) [1-^{13}C]pyruvate. Region of lactate conversion correlated with the bilateral biopsy data.*

4.3.2 Translation and Patient Acquisition Results

New spectral-spatial RF pulses were generated to account for the limitation

on peak power and the increased B1 field inhomogeneity in the clinical setup

(Figure 4.6A). The new SS-RF pulses has peak B1 of 0.597G and duration of 6.3ms,

which is a 67% reduction compared to our preclinical designs (peak B1 = 1.796G,

duration = 8.9ms). The pulse bandwidth was 793Hz. The ripple was set to less than

1% in both passband and stopband to ensure reasonably homogeneous pulse

profile.
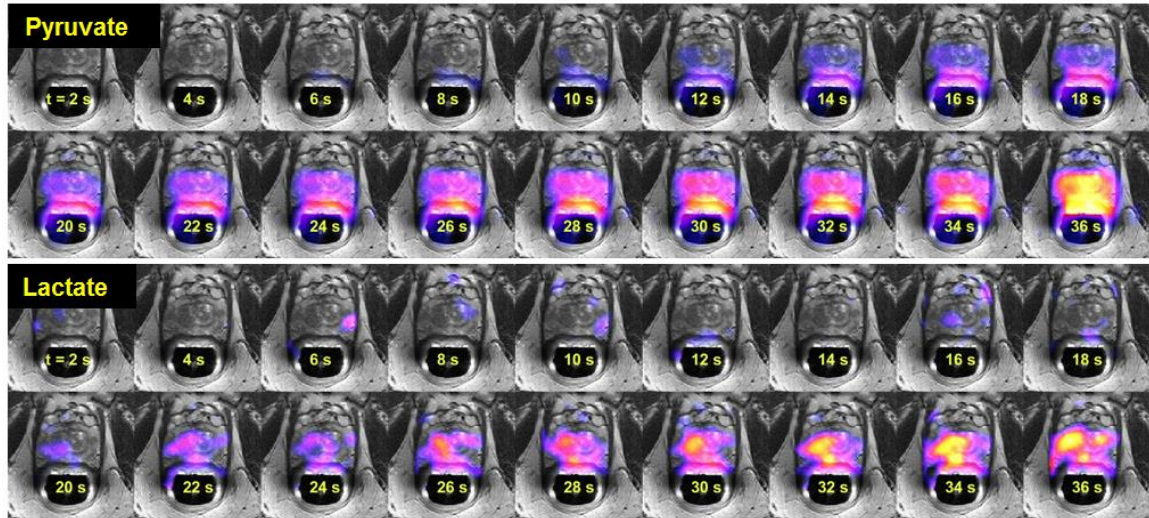
Figure 4.8 *18 timepoints for HP ^{13}C-pyruvate and ^{13}C-lactate from a single slice with bilateral biopsy-confirmed prostate cancer. The acquisition began ~5s after injection. HP-^{13}C pyruvate appears in the prostate at ~10s into the dynamic 3D CS-EPSI acquisition. Conversion to lactate in the cancer regions was observed later at ~20 seconds.*

Phantom studies were conducted using the full clinical configuration with clamshell and endorectal transceive coils. The phantom setup includes a built-in ^{13}C-urea phantom on the coil and two ^{13}C-ethelyne glycol phantoms. The excitation profile on the urea phantom was found to be notably homogeneous, whereas it was less so on ethylene glycol phantoms (Figure 4.6B). Such signal pattern probably resulted from the reduced sensitivity in regions away from the endorectal coil. The phantom data was acquired with our 3D CS-EPSI sequence in conjunction with the RF pulses designed with multiband and variable-flips scheme. On both pyruvate and lactate bands, the phantom dynamics showed good fitting agreement with the simulated signal profile (Figure 4.6C). The apparent SNR of ethylene glycol phantom was 16.1, and of urea phantom was 354 at the final timepoint, where the ^{13}C

compounds were individually excited by the lactate excitation band with a mean flip angle ~40°.
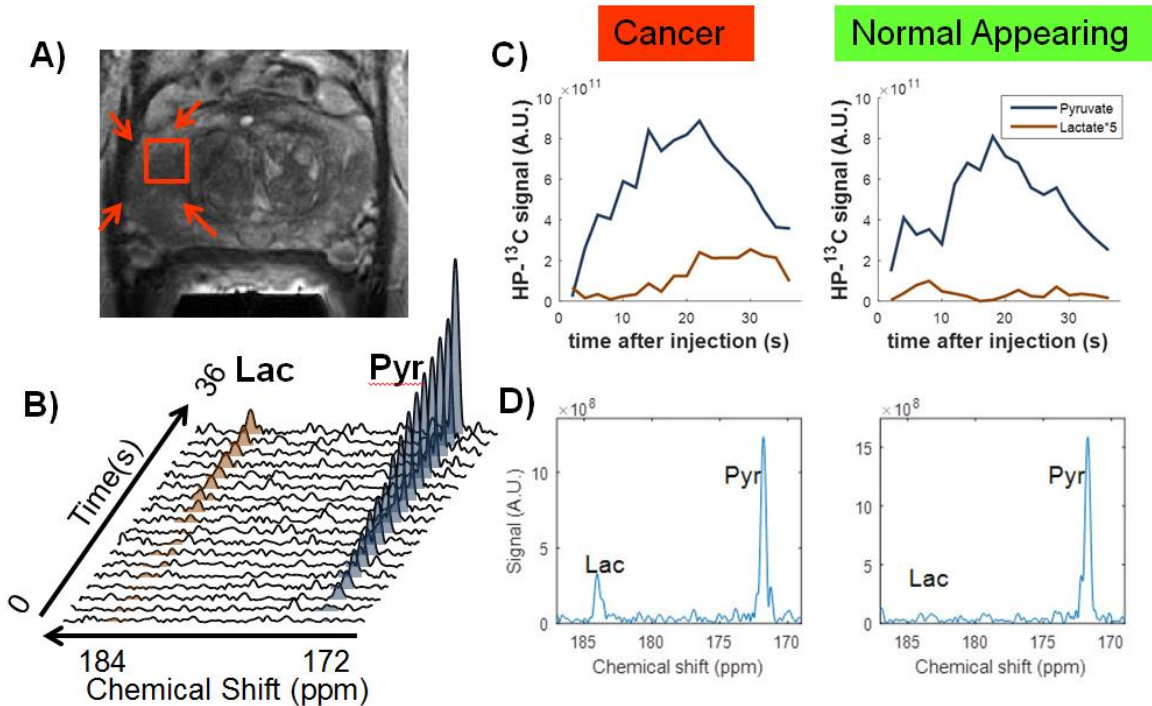
Figure 4.9 The biopsy-proven Gleason 4+3 tumor in the peripheral zone (PZ) exhibited high lactate conversion following HP pyruvate injection. *A)* T2-FSE image showing the tumor voxel selected for the dynamic spectral plot in *B)*. *C)* Dynamic curves (corrected for variable flip angle) are shown with far higher conversion to lactate in cancer compared to normal appearing regions. *D)* Representative spectra for these regions at t = 36 s.

The subject of our first clinical study was a 66 year old male patient with bilateral biopsy-confirmed prostate cancer. Patient 3D dynamic CS-EPSI data demonstrates volumetric coverage from apex to base, with a spatial resolution of 8mm x 8mm x 8mm isotropic (volumetric = $0.5cm^3$), temporal resolution of 2s, and 36s acquisition window. The sequence was started 5s following the injection of sterile [1-^{13}C]pyruvate (hyperpolarized to 37%). Figure 4.7 shows the pyruvate and lactate area under curve (AUC) in the prostate region overlaid on T2w reference

scan. It demonstrated full gland coverage of this new sequence with a FOV=9.6x9.6x12.8cm. While pyruvate intensities outline the prostate gland as well as some surrounding vasculatures, map of lactate conversion correlated with the bilateral biopsy data of this patient. Areas of increased lactate conversion highlight the biopsy-proven multifocal cancer with Gleason 3+4 and 4+3 foci in the PZ. Figure 4.8 illustrates the temporal dynamics in a single-slice data containing bilateral biopsy-confirmed prostate cancer. HP-^{13}C pyruvate is seen to perfuse into the vasculature surrounding the prostate, and the bolus entered prostate around ~10 seconds into the dynamic 3D acquisition. Rapid conversion to lactate in cancerous regions was observed to occur later at ~20 seconds.

The biopsy-proven Gleason 4+3 tumor in the PZ exhibited more than 4x in pyruvate-to-lactate conversion k_{PL} than normal-appearing region, as driven by the high LDH enzymatic activity. Figure 9C and D showed the HP-^{13}C spectra and dynamics in a representative voxel of this tumor versus normal-appearing region. The dynamics curve was corrected for progressive flip angles to reflect the true metabolic activity for visualization purposes. However, it should be noted that T_1 relaxation was not taken into account in this correction. While the raw signal of both pyruvate and lactate appears to monotonically increase until the end of acquisition (Figure 4.9C), the corrected signal shows the pyruvate inversion near ~20 seconds after injection and that of lactate around ~30 seconds and decrease toward the end (Figure 4.9B). The tumor region also corresponds to darker region in T2-weighted FSE image (Figure 4.9A, as encircled by the red box), and high intensity in high b-

value ADC maps (not shown), both of which exhibited good consistency with biopsy and HP-^{13}C findings.
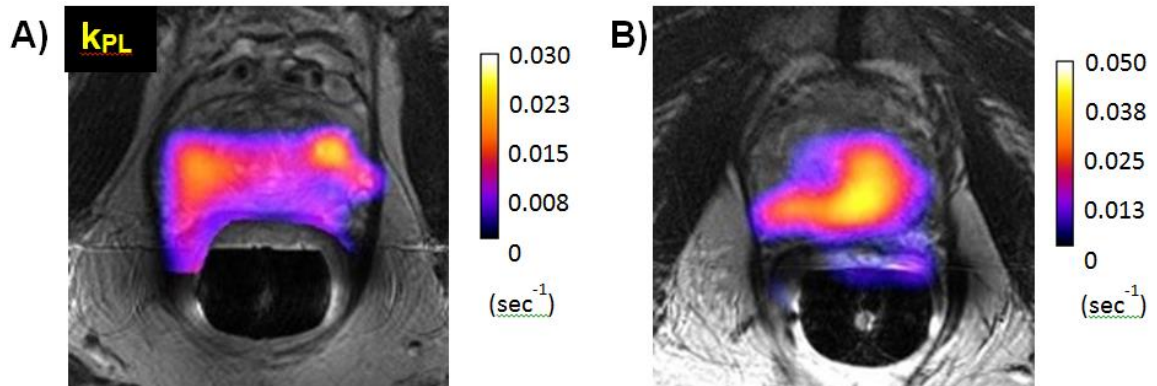
Figure 4.10 *Calculated k$_{PL}$ map from pyruvate-lactate dynamic curves.* **A)** *A bilateral biopsy-proven Gleason 4+3 in the peripheral zone, same region as Figure 7, 8 and 9.* **B)** *A large volume of biopsy-proven Gleason 4+5, 4+4 and 4+3 cancer involving a majority of the left lobe of the prostate and extending into the right peripheral zone.*

The calculated SNR for pyruvate was 104, and for lactate was 10.7 at the last timepoint. The mean SNR over the acquisition for pyruvate was 45.2, and was 6.1 for lactate. The mean SNR over all timepoints for total carbon was 51.3.

4.4 Discussion

The translation from animal to clinical HP-13C imaging presents the unique challenges of larger imaging volume, reduced peak RF power and higher B1 inhomogeneity. To address these challenges, specialized sequence modifications were developed including a low-power spectral spatial RF excitation, "FID" acquisition mode, 3d coverage of the entire prostate with 0.5 cm3 spatial and 2-second temporal resolution for prostate cancer patient imaging. We aimed in this study to characterize the sequence properties and signal behavior transitioning from small animal to larger animal and, ultimately, to human subjects, with the

intent to optimize the performance and robustness of this new 3D dynamic acquisition approach for imaging patients.

One major sequence modification made toward clinical imaging was the new RF pulses. The spectral-spatial RF pulses provide 67% savings in peak B1, which accounts for the reduced peak RF power from clamshell transmit coils in clinical setup compared to preclinical settings. The designed peak B1 was chosen to be around 60% the nominal maximum allowable power for the transmit coil. Such configuration leaves sufficient headroom in transmit power, to make allowance for coil loading factor when scanning different patients. The 1ppm (~30Hz) passband for each metabolite in this spectral-spatial pulse was reasonably wide to account for off-resonance, and the time-bandwidth of 5 provides good compromise between pulse duration, peak power and transition profile sharpness (Figure 4.6A). The phantom signal curve agrees well with the simulated signal profile, which suggests that the excitation pulses can be confidently generated under clinical configuration.

Another major modification to the sequence was the transition from the "DSE" acquisition mode with double spin-echo refocusing pulses to the "FID" mode, where RF excitation was directly followed by EPSI readout. The FID mode was designed to account for the limited peak RF power and reduced B1 field inhomogeneity as offered by the clinical setup. A direct comparison of the signals in TRAMP tumor region (N=7) between DSE and FID mode revealed similar performance in terms of mean SNR levels for total carbon, as shown in Figure 4.5A.

In the mouse study scheme, one main deficiency of the FID mode acquisition compared to the DSE mode is the T2* relaxation, since the latter benefits from the refocusing of magnetization. In DSE mode, nevertheless, the double-spin echo pulses may spoil the HP 13C magnetization at the coil edge, where the RF field rolls off and fails to meet the adiabatic threshold required for refocusing (157). As an overall effect of these factors, the SNR turns out to be similar between DSE and FID mode in the TRAMP mouse acquisition. In human scans, the RF transmit field inhomogeneity is likely worse than the mouse scenario due to increased imaging volume and loading, which can further induce the undesired spoiling. Taking these factors into account, the FID mode should outperform DSE from an SNR standpoint.

Imaging a larger subject using the 3D dynamic CS-EPSI acquisition protocol provides a way to investigate the sequence parameters and signal behavior due to increasing FOV. The rat scans in this study utilizes a dual-tuned rat coil which was about ~ 5 times the volume of mouse coil. The FOV and voxel size were doubled both in the phase encode and EPSI readout direction (in-plane resolution: mouse 3.3mm and rat 6.7mm, axial resolution: mouse 5.4mm and rat 10.8mm), giving 4x voxel volume. The total injection dose also increased by approximately 6 fold. Unfortunately, rat received lower HP-13C dose per unit weight (around 60% that of TRAMP). In addition, the larger coil volumes inherently leads to decreased sensitivity compared to mouse setup. The other sequence parameters (e.g. flip angles, temporal resolution and undersampling ratio) remained the same, and "FID" mode was applied. Pyruvate metabolism is well represented in rat kidney just like in TRAMP mice tumor (Figure 4.4). Also, the SNR did not deteriorate in rat relative to

mouse (Figure 4.5A). As such, transitioning to rats scans revealed the key elements to scaling up the sequence, and this protocol showed robustness in signal and image quality with larger imaging subjects and coils.

A 2-second temporal resolution was chosen for clinical protocol, identical to that in TRAMP studies. In TRAMP scans, this consistently provided >30 (apparent) SNR for both pyruvate and lactate (~20-30% polarization), which translates into less than 3% error in quantitative metabolism models (Figure 4.2B). For the clinical study, the pyruvate SNR was similar to TRAMP (~30), while lactate SNR was relatively lower (~6). Two primary sources of error contribute to the apparent SNR of this 3D CS-EPSI acquisition, which are the data noise and the inherent error contributed by CS reconstruction. Referring to Fig.3 of the paper by Larson et al.(12), the reconstruction error was less than 0.001 for SNR of 30, and less than 0.007 for SNR of 6. Therefore, it can be concluded that the data noise was dominant source of error under both clinical and mouse scheme. SNR improvement is theoretically possible through a longer temporal resolution, since it results in effective signal averaging and decrease of undersampling ratio. Nevertheless, a longer temporal resolution also creates temporal blurring, and introduces ambiguity on timing of dynamic curve, which can seriously hurt quantitative modeling. Under the current clinical settings, 2-second temporal resolution offered a good compromise between SNR and timing accuracy.

In the patient research studies, the acquisition began at 5 seconds after the end of injection, compared to the 15 second in mouse studies, while both shares the same 2-second temporal resolution. The acquisition time window covered both

bolus dynamics and pyruvate-to-lactate conversion in human prostate cancer, while the TRAMP scan focuses more on the latter half of the pharmacokinetics that mainly reflected pyruvate metabolism. Since the bolus delivery was more rapid in small animals, and a reference AIF was relatively easy to estimate using the HP 13C urea through arterial voxels, the sequence can be configured to put more focus on net metabolism by acquiring at a delayed window for TRAMP. Due to absence of arterial coverage or perfusion markers in clinical imaging, it is more challenging to account for these pharmacokinetic parameters. Additionally, the circulation and bolus delivery is generally slower in human versus small animals. Therefore, acquiring at a window that accounts for both pyruvate infusion and conversion may ultimately help clinical quantitation of prostate tumor metabolism.

Translation of 3D dynamic HP 13C MRSI has offered a way to quantitatively analyze metabolism in human prostate cancer. But just as importantly, the capability to image biochemical processes and visualize diseases with ultra-high spatiotemporal resolution has opened the door to many potential HP 13C translational and research applications. For instance, high lactate/pyruvate ratios were detected in various cancer types such as xenografts of human brain tumor (45), renal carcinoma cells (6), and breast tumor xenografts (145). And modulation of lactate production were found in tumor subjected to chemo (42) and targeted therapy (158). Besides cancer, HP 13C imaging has been used to study kidney urea transporters (112), diabetes and gluconeogenesis (159), cardiac diseases (160) and neurodevelopment (161).

Further improvements of the HP ^{13}C CS-EPSI protocol is possible through optimization of acquisition, reconstruction and quantitation processes. For instance, optimal flip angle scheme can be designed based on the specific physiological parameter of interest (162). Acquisition window and temporal resolution can be adjusted according to the SNR performance across a cohort of patient data. Investigating different pharmacokinetic models allows one to optimize the representation of the underlying physiological parameters (110,162,163). Coil correction accounts for inhomogeneous receiver profile (164), and parallel imaging technique can be applied in multi-channel receiving scheme (68,165).

4.5 Conclusions

This new clinical 3D dynamic acquisition method incorporating a novel spectral-spatial RF, "FID" readout and modified CS reconstruction addressed the challenges of larger imaging volumes, reduced available peak RF power and increased B1 inhomogeneity as required for human studies. Scalability in acquisition, reconstruction and quantitation methods was demonstrated by the satisfactory image quality, SNR and contrast between cancer/normal during the transition from mice to clinical studies. In general, the 3D dynamic CS-EPSI exhibited excellent performance and robustness in phantom, preclinical, and patient exams.

Chapter 5 Quantitative Methods for Estimation of Metabolism and Perfusion

5.1 Metabolic Modeling

5.1.1 Introduction to tumor metabolism

Otto Warburg proposed the well-known Warburg effect in the 1920s (4). It describes findings from his experiments that cancer cells produce much higher lactate from pyruvate than normal cells. This elevation of lactate production not only increases under hypoxia, but happens even under aerobic conditions. It is thus given the name "aerobic glycolysis". With the advances of molecular biology and genetics, the metabolic rationale behind the aerobic glycolysis in cancer has come to light. Recent studies suggest that the Warburg effect is fundamental to sustaining cancer cell proliferation, production and incorporation of biomass (3,32). Another important observation is that oxidative phosphorylation remains unaffected by the increase in aerobic glycolysis.
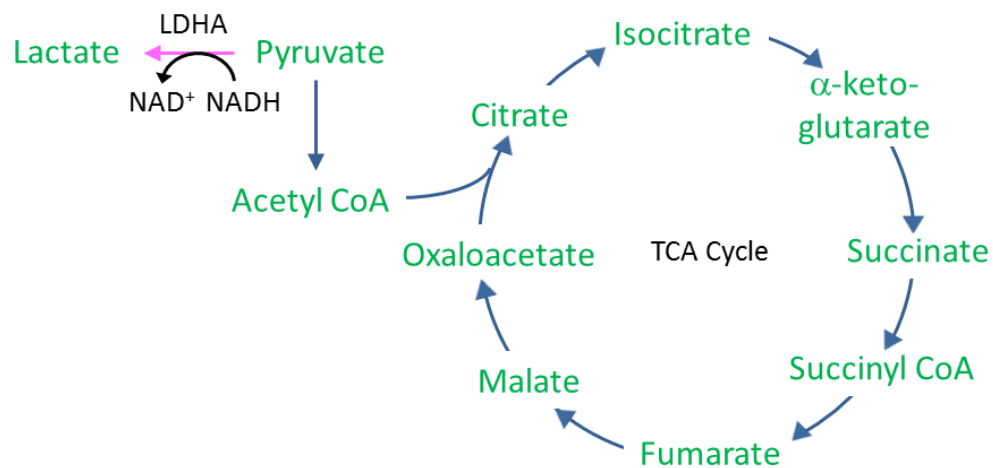
Figure 5.1 *The Warburg effect describes a phenomenon where cancer cells undergo increased conversion of pyruvate to lactate catalyzed by high LDHA enzymatic activity. Recently studies find that Warburg effect is fundamental to cancer survival and proliferation. The increase in pyruvate-to-lactate conversion is present even in the absence of hypoxia, therefore given the name "aerobic glycolysis."*

As further investigations have shown, cancer cells undergo a series of oncogenic mutations that promotes unrestricted proliferation and overcomes survival stress (32). Some of these mutations alter the cellular metabolism. While oxidative phosphorylation maximizes the utilization of energy for ATP production, aerobic glycolysis and its related pathways produces essential precursors for fatty acids, amino acids, and nucleotides, in addition to cofactors such as NADPH. Recycling of acetyl-CoA from TCA cycle is another important reaction for fatty acid synthesis. The production of macromolecules and cofactors provides necessary building blocks for tumor proliferation (Figure 5.1).

In terms of the underlying genetics, several oncogenic mutations can promote the Warburg effect. Oncogenes like AKT and MYC are known to enhance hypoxia-inducible factor (HIF) for increased glycolytic flux under hypoxic conditions (166). Under aerobic conditions, the Src and PI3K pathways can also stabilize the expression of HIF that increases aerobic glycolysis. This section will investigate mathematic models of HP-[1-^{13}C] pyruvate to ^{13}C lactate conversion, which serves as the centerpiece to quantification of aerobic glycolysis in cancer.

5.1.2 Overview of HP ^{13}C metabolism models

The conversion of pyruvate to lactate reflects cellular metabolism in cancer. As is explained in Chapter 3, the pyruvate-to-lactate conversion rate k_{PL} is strongly correlated to LDHA activity and histological grades in prostate cancer. The clinical need to quantitatively interrogating cancer metabolism requires an accurate and

robust measurement of k_{PL} from the temporal dynamics of pyruvate and lactate.

Several types of mathematical models have been proposed to describe *in vivo* HP-^{13}C

dynamics.
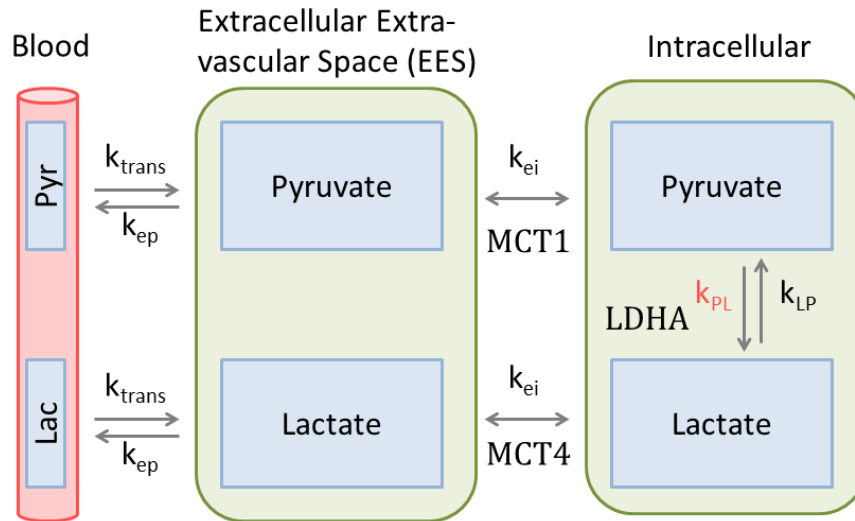
Figure 5.2 *This is a generalized dynamic model that quantitatively describes HP-^{13}C pyruvate metabolism. It consists of 3 physical compartments: blood, extracellular extravascular space (EES), and intracellular space. Each compartment is divided into chemical components (i.e. pools). Many models found in literature, as well as the ones proposed in this dissertation, are either a variant or a simplified version of this generalized model architecture.*

First and foremost, an appropriate model architecture needs to be selected.

In the generalized form of models found in literature, three physical compartments

are often included. These include the arterial compartment, the extracellular

extravascular space (EES) compartment, and the intracellular compartment. Each

physical component is further divided into chemical components such as pyruvate,

lactate, alanine based on the metabolites of interest (Figure 5.2). One major

assumption is that the pyruvate to lactate conversion, catalyzed by LDHA

isoenzyme, only occurs intracellularly. The transport of pyruvate and lactate across

the cell membrane is known to be facilitated by the monocarboxylate transporters

(MCT), including MCT1 and MCT4.
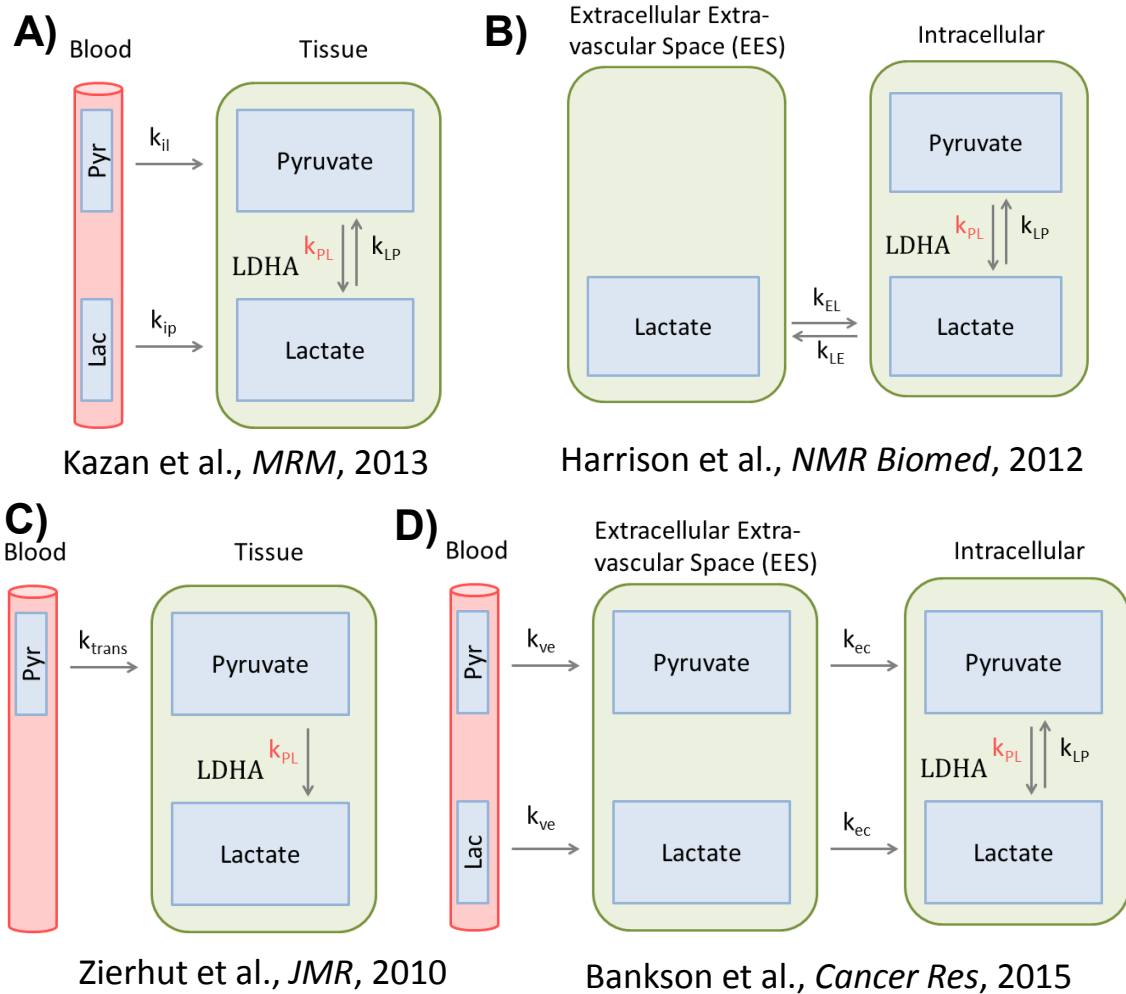
Figure 5.3 A summary of dynamic models in literature. **A)** Kazan's model has blood, tissue compartments and pyruvate, lactate pool in both compartments. (140) **B)** Harrison's model consists of EES and intracellular compartments, with only lactate pool in the EES. (167) **C)** Zierhut's model consists of uni-directional pyruvate-to-lactate flux with a pyruvate AIF. (163) **D)** One of Bankson's models has all 3 compartments and both pools in each compartment. It resembles the generalized model, but with some fluxes assumed to be uni-directional. (142)

Many models in literature are either a variant or a simplified version of this

model architecture. A key determinant is the number of compartments included in

the dynamic model. One very commonly seen simplification is to combine the EES

and intracellular compartment into a "tissue" compartment. Under some specific

circumstances, the blood compartment, described by the arterial input function

(AIF), can be omitted. The choice between inclusion or exclusion of blood

compartment and AIF will be discussed in detail in the following sections. Moreover,

in the presence of AIF, whether to apply a measured AIF or a model-based AIF is

another consideration that will also be discussed. One more simplification is to

neglect reverse reactions such as lactate-to-pyruvate conversion rate k_{LP}, if it can be

justified that the reverse conversion rate is insignificantly small compared to the

forward rate.

For instance, the model proposed by Kazan (140) utilizes the AIF and tissue

compartment, and included both pyruvate and lactate pool in the two physical

compartments (Figure 5.3A). Interestingly, Kazan designed a blood chamber to

detect the AIF dynamics, similar to the arterial blood sampling used in DCE imaging.

Harrison's model (167), on the other hand, consists of only the extracellular and

intracellular components, where arterial compartment was excluded (Figure 5.3B).

Furthermore, Harrison and colleagues only included lactate in their extracellular

compartment, arguing that extracellular pyruvate does not benefit modeling of k_{PL}.

The model proposed by Zierhut (163) is similar to Kazan's model, except that the

arterial compartment only consists of pyruvate (Figure 5.3C). This model choice is

based on the assumption that very little lactate exists in the arterial compartment,

which is reasonable given that lactate conversion primarily only occurs in

tissue/tumor, and ignoring the excreted lactate that enters recirculation. Bankson

explored a few different types of models and compared the goodness of model and fit using the Akaike's Information Criterion (AIC) (142). They discussed the simplest two-site exchange model using only pyruvate-lactate exchange within a single tissue compartment, and a two-compartment model with arterial and tissue compartment similar to Kazan's version. Finally, Bankson and colleagues also investigated a 3-compartment model (Figure 5.3D) similar to the generalized model in Figure 5.2.

The selection of free versus fixed parameters is also an important consideration. The number of free parameters will ultimately affect the condition of fit between model and data, and the relative goodness of a model can be determined using the AIC, as will be explained in the following section. Some common parameters can be set to constant based on assumption or actual measurements if the parameter is sufficiently consistent across the datasets of interest. Some examples of parameters that can potentially be kept constant include the T_1 relaxation time, the perfusion time delay t_0, and reverse perfusion rate k_{ep}. Some compartment and associated parameters are completely omitted in certain cases, as is seen in the abovementioned literature. For example, the AIF, the reverse reaction rate k_{LP}, and the clearance of lactate from tissue. The partial voluming within a voxel is another factor that tends to be omitted, whereas a few works still incorporate the fractional volume v_e.

Recently, Maidens et al. proposed a model-free k_{PL} estimation method that also exhibits very promising outcomes (162). However, this class of methods is out of scope of this work and will not be discussed here.

5.1.3 The two-site exchange model

In the TRAMP prostate cancer studies in Chapter 4, the two-site exchange model was selected as the standard for k_{PL} estimation (110). The two-site model can also be viewed as a special form of the generalized model mentioned in 5.1.2. In this model, only the tissue compartment was accounted for. All pyruvate and lactate are assumed to be confined to the tissue compartment, and the arterial input and metabolite clearance are not included in such model architecture. The two-site model can be expressed in an elegant and simple mathematical form, written here in ODE format.

$$\frac{dM_{pyr}(t)}{dt} = -(\rho + k_{PL} + k_{PA})M_{pyr}(t)$$

$$\frac{dM_{lac}(t)}{dt} = k_{PL}M_{pyr}(t) - \rho M_{lac}(t)$$

where M_x is the net longitudinal magnetization of metabolite x, k_{PL} is the rate of pyruvate-to-lactate conversion, and ρ is the intrinsic relaxivity of HP-^{13}C metabolites. For the sake of simplicity and model robustness, the relaxivity ρ is assumed equal among metabolites, and reverse conversions are neglected.

The equations above account for the magnetization evolution in between adjacent RF excitations. Jointly solving the ODEs gives

$$M_{pyr}(t) = M_{pyr}(t_0) \cdot e^{-(\rho+k_{PL}+k_{PA})(t-t_0)}$$

$$M_{lac}(t) = M_{lac}(t_0) \cdot e^{-\rho(t-t_0)} + \frac{k_{PL} \cdot M_{pyr}(t_0)}{k_{PL} + k_{PA}} e^{-\rho(t-t_0)}\left[1 - e^{-(k_{PL}+k_{PA})(t-t_0)}\right]$$

A similar signal equation holds for alanine as for lactate.

The RF excitations can be expressed as

$$M_x{}^+[n] = M_x{}^-[n] \cdot \cos \theta_n$$

$$S_x[n] = M_x{}^-[n] \cdot \sin \theta_n$$

A hybrid continuous-discrete model, described in the equations above, was applied for the HP-^{13}C TRAMP tumor data. The chosen compartmental modeling approach was a trade-off between several factors, and there will be future opportunities for modeling improvements. The first choice was the use of a dynamic acquisition based on double spin-echo refocusing, which provides improved SNR for individual images, but at the expense of saturating some hyperpolarized magnetization at the edges of the RF coil, which is typically at the head and tail of the mice studied. This saturation effect is larger during the injection, when all HP magnetization passes through the edges into the sensitive volume of the coil. Therefore the use of double spin-echo refocusing for SNR improvements required starting data acquisition at the end of injection of hyperpolarized pyruvate resulting in the loss of the initial time points of the dynamic curve. With this acquisition, it was determined that the two-site uni-directional pyruvate-to-lactate model provided the most robust and reproducible fits.

Realistically, the arterial input function always exists and continuously replenishes the pyruvate pool in tissue. The two-site model assumes all pyruvate magnetization is present at t=0 and no AIF further contributes to pyruvate pool. The replenishment of pyruvate from the blood supply appears as a reduced pyruvate loss rate, which is interpreted by the model fit as reduced pyruvate-to-lactate conversion. Lactate production would also be calculated as slower since the

pyruvate arrival was distributed across time rather than being present at the beginning. In addition, disregarding the intra-voxel partial voluming and fractional volume v_e, will likely also lead to lower k_{PL} estimates, as was explained in a recent publication (142). In general, it is important to be aware of these factors that may lead to systematic underestimation of k_{PL} using the two-site model.

There are some other special cases, where the two-site model, with the absence of the arterial compartment and AIF, can be a good assumption as well. For example, the MAD-STEAM spectroscopy published by Swisher et al. (116) utilized a stimulated-echo (STEAM) based pulse sequence. The STEAM sequence features a series of 3 $\pi/2$ pulses, where the crusher gradient in the middle dephases the flowing spins. Therefore, the vascular component is suppressed during the acquisition time window, and the acquired signal dynamic can be considered as purely exchanging.

There is potential to improve the kinetic modeling of metabolism and perfusion by capturing the bolus input signal. In future studies, the tradeoff between double spin-echo SNR and kinetic modeling accuracy using modeling methods will also be investigated.

5.1.4 The two-compartment three-site exchange model

In the two-site model from the previous section, pyruvate and lactate dynamics are considered to be solely a function of metabolic exchange, RF excitation and T_1 relaxation (Figure 5.5B). Per the TRAMP mice sequence protocol, the acquisition begins at the end of the 15 second-injection, when the main pyruvate

95

bolus has arrived at the tumor. The tumor compartment is assumed to be at a quasi-equilibrium state where pyruvate inflow and clearance are approximately at the same rate. The observed signal *in vivo* in TRAMP was that pyruvate signal monotonically decreases, and lactate signal first increased, and then is followed by a decrease. Such signal behavior can therefore be adequately described by the two-site model.

Quantification of pyruvate-to-lactate conversion is a unique and very important challenge in clinical translation of HP-^{13}C imaging. In patient studies, a different type of dynamic model is required to represent the signal, compared to the TRAMP two-site exchange model. Such demand comes from several reasons. First of all, the human subject presents significantly different pharmacokinetics from that of the TRAMP mice. Moreover, the coil setup, the imaging volume, sequence prescription and flip angle design for clinical studies all deviate from that of mice studies. Specifically, the clinical protocol mandates that the acquisition starts at 5 seconds after the end of injection, which was administered from antecubital IV. With the time delay for the bolus to travel through circulation to prostate, it was found that such acquisition scheme captures a Lorentzian shape of pyruvate bolus, with both the ascending and descending portions. The 1D and 2D MRSI data presented by Nelson et al. suggests that the pyruvate bolus appears at around 10-15 seconds after the end of injection, and reached maximum around 20 seconds. Lactate signal, on the other hand, peaked at approximately 30 seconds.

A two-compartment three-site model has been proposed to account for the bolus effect. In this case, the blood and tissue compartment were included in the

proposed model (Figure 5.5B). However, only the pyruvate pool (AIF) was accounted for in the blood compartment, with the assumption that lactate was solely produced in the tumor. In order to derive an analytical form of the model, the AIF was assumed to be a boxcar function, defined by injection rate r_0, similar to the three-site model reported by Zierhut et al. (163)

The proposed model can be written in the following ODE form

$$\frac{dM_{pyr}(t)}{dt} = r_0 \cdot e^{-\rho t} - (\rho + k_{PL} + k_{PA})M_{pyr}(t)$$

$$\frac{dM_{lac}(t)}{dt} = k_{PL} \cdot M_{pyr}(t) - \rho \cdot M_{lac}(t)$$

$$\frac{dM_{ala}(t)}{dt} = k_{PL} \cdot M_{pyr}(t) - \rho \cdot M_{ala}(t)$$

where M_x is the magnetization of metabolite x, and ρ is the intrinsic relaxation of HP-^{13}C compounds, $\rho = 1/T_1$.

Solving for the ODEs gives the following analytical form,

$$M_{pyr}(t) = M_{pyr}(t_0) \cdot e^{-(\rho+k_{PL}+k_{PA})(t-t_0)} + \frac{r_0}{k_{PL}+k_{PA}}e^{-\rho(t-t_0)}\left[1 - e^{-(k_{PL}+k_{PA})(t-t_0)}\right]$$

$$M_{lac}(t) = \frac{k_{PL}}{k_{PL}+k_{PA}}\left\{\left[M_{pyr}(t_0) + \frac{k_{PL}+k_{PA}}{k_{PL}}M_{lac}(t_0) + r_0 t - \frac{r_0}{k_{PL}+k_{PA}}\right] \cdot e^{-\rho(t-t_0)} + \right.$$

$$\left.\left[\frac{r_0}{k_{PL}+k_{PA}} - M_{pyr}(t_0)\right]e^{-(\rho+k_{PL}+k_{PA})(t-t_0)}\right\}$$

With this model, we attempted to represent the case in human HP-^{13}C injections, where AIF plays an important role in the dynamics given the human pharmacokinetics, the acquisition scheme, and time frame. Recently, Cunningham et al. published a HP-^{13}C human cardiac study (46). Given the rapid circulation and

perfusion in human heart, the bolus effect would presumably be crucial for quantification there as well.

5.2 Perfusion Modeling

5.2.1 Application of Tofts models on HP-^{13}C perfusion imaging

Cancer hypoxia is known to be a strong promoter of aggressiveness, and is associated with breakdown of extracellular matrix and resistant to chemotherapy. Imaging cancer blood flow and perfusion has great clinical value, and could serve as a predictor for prognosis and therapeutic response. Tofts formulated a mathematical model (115,168) for quantitative measurement of *in vivo* perfusion. To this date, the Tofts model still serves as the "Gold standard" for perfusion, and has found extensive usage in different forms of perfusion imaging and pharmacokinetics, such as PET and DCE-MRI. This section includes a discussion of the application of Tofts model in the context of HP-^{13}C perfusion imaging using HP-urea.

The Tofts model considers a single tissue compartment and an arterial input function (AIF). Perfusion is described as the tracer diffusion through the endothelium of blood vessels and entering the tissue. The forward and backward perfusion /permeability coefficients are denoted as k_{trans} and k_{ep}, respectively. The perfusion phenomenon can then be formulated as

$$\frac{dC_{tissue}(t)}{dt} = k_{trans} \cdot C_{blood}(t) - k_{ep} \cdot C_{tissue}(t)$$

where $C_{blood}(t)$ and $C_{tissue}(t)$ are the tracer concentration in vasculature supplying the tissue, and the tissue itself, respectively. $C_{blood}(t)$ is also known as AIF. k_{trans} is the product of extraction fraction E and flow F, that is k_{trans} = E·F. The extraction fraction $E = (1 - exp(-PS/F))$.

The solution of the concentration equation becomes

$$C_{tissue}(t) = k_{trans} \cdot C_{blood}(t) * \exp(-k_{ep} \cdot t)$$

If the fractional volume v_e is to be considered, the equation becomes

$$C_{tissue}(t) = (1 - v_e)k_{trans} \cdot C_{blood}(t) * \exp(-k_{ep} \cdot t) + v_e \cdot C_{blood}(t)$$

The fractional volume, or the fraction of blood volume in tissue is connected to the perfusion coefficients as v_e = k_{trans}/k_{ep}. For DCE imaging, the signal curve can be uniquely mapped to concentration curve, leading to straightforward parameter fitting. However, the signal mapping is nonlinear and may induce ambiguity in the fit, as will be discussed in Section 5.4 .

Although positive proportionality exists between the HP-^{13}C signal and concentration, the signal equation is not as simple as it appears, since the magnetization loss needs to be accounted for due to RF excitation and T1 relaxation. The magnetization equation for HP tracers can be written in a similar form to the concentration equation

$$\frac{dM_{tissue}(t)}{dt} = k_{trans} \cdot M_{blood}(t) - (k_{ep} + 1/T_1) \cdot M_{tissue}(t)$$

generating the solution (169)

$$M_{tissue}(t) = k_{trans} \cdot M_{blood}(t) * \exp[(-k_{ep} + 1/T_1) \cdot t]$$

Note: it needs to be considered that $M_{blood}(t) = C_{blood}(t) \cdot \exp(-t/T_1)$ when model-based AIF was used.

Similar to the metabolic modeling, the perfusion model utilizes a hybrid continuous-discrete model to account for the RF excitation loss and magnetization evolution in each TR.

5.2.2 Model-based AIF

A well-defined arterial input function is of great importance to accurate quantification of perfusion. One strategy of defining AIF is to use a mathematical function that mimics the empirical or population-mean AIF across subject animals or humans.

The simplest form of model-based AIF is probably a boxcar function. The boxcar function is defined as

$$C_{blood}(t) = \begin{cases} r_0 & t_0 < t < t_0 + t_a \\ 0 & \text{elsewhere} \end{cases}$$

The associated parameters are the rate of AIF r_0, the bolus arrival time t_0, and the duration of AIF t_a. The model parameters can either be fixed to an empirical value, or be as a free parameter in the fit.

For HP-^{13}C urea in mouse cancer model studies, a Gamma-variate based model was defined by von Morze et al (41,112),

$$C_{blood}(t) = A_0 \cdot (t - t_0)^\alpha \cdot \exp[-(t - t_0)/\beta]$$

with coefficients $\alpha = 3.3$ and $\beta = 4.0$ (Figure 5.4A).

A model-based AIF is less susceptible to noise compared to an AIF measured during study, and is therefore more likely to provide a stable and reproducible fit.

The downside of the model-based method is that it might be more susceptible to study subject variations, different injection protocols, as well as deviations from the population mean. That is, the choice of using a power injector versus manual injection, and the variability within manual injections from each dataset. Also, for those subjects who have an "outlier" AIF that deviates from population mean in shape or duration, the model-based AIF might not represent the true AIF effectively.
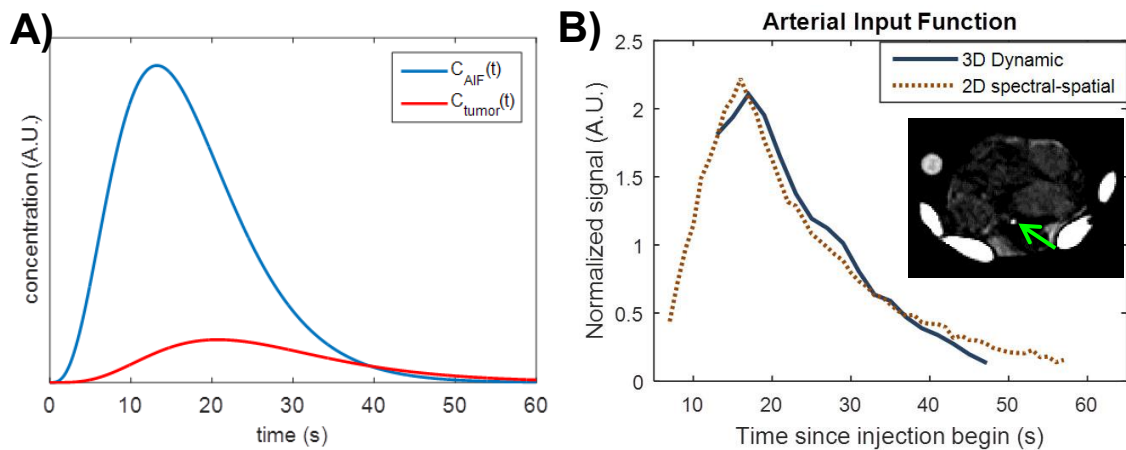
Figure 5.4 A) *Model-based arterial input function using a gamma variate function $C_{AIF}(t)$ and a simulated urea concentration curve $C_{tumor}(t)$ in tumor using $k_{trans} = 120$ and $k_{ep} = 600$ (ml/dL·min⁻¹). **B)** Actual measurements of urea AIF using two different acquisition schemes. The 3D CS-EPSI sequence (11,12) and the 2D-RF pulses (170) give very similar AIF profile after signal normalization. Study was conducted on the same day and same animal.*

5.2.3 In vivo measurement of AIF

In the quantitative perfusion analysis, another strategy to determine AIF is through a direct measurement instead of the model-based AIF. The *in vivo* measurement of AIF can be done by several means, most notably arterial blood sampling and image-derived AIF. The arterial blood sampling method applies an I.V. catheter that continuously samples blood from subject animal/patient. This strategy

is historically known to provide precise AIF measurements in PET imaging (168,171). In terms of PET, the arterial blood sampling works either by placing the catheter directly inside the imaging FOV and directly calculate it from PET images, or use an external Gamma counter. However, arterial blood sampling is invasive and not preferred in the clinic. The image-derived AIF, as the name suggests, requires manual segmentation of a sufficiently large blood vessel on the PET image, and corrections such as hematocrit and partial voluming needs to be applied.

For *in vivo* AIF measurement in HP-^{13}C studies, both arterial blood sampling and image-derived AIF have been previously reported. In the dynamic studies by Kazan et al. (140), they placed an external blood chamber next to their carbon surface coil for blood sampling, and fit the measured AIF curve using different models.

In this project, we attempted to estimate an image-derived AIF using both the 3D dynamic EPSI sequence (11,12) and a 2D-RF excitation sequence (170) on TRAMP mice. The 3D dynamic sequence uses the same protocol as our prostate tumor studies, as described in Chapter 3. The parameters are briefly summarized here, (RF with variable flip angles, multiband excitation, compressed sensing EPSI readout, spatial resolution = 3.3 x 3.3 x 5.4mm, temporal resolution = 2s, acquisition length = 36s, TR = 250ms, TE=150ms). The 2D-RF sequence consists of a RF pulse selective in 2 dimensions, namely x and y, followed by a 1D EPSI readout in the z direction. Some parameters of the 2D-RF sequence include: 5° flip angle, 5mm excitation diameter in x-y, 5mm EPSI resolution along SI direction, and a temporal resolution of 2s.

The injection bolus was 350ul of 80mM HP-^{13}C urea over 15 seconds, with polarization level 20-30%, done manually by an experienced uro-oncologist. Due to the RF spoiling created by DSE refocusing pulses, the 3D dynamic sequence starts at 15 seconds after the beginning of injection. Therefore, only the latter half of the AIF is captured in the acquisition. The 2D-RF sequence, on the other hand, starts at 5 seconds after the beginning of injection.

The blood vessel identified was the inferior vena cava, and the diameter was estimated based on a 3D TOF flow sequence (TE/TR = 2.5/15ms, 256x256 matrix, FOV = 10x10cm, in-plane resolution = 0.39mm, slice thickness = 1.5mm, Flip Angle = 7°). The vessel diameter was estimated to be around 0.7mm. The AIF curve derived from the vena cava of both the 3D EPSI and 2D-RF sequence was shown in Figure 5.4B. The urea signal curve, after normalization, was strikingly similar between the two acquisitions. This is a very interesting finding, since different pulse sequences and flip angle schedules were played between the 3D and 2D acquisitions. First, the similarity can be attributed to the consistency between injection protocols. Moreover, the small variable flip angle at the beginning of the 3D sequence was very close to the 5° constant flip angle provided by the 2D RF sequence. With the afore-mentioned factors in mind, this could suggest that the AIF is relatively consistent among different pulses sequences, given similar flip angle scheme. The findings of the measured AIF can help reduce the need for arterial blood sampling, and even to improve the model-based AIF.

The AIF between the 3D EPSI and 2D-RF sequences demonstrated close similarities. In the future, it may be beneficial to interleave the two sequences, such

that a small-flip 2D-RF sequence can begin at t=0 for bolus tracking and AIF estimation, and the "main" sequence, such as the 3D EPSI, could wait until the bolus arrives (e.g. 15 seconds after beginning of injection) to start. After the start of 3D sequence, the 2D-RF can be interleaved in between TR's for signal normalization.

5.2.4 Quantitative analysis of perfusion and pharmacokinetic parameters

The kinetic modeling of perfusion was performed using HP-^{13}C urea from the co-polarized 3D dynamic pyruvate-urea studies, as described in Chapter 3. The AIF and perfusion curves in tumor were jointly fitted, where the AIF curve was fitted to Gamma-variate function (i.e. model-based). The relation between AIF and tumor perfusion curves gives an estimate of k_{trans} as well as the lumped "reverse" perfusion coefficient k_2. Urea area under the curve (AUC), normalized to kidney urea signal, was also evaluated for each animal to study the distribution of urea in tumor.

In a sense, quantitative modeling of HP-^{13}C perfusion pharmacokinetics is similar to modeling PET radioactive tracers. As opposed to DCE imaging, the signal is relatively "linear" to tracer concentration, barring radioactive decay or T1 relaxation. One difference is the RF excitation pulses in the HP-^{13}C, used to interrogate the tracer, causes additional signal loss in addition to the intrinsic decay and has to be accounted for.

Generally speaking, fitting for perfusion models in TRAMP mice is less reproducible or stable than the pyruvate-lactate metabolism fits. This could be mainly due to the absence of the first (ascending) lobe of AIF, which was not captured for the DSE-based acquisition scheme in TRAMP mice studies. Even with

104

the support of model-based AIF, substantial variations could still arise from difference in timing, bolus signal scaling, bolus shape and duration. If an FID acquisition scheme is used instead of DSE, the acquisition could begin earlier, and capture the first lobe of AIF. Such modification, nevertheless, is at the expense of reduced lactate SNR and increase spectral linewidth.

In patient studies, however, the measurement of perfusion using HP-^{13}C tracers can be more challenging. First of all, approval for clinical study using HP-^{13}C urea is still a working progress. Moreover, whether the coil and hardware setup covers the ascending/descending vena cava is an important question. The sensitive region of prostate, brain or liver ^{13}C coils, for instance, does not cover the vena cava in most cases.

Measuring AIF using the existing pyruvate data is certainly an option in the absence of HP-urea. It is important, however, to note the assumption that no pyruvate is being converted to lactate in the blood vessels. It is known that the pyruvate-to-lactate conversion does occur in red blood cells. Also, blood vessels surrounding the ROI may have partial voluming with tumor or other tissues, adding to the complexity of AIF estimation. In many prostate cancer patients, the reception profile of the endorectal coil includes a major artery around the rectal wall, and the pyruvate bolus was observed to arrive at this artery first, before it appeared in the prostate. The reproducibility of this arterial signal -- and how well it represents AIF, may be an interesting subject for future investigation.

5.3 Assessing Goodness of Models and Fit

5.3.1 The Akaike Information Theorem

Careful selection of kinetic model architecture and free model parameters are key to accurate and robust estimate of metabolic and perfusion parameters. More often than not we face the situation where several mathematical models have been proposed to describe the same dataset. We'd like to select a model that most appropriately represents the dataset, giving reliable and reproducible fitting.

The Akaike Information Theorem was proposed by Akaike et al back in 1974 to determine the relative "goodness" of models (172,173). Shannon's information theory tells us that the information content from a given observation is finite and limited by observation noise(174). Therefore, when selecting a model, it is an important task to minimize the loss of information, such that the model best represents the ground truth. According to the principle of parsimony, the selection of model is a compromise between model bias and variance. A model with too many free parameters will lead to increased variance, while a model with too few parameters will cause increase in bias (173).

Another interpretation approach is that a model with more variables may provide a better "fit" (e.g. a high-order polynomial fits an arbitrary curve better than a low-order polynomial, likely giving smaller R^2). However, higher number of variables also means that the values of these variables are more sensitive to small perturbations. In another word, a small change in the data curve might create rather dramatic variation in the parameter space. A model with too few parameters, on the other hand, gives a less than optimal "fit". That is, the free parameters are biased

due to those "missing" parameters required to represent the data. Fortunately, these free parameters are less susceptible to a small change in data compared to the high-variable case, reducing their variation. Therefore, the goodness of model is a delicate compromise between variance and bias (Figure 5.5A).

Akaike established a relationship between the conventional maximum likelihood and the Kullback-Liebler information (175). The K-L information measures the information loss when approximating the "true" underlying data P with a model Q. The K-L divergence given random variable P and Q is defined as

$$I(p,q) = \int_{\Omega} p(x) log \frac{p(x)}{q(x|\theta)} dx$$

where p and q are the distribution of P and Q, and θ is the parameter vector used in model Q.

Minimizing the expected K-L divergence produces the definition of Akaike's Information Criteria (AIC), with detailed explained in Appendix.

$$\text{AIC} = -2 \log \mathcal{L}(\hat{\theta}|y) + 2k$$

where $\hat{\theta}$ is the maximum likelihood estimate of θ, y are the random samples from function p(x), and $\mathcal{L}(\hat{\theta}|y)$ is the likelihood of $\hat{\theta}$ with observation y. k denotes the number of estimated (free) parameters.

The model that has the relatively lowest AIC has least information loss among all candidate models given observation y. In the AIC formula, the first term represents bias, and the second term denotes variance. With higher number of parameters in vector θ, the log likelihood of ML parameter estimate $\hat{\theta}$ given y would

be higher. However, the second term penalizes the higher number of parameters. This comprises the trade-off between bias and variation.

Since the AIC was derived from an unbiased estimated of I(p,q), correction is needed facing a small sample size. The rule of thumb is that when n/K<40, the corrected AIC formula is required. The corrected AIC formulates as

$$\text{AIC}_C = -2 \log \mathcal{L}(\hat{\theta}|y) + 2k + 2\frac{2k(k+1)}{(n-k+1)}$$

It is important to keep in mind that the AIC only compares and determines the relative "goodness" between the candidate models, and cannot be used to discover the globally best model. Therefore, system knowledge and prior data is of great importance to formulation of models.
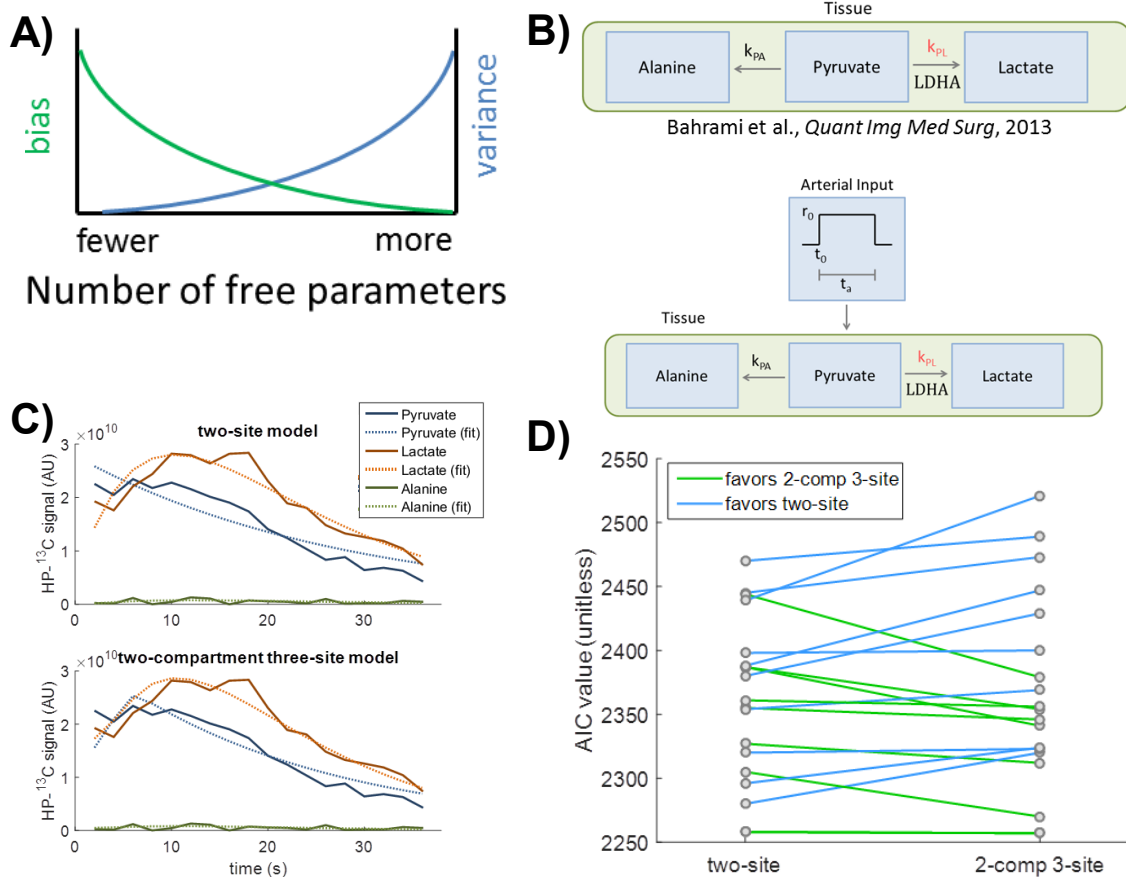
Figure 5.5 A) *The principle of parsimony illustrates the trade-off between number of free parameters in a model. While fewer variables increase the bias, more variables increase the variation.* **B)** *The two candidate models compared for TRAMP. (Top) The two-site exchange model (110), and the two-compartment three-site model similar to Zierhut's. (163)* **C)** *Both two-site and the two-compartment three-site model provides good fit in this set of TRAMP data and similar k_{PL} estimates (0.0373 vs 0.0375)* **D)** *(N=19) AIC for the two models associated with a given dataset was connected by a line. While a blue line represents lower AIC value in two-site model, a green line suggest opposite.*

5.3.2 Goodness of models in TRAMP prostate cancer

Goodness of two candidate models (Figure 5.5B), namely a two-site exchange model similar to Bahrami's (Section 5.1.3) and the a two-compartment three-site model similar to Zierhut's (Section 5.1.4), were compared by retrospectively examining HP-^{13}C dynamics from the TRAMP dataset for both low grade and high

grade tumor (N=19). These two models seem to produce the most reasonable and reproducible fit for TRAMP datasets to our knowledge. The two-site model has 6 free (fitting) variables, namely $M_{pyr}(t_0)$, $M_{lac}(t_0)$, $M_{ala}(t_0)$, k_{PL}, k_{PA}, and T_1. The two-compartment three-site model also has 6, which are k_{PL}, k_{PA}, r_0, t_{offset}, R_{spoil} and T_1. R_{spoil} is the RF spoiling factor caused by double spin-echo pulses at the coil edge. R_{spoil} was not accounted for in the two-site model since the two-site model does not incorporate the dynamics before t_0, the timepoint where acquisition starts.

Figure 5.5D illustrates AIC pairs for the two models in each TRAMP *in vivo* dynamic dataset. Each line pairs AIC values associated with the two models in a given dataset. A blue line represents lower AIC value in two-site model, while a green line suggests the opposite. The absolute values of AIC has little meaning, but comparing the AIC estimates for dynamic datasets between different models reveals the relative "goodness" of the candidate models. Out of the 19 datasets, the two-site model has lower AIC value in 10 datasets, while AIC for the three-site model is lower in 9 of them. From the fit in Figure 5.5C, both methods performs reasonably well and provided similar measures of k_{PL}, the quantitative parameter of question in metabolism. The AIC suggests that the two-site and three-site model have similar performance whether in the high-grade or low-grade tumor. Since no significant evidence favors either model, the two-site model was empirically chosen as the model of use for the TRAMP tumor studies.

The modeling strategy for TRAMP imaging is heavily dependent on the acquisition scheme. In the TRAMP mouse studies we used a dynamic acquisition based on double spin-echo refocusing, which provides improved SNR for individual

images, but at the expense of saturating some hyperpolarized magnetization at the edges of the RF coil, or at the head and tail of the mice studied. This saturation effect is larger during the injection, when all HP magnetization passes through the edges into the sensitive volume of the coil. Therefore the use of double spin-echo refocusing for SNR improvements required starting data acquisition at the end of injection of hyperpolarized pyruvate resulting in the loss of the initial time points of the dynamic curve.

In this case, the two-site exchange model accounts for the net conversion from pyruvate to lactate, and also provides an estimate for relaxation T_1. The initial magnetization $M_x(t_0)$ for each metabolite x is also an estimated parameter, allowing no assumption to be made about the dynamics prior to the sequence begins (i.e. $t<t_0$). Once the sequence begins, the pyruvate curve will be monotonically decreasing due to the assumption that the main pyruvate bolus has arrived at the tumor, and the AIF was omitted. This speculation is consistent with the TRAMP dynamics that we acquired, some of which can be found in Chapter 3. However, the monotonic decreasing pyruvate does not necessary suggest that no pyruvate inflow occurs after the acquisition begins. Instead, it is possible that the net pyruvate signal loss, as a combination effect of pyruvate-to-lactate conversion and T_1 relaxation, is higher than the contribution of pyruvate from blood flow. The lactate signal, on the other hand, tends to first increase, followed by invert and decrease till the end of acquisition. The two-compartment three-site model provides a simplistic boxcar input function, a timing offset t_{offset} to account for the timing of bolus arrival, conversion rate constant k_{PL} and k_{PA} similar to the two-site model, and also the

relaxation T_1. One necessary assumption for the three-site model is that no HP-^{13}C is present until the beginning of bolus arrival. An additional term is the RF spoiling factor R_{spoil}, which accounts for the extra signal loss after acquisition start due to RF spoiling resulting from DSE refocusing pulses. If an FID-based acquisition mode is applied without refocusing, the R_{spoil} term would not be necessary.

In summary, the three-site model offers higher flexibility on pharmacokinetics, including bolus size and timing, while the two-site model focuses more on the net metabolic conversion.

5.3.3 Selection of Models in Human Prostate Cancer

As described in 5.1.4 , the human HP-^{13}C acquisition captures a strong bolus profile, which necessitates the inclusion of AIF in the models. Such AIF profile was found not only in prostate, but also in the recently published HP brain and cardiac data. One option is the two-compartment three-site model (Zierhut-like) we proposed as an alternative to the two-site exchange model in TRAMP studies (163). Although the three-site versus two-site AIC was not directly compared using the clinical data, one can safely assume that a three-site model will outperform a two-site model. This is due to the strong AIF that can be visually identified, where the two-site model omits the existence of such AIF.
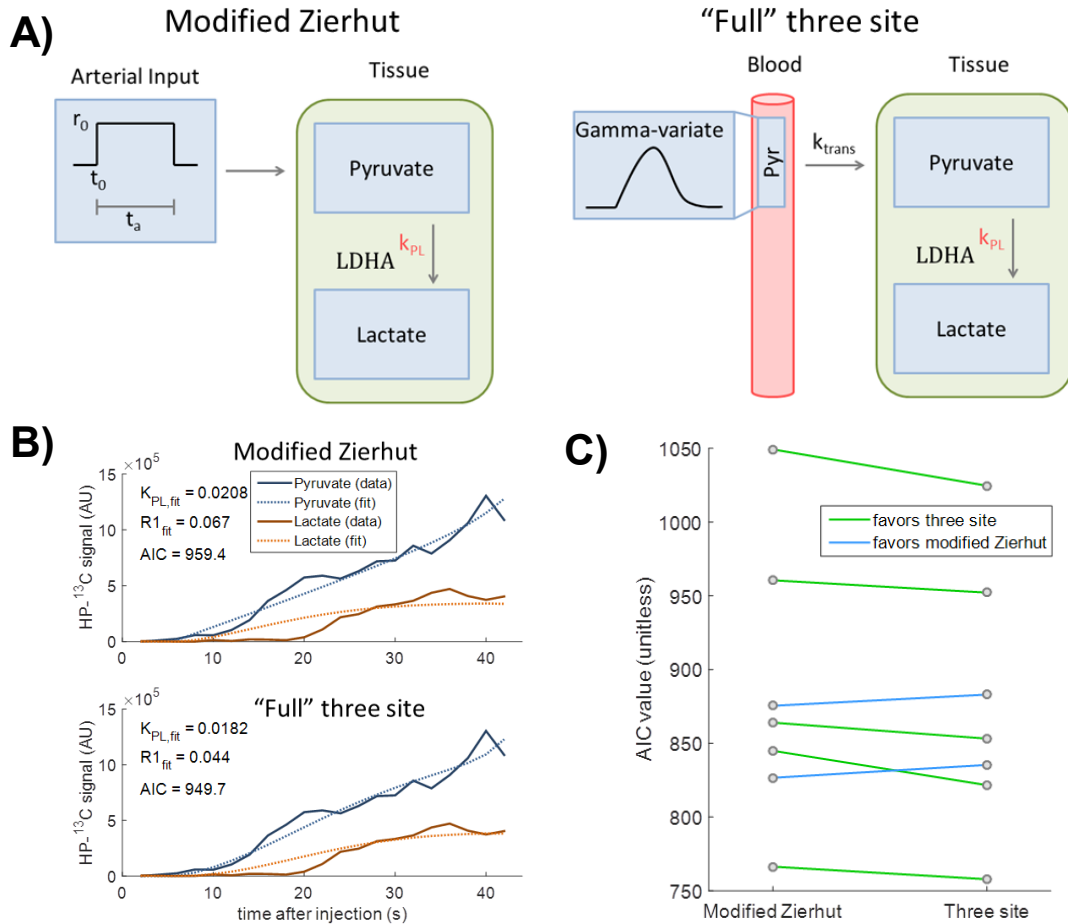
Figure 5.6 A) *This figure summarizes the two candidate models compared for the phase II human prostate data acquired using the 3D CS-EPSI sequence. The modified Zierhut model is also a candidate for TRAMP mice studies, while the full three site model includes a Gamma-variate AIF in blood compartment.* ***B)*** *The modified Zierhut model and the full three-site model both provide good fit for human prostate cancer with similar k_{PL} estimates.* ***C)*** *AIC comparison from human datasets (N=7). The full three-site model has a slight advantage over the modified Zierhut model, but the latter still performs reasonably well with good reproducibility.*

The free parameters in Zierhut-like model (Figure 5.6A, left) can be simplified to k_{PL}, r_0, and T_1. Since alanine was not considered the human acquisition, and RF spoiling is not an issue with the disabling of DSE refocusing k_{PA} and R_{spoil} are omitted along with the alanine compartment. At the first glance, the Zierhut-like

113

model provides good fits with reasonable k$_{PL}$ numbers. Nevertheless, to investigate whether we run the risk of oversimplification, a more complex "full" two-compartment three-site model was also proposed for comparison.

First of all, in the "full three-site" model (Figure 5.6A, right), a Gamma-variate AIF was applied in place of the boxcar function in the Zierhut-like model. The Gamma function is identical to what was discussed in the perfusion section, but with coefficient $\alpha = 2$ and $\beta = 10$, chosen empirically based on the clinical data from phase I and phase II clinical studies. Moreover, both forward and reverse perfusion coefficient was included to model the exchange between blood and tissue compartment.

This model structure leads to three-site exchange equations

$$\frac{dM_{pyr,tissue}(t)}{dt} = k_{trans} \cdot M_{pyr,blood}(t) - \left(\rho + k_{PL} + k_{ep}\right)M_{pyr,tissue}(t)$$

$$\frac{dM_{lac}(t)}{dt} = k_{PL} \cdot M_{pyr,tissue}(t) - \rho \cdot M_{lac}(t)$$

where M$_{pyr,blood}$(t) denotes the AIF, M$_{pyr,tissue}$(t) is the tumor pyruvate magnetization, and k$_{trans}$, k$_{ep}$ are forward and reverse perfusion coefficients, respectively. In this particular case, an analytical solution cannot be reached due to the gamma-variate AIF. Fortunately, a numerical approximation can be evaluated using MATLAB methods. Similar to any other type of model fit, the RF excitation has to be accounted for in each TR as a signal loss mechanism.

Figure 5.6C depicts the AIC comparison between "full three-site" and the Zierhut-like simplified three-site models using the clinical prostate dynamics we acquired so far (N=7). While the green line connects an AIC-estimate pair from a

single dataset where the full three-site model has lower AIC, the blue line shows a

pair where the modified Zierhut model has lower AIC.

Out of the 7 datasets we have so far, 5 of them favor the full three-site model,

while 2 favor the Zierhut-like model. Therefore, with the current data it appears that

the "full" three-site model has a slight edge over the Zierhut-like model. However,

the AIC difference, ΔAIC, is small between the two models. Moreover, the fits from

the two models (Figure 5.6B) appear visually similar. Such outcomes suggest that

their performance is not significantly different. It also suggests that a Zierhut-like

model, using a boxcar input function and 3 free parameters, is a reasonable model

structure which does not oversimplify the *in vivo* dynamics. The full three site

model, while providing better fit, is penalized by the 5 parameters that lead to

increased parameter variation.

At this stage it is still too early to decide on a particular model for clinical

studies, and there is certainly room for improvements with both model architecture

as well as choice of free parameters. As importantly, more data points need to be

collected for clinical model development.

5.3.4 Summary of model selection

Kinetic modeling lies at the heart of quantitative analysis in HP-^{13}C dynamic

imaging. Dynamic models incorporate fundamental parameters such as timing

differences and offsets in bolus injection, tracer delivery, and metabolic conversion

during the acquisition. Careful selection of a candidate model ensures faithful

representation of the underlying information in the dynamic dataset. Flexibility is offered through choice of free parameters to enter the fitting operation.

The Akaike's Information Criterion provides a statistical method to evaluate the "goodness" of candidate models based on real data. Given real-world datasets, a model that consistently provides lower AIC estimates than others indicates better performance. Bankson and colleagues compared 3 different model architectures using a variety of animal tumor models (142). They concluded that the two-compartment and three-compartment models perform better than a simple two-site exchange one, evaluated based on AIC. Nevertheless, the characteristics of dynamic data are heavily dependent on the animal model, MRI instruments, the experimental setup, the pulse sequence, and the acquisition strategy. Based on our investigation, the two-site and Zierhut-like three-site model both work well for the HP-^{13}C TRAMP tumor dynamics. For clinical prostate studies, the "full" three-site model seems to perform slightly better than the Zierhut-like model, but no significant difference was found, and the Zierhut-like model can serve as a reasonable simplification for the full model. The model-free estimation method, like the one recently discussed by Maidens et al., may also be beneficial (162).

In general, more data points need to be collected, where the variation over population in pharmacokinetics such as AIF shape, perfusion and delivery timing can be factored in for model improvements. The HP-^{13}C dynamic modeling in other targets such as brain, heart and liver would also need to be investigated; as such organs can exhibit different pharmacokinetics and rate of pyruvate-to-lactate conversion compared to the prostate.

5.4 Comparison of HP-[13]C Urea Perfusion and DCE Imaging

5.4.1 Basics of dynamic contrast enhanced imaging

Dynamic contrast enhanced MRI (DCE-MRI) is a common way to image blood flow, perfusion and permeability (91,93). The DCE-MRI uses a T1-weighted imaging sequence and the signal enhancement provided by Gadolinium (Gd)-based contrast agents. The Gd tracer creates a T1-shortening of protons, and therefore altering the native contrast in vivo. The amount of T1-shortening is a function of Gd concentration. Since Gd is an extracellular agent and technically no cellular uptake takes place, DCE imaging can serve as a good measurement of perfusion and vascular permeability in tumor or in a given tissue, in the general sense.

The T1-shortening given a Gd concentration C can be expressed as

$$R_1 = R_{10} + r_1 \cdot C$$

where R_{10} and R_1 are the intrinsic and the Gd-enhanced relaxation rate, respectively, and r_1 is the relaxivity. The definition of relaxation rate R_1 is simply $R_1 = 1/T_1$. The signal equation can be expressed as (176)

$$S = S_0 \cdot \frac{(1 - E_1) \sin \theta}{1 - E_1 \cos \theta}$$

where S and S_0 are the contrasted and intrinsic (uncontrasted) signal from a given voxel, respectively. E_1 is defined as a function of TR and T_1 as $E_1 = \exp(-T_1/TR)$, and θ is the flip angle played at acquisition. Note that S_0 was acquired with θ = 90° with sufficiently long TR for T1 recovery, and has to be back-calculated if a flip angle other than 90° was used.

DCE signal conversion curve

$r_1 = 4.5 \ (s^{-1} \cdot mM^{-1})$
Hct = 0.42
$T_{1,0} = 1.4 \ (s)$
TR = 8.7 (ms)
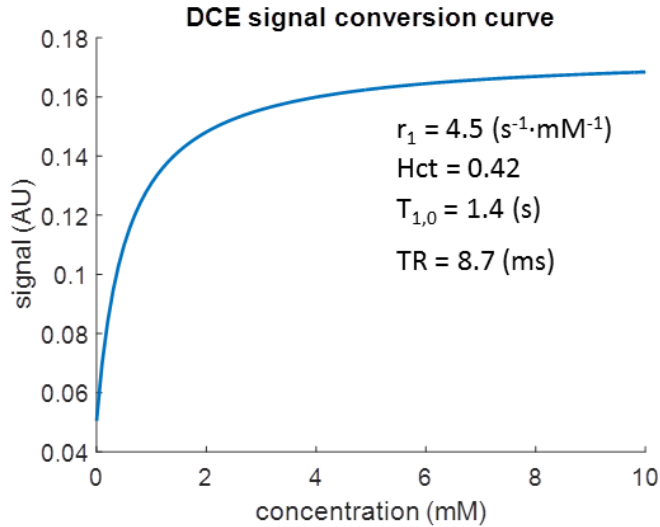
Figure 5.7 *DCE signal curve illustrates the nonlinear relation between Gd tracer concentration and T1 signal enhancement. The nonlinearity is particular an issue with AIF measurements, where high Gd concentration is present and the conversion curve is almost "flat".*

On the signal modeling end, the canonical Tofts model (as formulated in the urea perfusion section) is typically applied, along with the signal-intensity versus Gd-concentration curve as characterized above (Figure 5.7). One confounding factor of DCE imaging, nevertheless, is that the signal intensity is not directly proportional to Gd tracer concentration. Especially in the major arteries, where high concentration of Gd is present, the Gd concentration maps onto a plateau region on the signal-concentration curve, creating ambiguity in the AIF fit and therefore increases overall instability.

5.4.2 DCE imaging on transgenic mouse prostate tumor at 3 Tesla – Methods

DCE imaging was performed on several TRAMP mice on the same day of HP-^{13}C studies (N=4). The Gd-tracer used for the DCE study was Magnevist Gd-DTPA

(Bayer Pharmaceuticals, Wayne NJ) diluted to 0.17M. 100ul of the diluted tracer was injected through the same tail vein catheter as for the HP-^{13}C studies, immediately followed by 150ul of saline flush. The injection begins around 30 seconds after the acquisition begins, and ends around 45 seconds. The total injection duration for Gd and saline was ~15 seconds. The DCE acquisition used a GE 3D LAVA sequence, which is essentially a T1-weighted spoiled gradient sequence with fat suppression. The sequence parameter includes flip angle θ = 10°, TR = 8.73(ms), TE = 2.83(ms), resolution = 0.23x0.23(mm, in plane) x3(mm, axial slice), matrix size = 256x256x12, temporal resolution = 4(s), total acquisition duration = 248(s).

First of all, it is essential to acquire a T1-mapping for the each voxel in the imaging volume. The T1-mapping was done using the multi-angle method described by Parker et al (177). A set of 4 imaging series were performed under intrinsic contrast using exactly the same GE 3D LAVA sequences as the DCE acquisition and same parameters, except for RF flip angles. These series were acquired with 2.5°, 5°, 7.5° and 10° flip angles, respectively. Having the four LAVA datasets, T_1 can be estimated using a simple linear regression. The intrinsic signal S_0 easily follows based on the T_1 estimate.

For all the studies where DCE images were acquired, the Gd injection and acquisition followed the end of the final HP-^{13}C shot, so the HP-^{13}C signal characteristic would not be affected by the presence of Gd.

5.4.3 Results
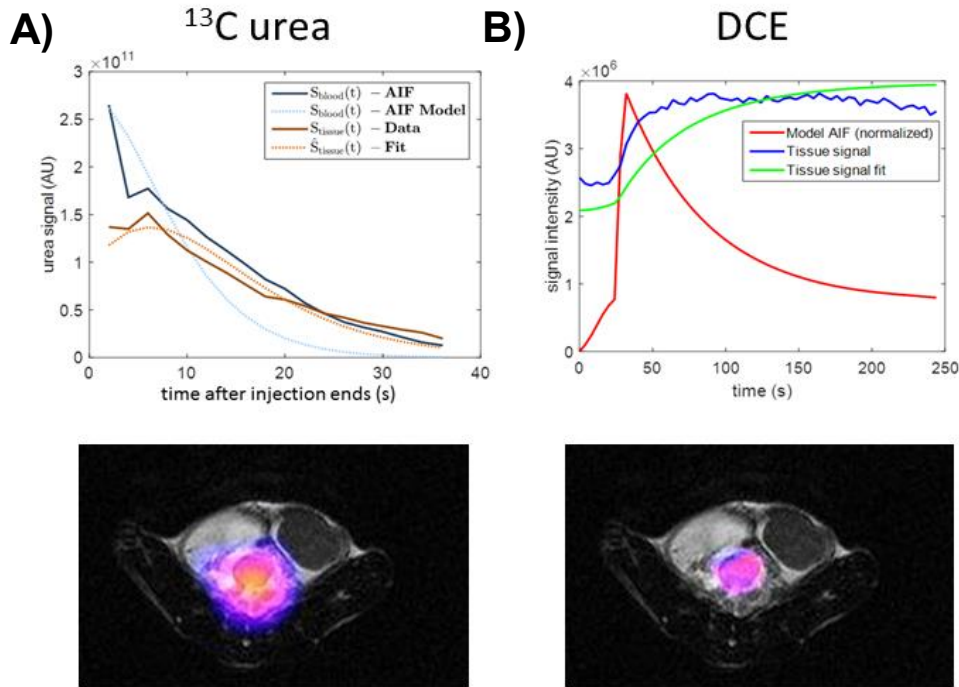
Figure 5.8 *Model fit and maps of k_{trans} estimates from **A)** HP-^{13}C urea and **B)** DCE imaging on a pathologically low-grade TRAMP mice with $k_{PL} = 0.0155$ (s^{-1}).*

DCE imaging was performed post-HP-^{13}C on 4 TRAMP mice. 3 TRAMPs were histologically categorized as low-grade, whereas 1 TRAMP had high-grade tumor. Figure 5.8 shows an example of dynamic curve and fit from HP-urea and DCE on the same animal. While the DCE arterial input function may suffer from fitting ambiguity, both data curves give reasonable fit. Figure 5.9 summarizes the pyruvate-to-lactate conversion k_{PL} and perfusion k_{trans} in the subject mouse prostate tumor. Estimated urea k_{trans} from the co-polarized HP-^{13}C pyruvate+urea MRSI data was $k_{trans,urea}$ = (high-grade:413 and low-grade:245±184 ml/dL/min^{-1}). Urea k_{trans} from the DCE imaging data was $k_{trans,DCE}$ = (high-grade:882 and low-grade:428±125 ml/dL/min^{-1}). k_{PL} was also estimated from the co-polarized injection, giving k_{PL} =

(high-grade:0.0482 and low-grade:0.0172±0.0056 s^{-1}). The k_{PL} and k_{trans} values for

these 4 animals are also reported in Chapter 3, and no overlap in k_{PL} was found

between high- and low-grade tumors. Higher k_{trans} was found in high-grade tumor

using both urea and Gd contrast. There was overlap between high- and low- grade

tumor in $k_{trans,urea}$ values, but not in $k_{trans,DCE}$. Significance was not reported here due

to the small sample size.

5.4.4 Comparison between urea perfusion/distribution volume and DCE
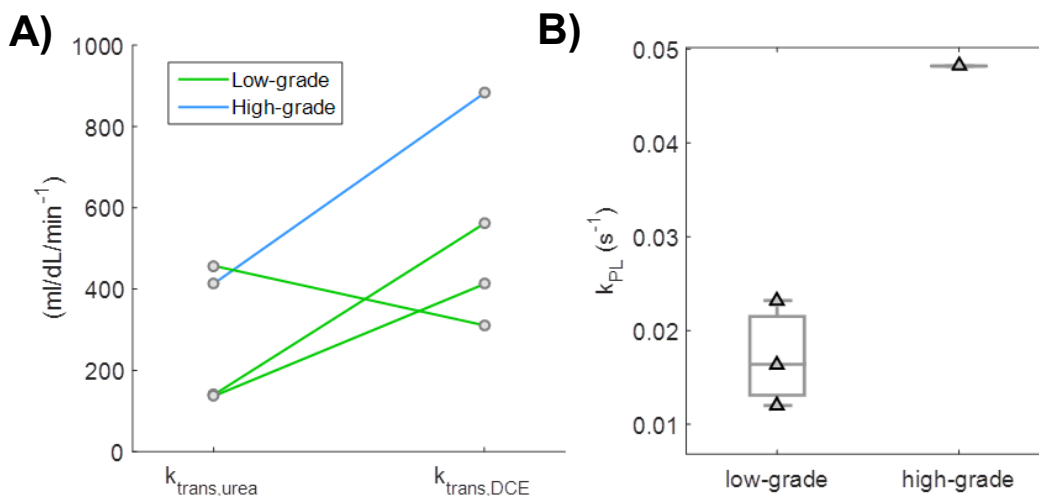
Figure 5.9 A) *k_{trans} estimates from HP-^{13}C urea and DCE imaging 4 TRAMP mice (1 high-grade, 3 low-grade). $k_{trans,DCE}$ was higher for in 3 animals, while $k_{trans,urea}$ was higher in 1.* ***B)*** *The k_{PL} for the 4 TRAMPs involved in this study was excerpted here, showing no overlap in k_{PL} between high- and low-grade tumor.*

In the context of tumor microenvironment, k_{trans} is a combined measure of

perfusion and permeability. The HP-^{13}C urea and Gd-tracer are similar in a sense

that they are both extracellular agent, neither crosses the blood brain barrier, and

both are relatively chemically inert *in vivo*. One difference is the diffusivity, which is

related to the properties of tracer molecule, such as molecule size, uptake by

tissue/organs, and its affinity to other biomolecules. For instance, urea is rapidly transported into red blood cells and kidney medulla (41).

The higher DCE k_{trans} in high-grade tumor can be interpreted as the increased vascular permeability in high-grade tumor, which is correlated to the high expression of *Vegf* in these advanced tumors. It is consistent with prior DCE data of human prostate cancer, where high-grade tumor showed higher and faster signal enhancement, reflected by a high k_{trans} (93). The urea k_{trans} was higher in high-grade tumor as well, where similar explanation applies. The urea molecules should have a slightly higher diffusivity than the Gd macromolecule complex. Interestingly, higher DCE k_{trans} was found than urea k_{trans} in 3 out of 4 cases. This could possibly be attributed to the instability in the model fit, due to either limited available information about urea AIF, the nonlinearity in the DCE AIF estimation, or to the small sample size.

Combination of HP urea and DCE imaging reveal very interesting behavior of tumor perfusion and permeability, as well as the *in vivo* tracer dynamics. In the work of von Morze et al. (41), several other perfusion tracers were investigated. The HP-^{13}C HMCP is more permeable than urea, while the HP-^{13}C t-butanol can be considered freely diffusible. Including these tracers in the future can potentially add valuable information, particularly to understanding of poorly-perfused and hypoxic regions in prostate tumors.

DCE imaging using Gd contrast is a standard protocol in prostate and brain imaging at UCSF, and can potentially be applied to other targets as well. While currently the clinical translation of HP-^{13}C urea is still a work in progress, it would

122

be very exciting to acquire urea perfusion data in patients. As the DCE data is readily available in the imaging protocol, the addition of HP-urea information will open up opportunities toward improved quantitative measurement of tumor perfusion and permeability. Also, with the knowledge that hypoxia is strongly correlated to highly aggressive tumor and poor prognosis (37,38), the ability of urea to detect hypoxia in TRAMP tumor is also very valuable in terms of clinical translation.

5.5 B1-insensitive Variable Flip Angle Design

5.5.1 Introduction and Purpose

As is discussed in this chapter, the capability to quantitatively estimate pyruvate metabolism and urea perfusion using HP-^{13}C MRI is of great importance. Especially in the clinical management of cancer, HP-^{13}C MRI has high potential to become the solution to the demand of non-invasively evaluate tumor aggressiveness and monitor treatment response. The 3D compressed-sensing echo-planar spectroscopic imaging (CS-EPSI) sequence enables 5-dimensional (3-spatial, 1-temporal, 1 spectral) dynamic HP-^{13}C imaging of human prostate cancer with high spatiotemporal resolution. The 3D CS-EPSI sequence can be used to collect high-quality HP-^{13}C data on human brain and prostate cancers.

The variable flip angle scheme was applied to improve metabolite SNR. In particular, it was designed to maximize total lactate SNR while maintaining constant pyruvate signal, which provides basis for reliable quantitative estimation of k_{PL}. Nevertheless, the quantitative accuracy of pyruvate-to-lactate conversion can potentially be affected by B_1^+ inhomogeneity (ΔB_1^+) with this scheme. Calibration of

B_1^+ is challenging due to the limited natural abundance of ^{13}C *in vivo*, and can also

vary across larger imaging volumes. The B_1^+ inhomogeneity can be particularly

serious in imaging targets such as brain and abdomen, where the ROI consists of a

larger volume, and the RF excitation coil geometry can easily lead to a ~20-30%

difference in B_1^+. Therefore, we seek to mitigate the impact of ΔB_1^+ on quantification

from a standpoint of sequence design.
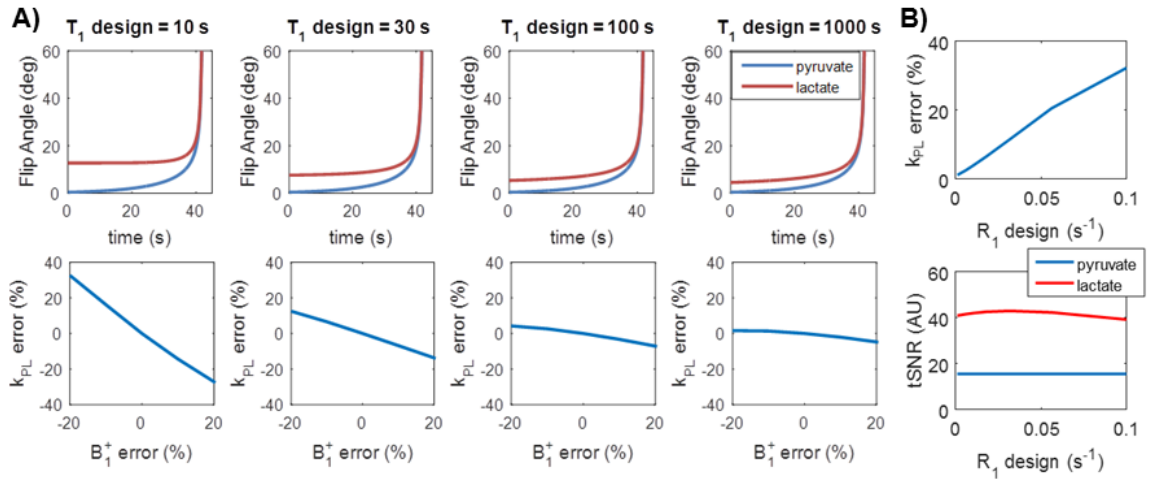
Lactate maximum SNR flip angle equation (Nagashima, 2008)

$$\theta_n = \cos^{-1}\sqrt{\frac{E_1^2 - E_1^{2(n_{max}-n+1)}}{1 - E_1^{2(n_{max}-n+1)}}} \quad \text{where } E_1 = \cos^{-1}\left(TR/T_{1,design}\right)$$

Figure 5.10 *One way of adjusting the B_1 sensitivity profile is changing the effective T_1 used to generate the lactate flip angles (T_1 design). **A)** Longer T_1-design reduces the early lactate flip angles, and Δk_{PL} resulting from the range of error ΔB_1^+ was depicted in this simulation. **B)** Unfortunately, deviating from the "optimal" maximum SNR flip angle design parameters comes at the cost of reduced total lactate SNR. This simulation shows the impact on lactate tSNR (A.U.) of different T_1-designs. While the original T_1-design =30(s) generates maximum signal, our choice of T_1-design =100(s) significantly reduces B1-sensitivitiy at the cost of 2.5% lactate tSNR loss. ΔkPL was shown for 20% B_1^+ error.*

In this section, a new variable flip angle scheme was developed to reduce the

sensitivity to ΔB_1^+ variations across the transmit-coil volume. *In vivo* HP-^{13}C studies

and simulations were conducted to explore the sensitivity of quantitative k_{PL} estimation to ΔB_1^+, as well as changes in total [1-^{13}C]pyruvate and [1-^{13}C]lactate SNR.

5.5.2 Methods

Sequences:

The 3D CS-ESPI sequence enables 3D dynamic imaging with high spatiotemporal resolution[1]. Spectral-spatial excitation pulses for varying flip angles between metabolites were designed using an open-source SS-RF toolbox (55).

The variable flip angle scheme was designed such that the lactate total SNR over time is maximized, and the pyruvate signal remains constant across the acquisition. The pyruvate flip angles are generated using the following equation (13).

$$\theta_{n-1} = \tan^{-1}(E_1 \sin \theta_n)$$

where $E_1 = \exp(TR*(R_1+k_{PL}))$, k_{PL} is an empirical design parameter based on typical k_{PL} values found on subjects, and n =1-N assuming there are a total of N phase encodes over all time points.

The lactate flip angles are described by Nagashima (178).

$$\theta_n = \cos^{-1}\left(\sqrt{\frac{E_1^2 - E_1^{2(N-n+1)}}{1 - E_1^{2(N-n+1)}}}\right)$$

In which $E_1 = \exp(TR*R_1)$.

Additional sequence parameters include TR = 150ms, TE = (6.3ms for original RF pulses, 4.0ms for new RF pulses), spatial resolution: 6.7mm x 6.7mm x

8mm (0.36cm^3, rats), and 8mm x 8mm x 8mm (0.5cm^3, humans), FOV = 8cm x 8cm x

12.8cm (rats), and 9.6x9.6x12.8cm (humans), temporal resolution = 2s, acquisition

window = 42s. The variable flip angles were calculated using MATLAB programs.
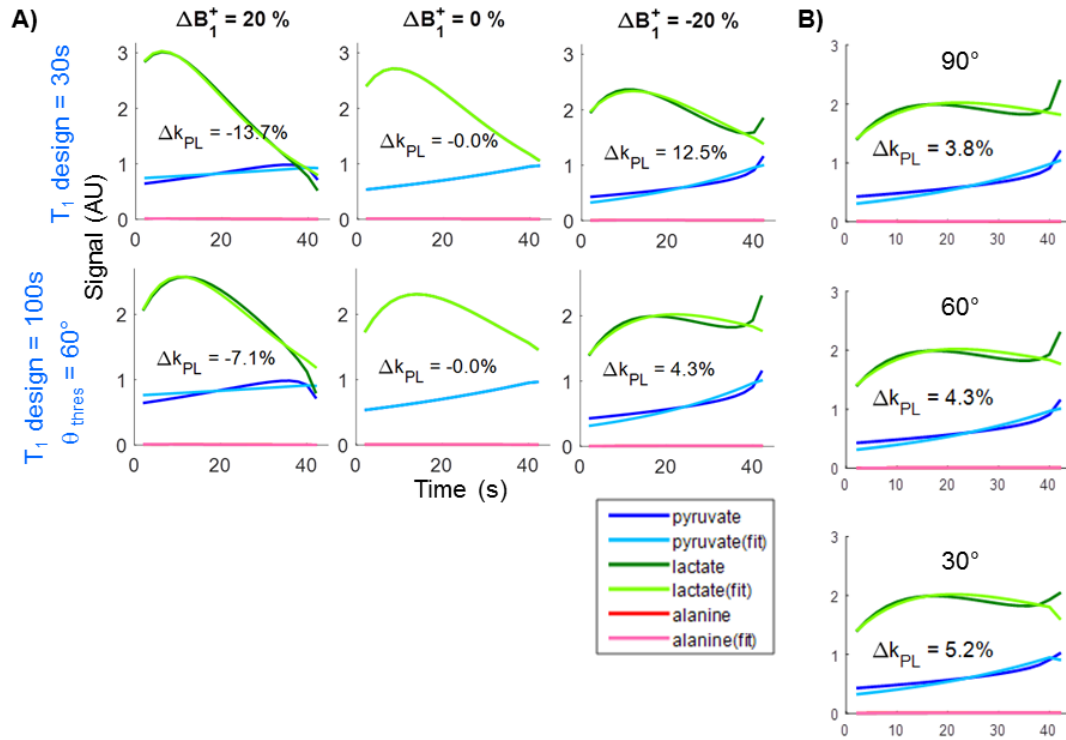
Figure 5.11 *Simulated signal curves and variation of k_{PL} estimates **A)** between our original and the proposed B_1-insensitive flip angle schemes subjected to different ΔB_1^+. The impact of ΔB_1^+ on amplitude of lactate signal is more benign using the new scheme. **B)** A threshold was set to limit the maximum flip angle for improved slice profile. k_{PL} Error was simulated for ΔB_1^+ = -20%. The threshold does not have a significant impact on k_{PL} estimation in terms of ΔB_1^+.*

MRI experiments:

A clamshell volume coil was used for ^{13}C transmit, and a dual-tuned ^{1}H-^{13}C

endorectal coil was applied for receive. Sterile GMP [1-^{13}C]pyruvic acid was

polarized in a 5T SpinLab polarizer for 2-3 hours, yielding 42.8±5.6% polarization of

241±11 mM pyruvate and met all pharmacy specifications prior to injection for the

clinical trial study (N=5) conducted in accordance with the approved IND protocol. The injection was conducted using a power injector (Spectris Solaris, Medrad, Saxonburg, PA) through an i.v. placed at the antecubital vein, with a dose of 0.43ml/kg and injection rate of 5ml/s, followed by 20ml saline flush. T2-FSE images were acquired for anatomical reference and lesion identification with the following parameters, (parameters). The RF power calibration was conducted using a built-in ^{13}C urea phantom embedded inside the endorectal coil.
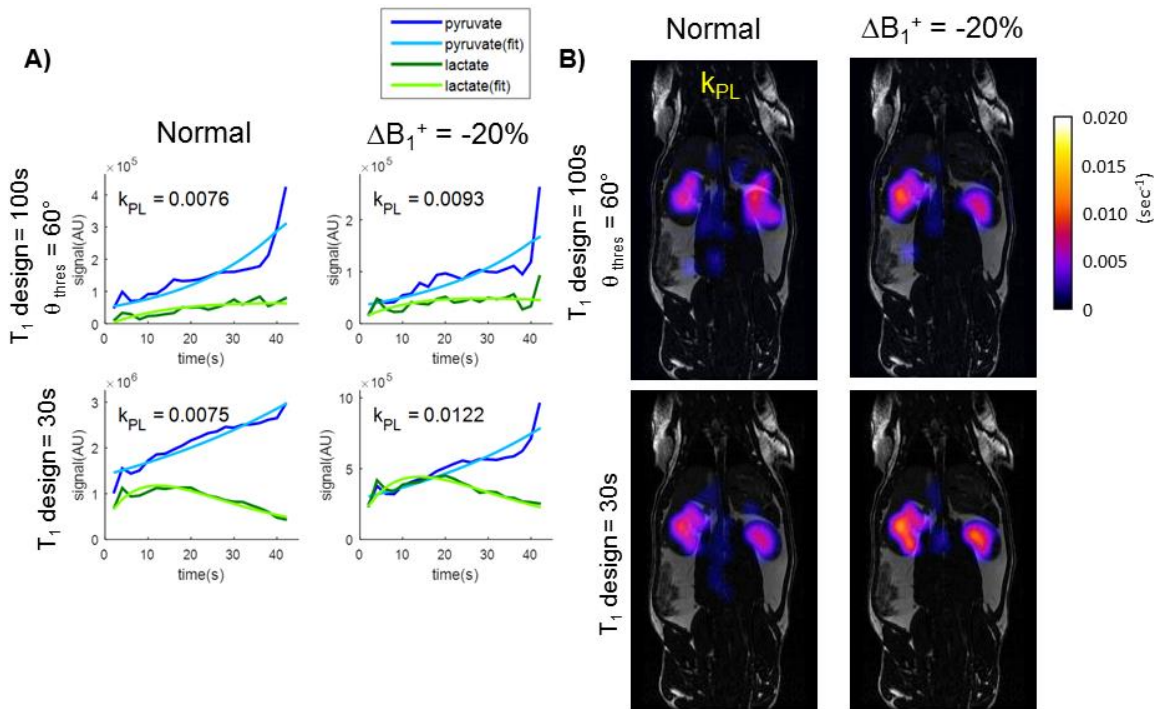
Figure 5.12 *HP-^{13}C imaging of a healthy Sprague Dawley rat using our original and the new B1-insensitive flip angle scheme. The injections were ~15 minutes apart.* ***A)*** *Estimated k$_{PL}$ of rat kidney, which is relatively homeostatic during the course of study. When subjected to variation ΔB_1^+= -20%, the new scheme shows less k$_{PL}$ drift than the original one. (old- Δk_{PL} = 63%, new- Δk_{PL} = 22%).* ***B)*** *Overlaid k$_{PL}$ map on bSSFP anatomical reference for the same data as in* ***A)***.

A healthy Sprague Dawley rat (N=1) was used for animal studies. A customized dual-tuned ^{1}H-^{13}C rat coil is responsible for transmitting and receiving of proton and carbon signals. [1-^{13}C]pyruvic acid was polarized using either Hypersense or Spinlab polarizer, yielding 80mM pyruvate solution with the following buildup time and polarization level - Hypersense: 1-1.5 hours, 20-25%, Spinlab: 2-2.5 hours, 30-35%. A balanced-SSFP ^{1}H scan was used for anatomical references. The injection bolus was 3ml over 12 seconds through a tail vein catheter. The RF power calibration was done using an 8M urea syringe placed right on top of the rat torso.

Simulations and k_{PL} estimation:

HP-^{13}C pyruvate and lactate signals were generated and fit using a simple and robust two-site exchange model, which is described in Section 5.1. B_1 inhomogeneity translates into an effective scaling in a given flip angle scheme, denoted by $\Delta\theta_n$. Potential variations of $\Delta B_1^+ = \pm20\%$ was assumed for clinical environment. All simulations were conducted using MATLAB. For both simulation and *in vivo* data, k_{PL} was estimated using nonlinear least-squares fitting algorithm.

5.5.3 Results/Discussions

One way of desensitizing the sequence to B_1 inhomogeneity is to adjust the effective T_1 design factor ($T_{1,design}$) used to generate the lactate flip angles[5]. At earlier timepoints, higher amount of magnetization is present, and is thus more susceptible to flip angle variation due to ΔB_1^+. Increasing $T_{1,design}$ reduces the flip angle for early

128

timepoints (Figure 5.10), thereby making the design less sensitive to ΔB_1^+. Deviating from the "optimal" design parameters comes at the cost of reduced total lactate SNR. Simulations suggest that while the original $T_{1,design} = 30(s)$ generates maximum signal, a choice of $T_{1,design} = 100(s)$ significantly reduces B_1-sensitivitiy (Figure 5.11A, Δk_{PL} from 12.5% to 4.3% for $\Delta B_1^+ = -20\%$, 13.7% to 7.1% for $\Delta B_1^+ = 20\%$) without substantially reducing SNR (Figure 5.10B, 2.5% lactate tSNR loss).
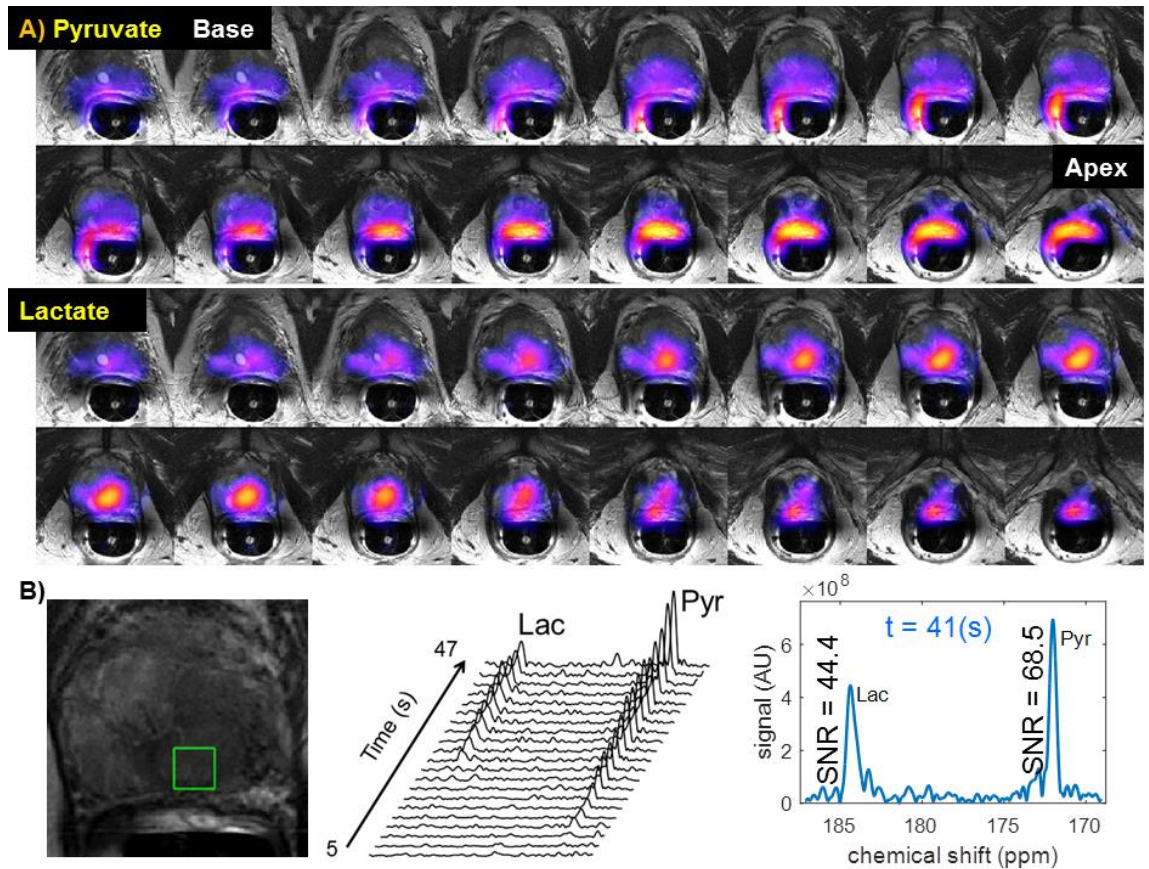
Figure 5.13. The new flip angle design enables acquisition of strong pyruvate and lactate signal in this patient with biopsy-proven Gleason 4+5, 4+4 and 4+3 cancer involving a majority of the left lobe of the prostate and extending into the right peripheral zone. A) 3D dynamic CS-EPSI allows spatial coverage of the entire prostate, from base to apex for HP-¹³C biomarkers (AUC through time). High lactate signal correlates with location of tumor. B) Spectrum through time for a selected voxel in tumor region. Pyruvate signal appears at around 10 s, lactate was observed later at 25 s, consistent with previous findings. At 41s, pyruvate SNR was 68.5, and lactate SNR was 44.4.

An interesting finding is the abrupt bump of signal at the last time point when ΔB_1^+ is negative. This is due to the under-utilization of magnetization in the earlier TRs, leaving more magnetization than theoretically anticipated. The excessive magnetization generates high signal when encountering a high flip-angle excitation pulse. Similar signal bump was also observed in another work (179), where the excessive magnetization there was caused by RF slice profile.
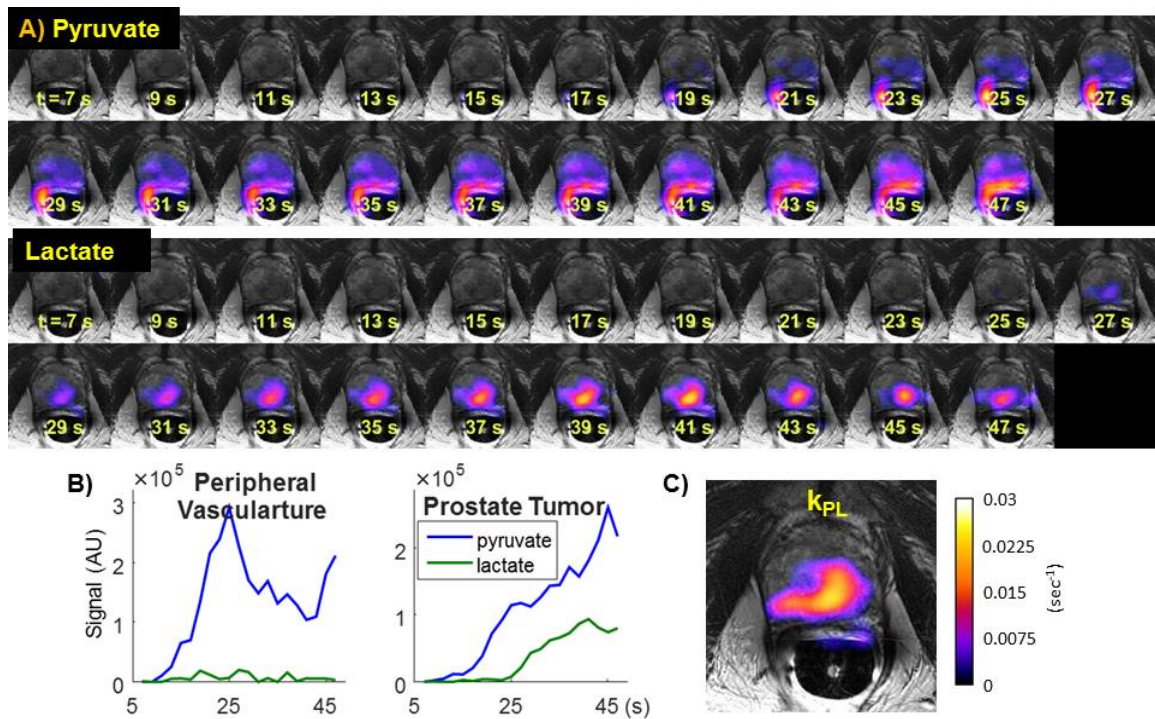
Figure 5.14 A) *Temporal dynamics of HP-^{13}C pyruvate and lactate in a slice that contains prostate cancer. **B)** Signal from clinical prostate tumor and peripheral vasculature. The new sequence not only maintains good pyruvate and lactate SNR, but preserves the timing characteristics of our previous design. Moreover, it potentially enables access to more information by the slightly longer (42s) acquisition window. **C)** Estimated pyruvate to lactate conversion rate k_{PL} map corresponded with a large volume of biopsy-proven Gleason 4+5, 4+4 and 4+3 cancer involving a majority of the left lobe of the prostate and extending into the right peripheral zone.*

Additionally, preventing the final flip angle from increasing to 90° helps to mitigate slice profile artifacts (179). Such thresholding does not have a significant impact on k_{PL} errors in terms of B_1 inhomogeneity, and a 60° threshold was selected based on past simulations[6] (Figure 5.11B). The resulting new spectral-spatial RF pulses using this variable flip angle scheme were 4.0 (ms) long with peak B_1 of 0.492(G), 37% shorter and 17% reduced in peak power than our previous clinical design (Section 4.2). The improved RF pulses may also provide additional benefit beyond ΔB_1^+ sensitivity. The reduced peak power makes the pulses available for different coil setups with limited power output, and the shorter pulse duration may improve SNR by shortening TE.

Four HP-imaging studies were done on a rat during the same session. Two of each using the previous ($T_{1,design} = 30(s)$) or the new (($T_{1,design} = 100(s)$, $\theta_{max} = 60°$)) flip angle scheme. Between the 2 studies using the same flip angle scheme, one is done using the calibrated "nominal" RF power, the other has -20% RF power prescribed on purpose to simulate the B_1^+ inhomogeneity in larger coils. Each of the 4 injections/HP-studies is ~15 minutes apart from one another. Kidneys were selected as our ROI since renal metabolism is known to be relatively homeostatic during the course of study. Moreover, consistently high SNR was observed in kidneys, providing robust k_{PL} estimates.

As anticipated, the new B1-insensitive flip angle scheme generates a different signal time course, with a gradually increasing lactate over time compared to the previous scheme, which has a Gamma-like lactate dynamics. This was probably due to the reduced lactate flip angles at early time points in the new scheme. Very

131

interestingly, the k_{PL} measured using both the original and the new scheme are very similar using the nominal RF power ($k_{PL,new}$ = 0.0076, $k_{PL,old}$ = 0.0075). This suggests that where the ROI is small, has relatively homogeneous B_1 and careful power calibration, both RF flip schedules provide good quantitative power. On the side note, these k_{PL} estimates are also consistent with our previous findings.

The differences became apparent in the presence of Δpower = -20% in order to simulate ΔB_1^+. HP-^{13}C imaging of rat kidney measured substantially lower Δk_{PL} using the new flip angle scheme compared to the previous scheme (Figure 5.12, $\Delta k_{PL,new}$ = 22% vs $\Delta k_{PL,old}$ = 63% with ΔB_1^+= -20%). The *in vivo* data agrees well with simulations, suggesting that the new flip angle scheme reduced B1 sensitivity, and thereby improving reliability of k_{PL} estimates.

For human studies, the dynamic 3D CS-EPSI acquisition with the improved variable flip angle scheme enabled coverage of the entire prostate gland with good spatiotemporal resolution and high SNR (Figure 5.13A & Figure 5.14A) with spectroscopic information (Figure 5.13B). SNR was 68.5 for pyruvate and 44.4 for lactate 41 seconds from injection. The new variable flip angle scheme not only retained excellent pyruvate and lactate SNR, but also preserved the signal timing characteristics compared to our prior studies[1]. The location of high k_{PL} (Figure 5.14C) corresponded with a large volume of biopsy-proven Gleason 4+5, 4+4 and 4+3 cancer involving a majority of the left lobe of the prostate and extending into the right peripheral zone. Mean k_{PL} over the tumor region was 0.0208 for this patient.

5.5.4 Conclusions

The 3D CS-EPSI sequence with an improved variable flip angle scheme
enabled quantitative analysis of pyruvate-to-lactate conversion with far less
sensitivity to B_1^+ variations. Moreover, the human research studies demonstrated
the potential to acquire new information in patient exams while preserving the
desirable SNR efficiency of the previous design. Improved ΔB_1^+ insensitivity is
beneficial for all HP-^{13}C applications, where calibration of this field is challenging
due to the limited natural abundance of ^{13}C *in vivo*. Furthermore, the proposed
variable flip angle schemes will be particularly valuable for human studies over
large volumes, e.g. brain and liver, where substantial ΔB_1^+ will likely be present
across the FOV.

5.6 Practical Considerations of Quantitative k_{PL} Estimation in Hyperpolarized ^{13}C Imaging in Response to Pulse Sequence Design and Parameters

5.6.1 Introduction and Purpose

Hyperpolarized ^{13}C MRSI has enabled imaging of cancer pathophysiology
with high spatiotemporal resolution in both human and translational settings[1].
Pyruvate-to-lactate conversion rate (k_{PL}) is a quantitative measure of cancer
metabolism and LDH activity. For quantitative analysis, it is important to identify
systematic factors introduced by the MR acquisition. We investigated the impact of
sequence design and parameters on estimation of k_{PL} through imaging studies of

transgenic mice with prostate cancer (TRAMP) using a 3D dynamic compressed-sensing ^{13}C-EPSI (CS-EPSI) sequence recently applied for human imaging (180) and simulations.

5.6.2 Methods
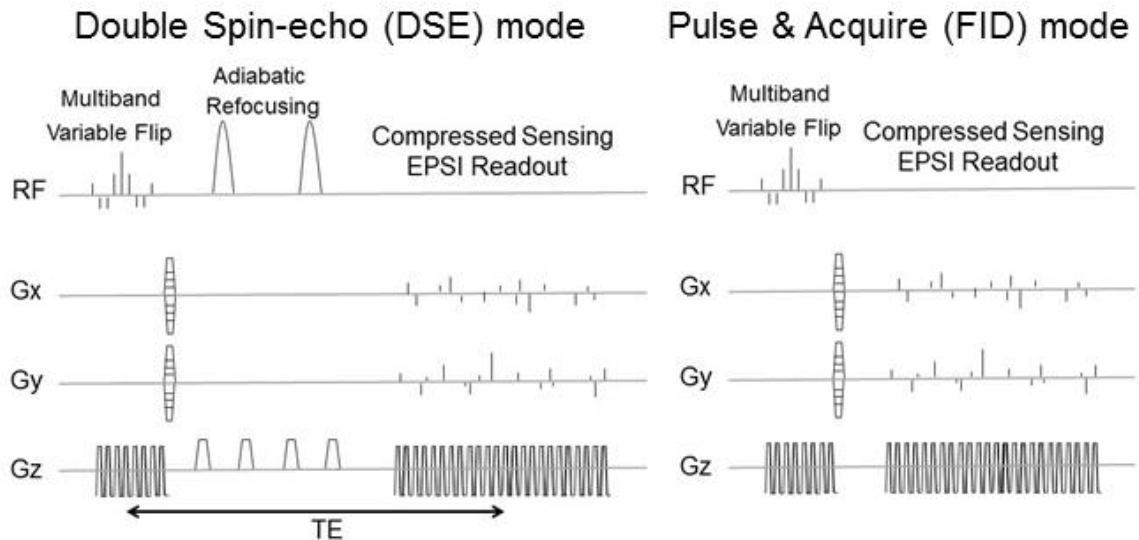
Figure 5.15 *The double-spin echo (DSE) and FID mode of 3D dynamic compressed sensing EPSI sequence, as well as two modified version of FID mode, are used to investigate impact of the sequence design and parameter on quantitative k_{PL} estimation. For ongoing clinical studies, the DSE pulses are disabled due to considerations of peak RF power and B_1 inhomogeneity with patient setup.*

Sequences: A 3D dynamic CS-EPSI sequence provides 5-dimension (3 spatial, 1 temporal, 1 spectral) acquisition with high spatiotemporal resolution. Double spin-echo[2] (DSE, TE=150ms) and FID (TE=6.3ms) acquisition modes (Figure 5.15A), as well as 2 modified sequence schemes (Figure 5.17A &Figure 5.18A) based on the FID mode were applied in HP-^{13}C scans of TRAMP mice.

MRI experiments: Twelve TRAMP mice were studied using a clinical 3T scanner with a dual-tuned mouse coil for ^{13}C and proton imaging. [1-^{13}C]pyruvate was

polarized using a preclinical HyperSense polarizer for 1.5 hours, reaching

approximately 20-25% percentage polarization. Following dissolution, ~350ul of

80mM [1-^{13}C] pyruvate was rapidly injected through a tail vein catheter over 15

seconds. Each ^{13}C MR acquisition began at the end of injection.
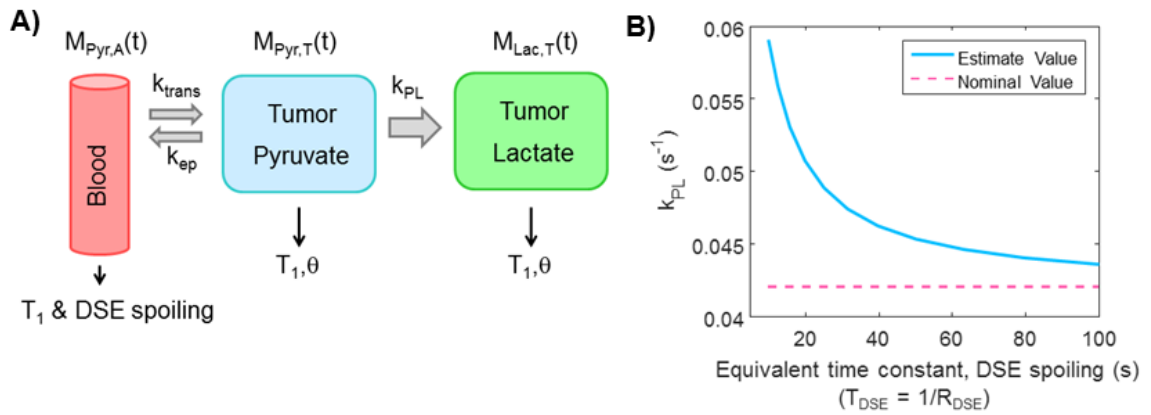
Figure 5.16 A) *A three-site exchange model that introduces pyruvate vascular input was applied for the simulation of DSE spoiling effects. Spoiling was modelled as magnetization loss in the input function $M_{pyr,A}(t)$ with equivalent decay factor R_{DSE}.* **B)** *With stronger DSE spoiling (i.e. shorter time constant), the pyruvate signal decays more rapidly than expected, resulting in higher k_{PL}.*

Simulations: A three-site compartmental model was applied to generate the

simulated DSE-spoiled signal (Figure 5.16A). It consists of a vascular input (AIF) of

pyruvate, as well as tumor pyruvate and lactate compartments (112,140,142,180).

The DSE spoiling was modeled as magnetization loss in the input function $M_{pyr,A}(t)$

with equivalent spoiling rate R_{DSE}. Metabolic conversion and signal loss

mechanisms, such as RF excitations and T_1 relaxation, were also included in the

model. The k_{PL} fit was estimated using the robust two-site exchange model also

applied *in vivo* (110,180). All simulations were performed on MATLAB.

5.6.3 Results and Discussions
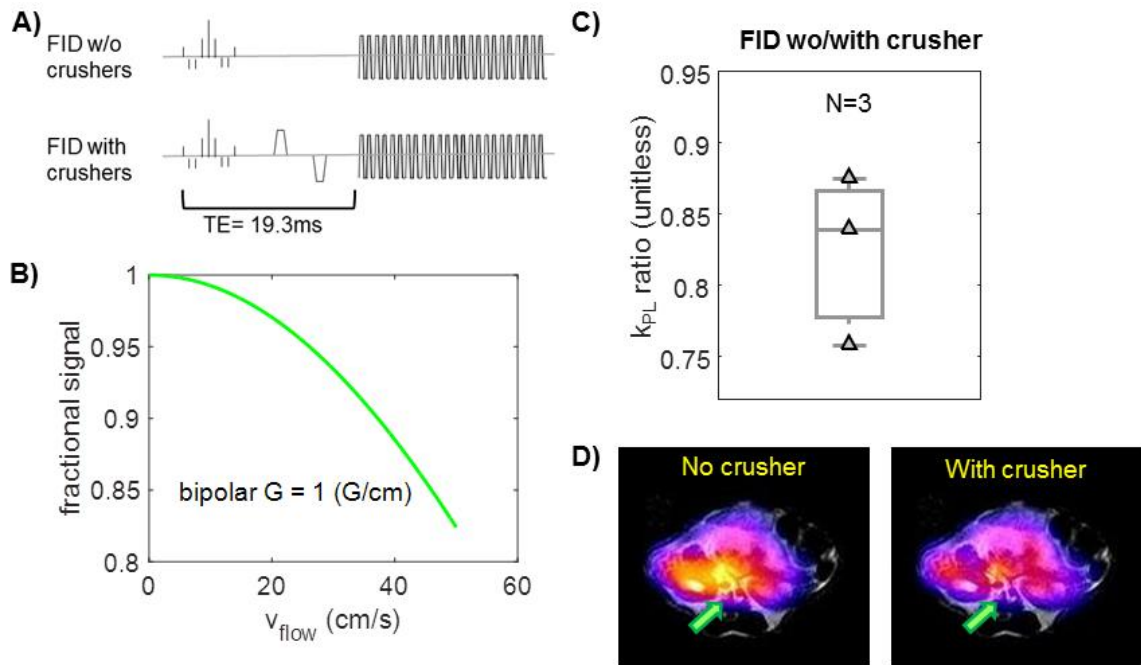
Figure 5.17 *Simulated and experimental results testing the impact of crusher gradients (applied around DSE refocusing pulses) to suppress flowing spins, which are predominately pyruvate. **A)** A pulse sequence with and without crusher gradients was tested. **B)** Fraction of signal remaining with the given crusher gradient strength in **A)**. **C)** Lower tumor k_{PL} estimates were observed using the "no crusher" sequence, as anticipated. **D)** Map of pyruvate area under curve. Spatially-dependent flow-suppression can be observed around the major vasculature.*

One difference between DSE and FID mode, first observed by Josan (157), is that the two adiabatic refocusing pulses may spoil the HP-^{13}C spins near the coil edge, which predominantly affects the AIF of pyruvate. In simulations, RF spoiling on AIF was modeled as an equivalent spoiling factor R_{DSE}. Increasing R_{DSE} results in higher k_{PL} estimates (**Fig.2B**) since the tumor pyruvate pool, directly supplied by AIF, decayed more rapidly than expected by the kinetic model.

Secondly, the crusher gradients (G=1G/cm on x,y,z, δ = 2ms, Δ = 11.8ms, Venc = 0.21m/s, b = 0.02s/mm^2) around the DSE refocusing pulses can act as flow-

suppressing gradients, reducing vascular pyruvate signal and leading to a higher k_{PL} estimate (181), similarly to the DSE spoiling. Simulations yielded a ~10% loss for typical peak arterial blood velocity of 30(cm/s) in animals. Back-to-back HP-^{13}C studies of TRAMP mice on the same day using FID mode scans with and without the crusher gradients demonstrated higher prostate tumor k_{PL} estimates with the crusher (Figure 5.17C, $k_{PL,crusher}/k_{PL,w/o}$ = 1.22±0.09, n = 3), corroborating the simulation results. Moreover, flow-suppression effects were preferentially seen near the major vasculature and renal arteries (Figure 5.17D).
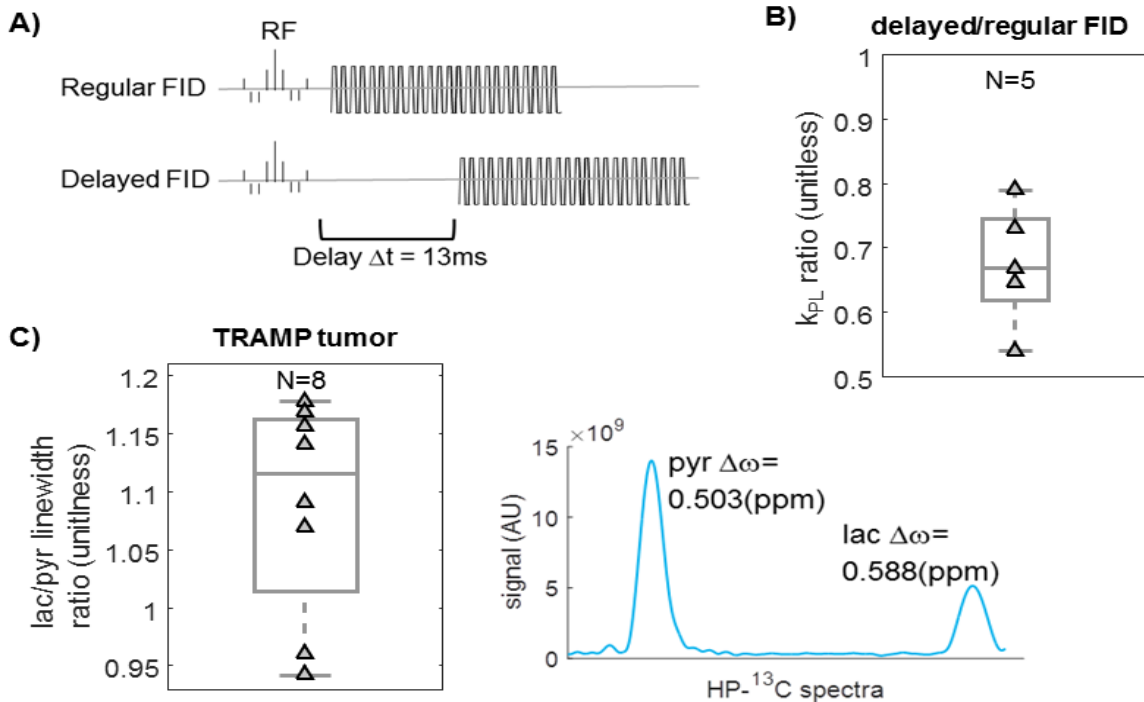
Figure 5.18 *It is hypothesized that lactate has shorter T_2^* than pyruvate.* **A)** *If lactate has shorter T_2^*, a "delayed" (Δt = ~13ms) FID sequence will give lower k_{PL} compared to regular one.* **B)** *Ratio of k_{PL} estimate in the same TRAMP tumor using delayed versus regular FID sequences. The delayed sequence gives lower k_{PL}.* **C)** *Furthermore, the in vivo lactate linewidth was broader than pyruvate, and thus lactate had a shorter T_2^*.*

Finally, *in vivo* T_2^* is hypothesized to be much shorter for lactate than pyruvate due to J-coupling (182,183). A "delayed" FID mode purposely introduced a longer echo time (Δt_{delay}=13ms) to introduce more T_2^* decay. As anticipated, lower tumor k_{PL} was found using the delayed sequence vs. normal FID (Figure 5.18B, $k_{PL,delay}/k_{PL,FID}$ = 0.67±0.09, n = 5), in back-to-back TRAMP tumor injections. Additionally, the lactate peak had broader linewidth than pyruvate in TRAMP tumor studies (Figure 5.18C), in agreement with the linewidth differences Marjańska (182) and Chen (184) observed due to lactate J-coupling that results in T_2^* weighting.

When comparing DSE and FID modes, a higher tumor k_{PL} was observed using the DSE than FID mode (Figure 5.19A, $k_{PL,FID}/k_{PL,DSE}$ = 0.48±0.20, N=7). This likely is a result of the DSE spoiling and crusher flow-suppression in the DSE sequence increasing the tumor pyruvate decay rate (Figure 5.16 & Figure 5.17) and FID T_2^* weighting (Figure 5.18). It may also be a result of compartmental T_2-weighting at the DSE TE=150ms, as pyruvate was measured to have a larger short-T_2 component compared to lactate in TRAMP tumors (183), which would further reduce the pyruvate signal in the DSE.

A) FID/DSE

B)

Compared Values	Ratio (unitless)
k_{PL} of regular FID/ k_{PL} of DSE	0.48±0.20
k_{PL} of delayed FID/ k_{PL} of regular FID	0.67±0.09
k_{PL} w/o crusher FID/ k_{PL} of crusher FID	0.82±0.06
Spectral linewidth $\Delta\omega_{lac}/\Delta\omega_{pyr}$	1.08±0.09
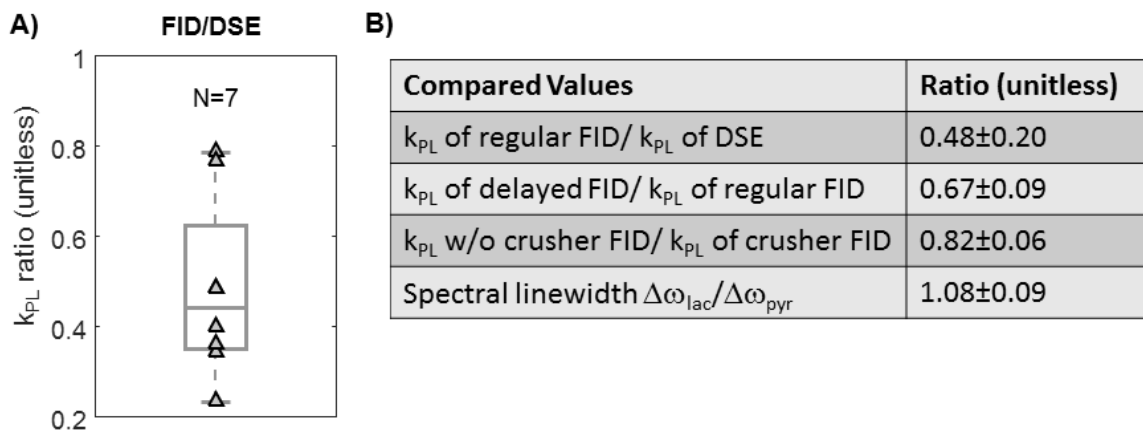
Figure 5.19 A) *Lower tumor k_{PL} estimates were found using FID versus DSE sequences. For each pair of data, the hyperpolarized study was conducted on the same day using the same transgenic mouse with prostate cancer (TRAMP).* ***B)*** *This table briefly summarizes all the in vivo comparisons made in TRAMP prostate tumors between the different sequences, including k_{PL} and linewidth, in order to investigate three major factors that affect k_{PL} estimation.*

5.6.4 Conclusions

We have identified 3 systematic sources that can affect the quantitative k_{PL} estimation using 3D dynamic EPSI sequence. These sources are particularly important in the context of clinical translation of HP-^{13}C imaging, where use of spin-echoes is more challenging due to peak RF power and B_1 homogeneity considerations. It is worth mentioning that while this study provides simulated and experimental estimates of these factors, the actual impact largely depends on the pathophysiology and pharmacokinetic behavior *in vivo*.

Chapter 6 Extension, Current and Future Work

6.1 New sampling patterns for 3D CS-EPSI sequence

6.1.1 The need for new sampling patterns

Transition from animal to clinical research requires substantial technical advancements including hardware, such as ^{13}C coils, MR pulse sequences, imaging reconstruction and processing software. On the pulse sequence end, design of new sampling patterns is both scientifically interesting and valuable to meet the emerging needs in imaging patients. Therefore, new designs of undersampling patterns for the 3D CS-EPSI sequence were developed to account for the new features and to address new requirements in clinical studies.

For example, in brain imaging the 2D EPSI sequence has been found to reproducibly generate good-quality spectroscopic images in tumor as well and contralateral normal brain. Using acquisition parameters (TE/TR = 6.1/130ms, in-plane resolution = 20x20mm, slice thickness = 20-30mm, matrix size = 10x18, temporal resolution = 3s , FOV= 20 x 36 cm, acquisition window = 24, flip angle = single-band 10°), peak SNR of 320 for pyruvate and 180 for lactate was observed (185). Bicarbonate was also detected. Compared to our prostate acquisition protocol, the brain acquisition has a much larger FOV to cover the entire tumor-containing slice, with coarser spatial resolution (brain:20mm vs prostate:8mm). Nevertheless, the physical coverage of the clamshell transmit and the 8-CH phased array receiver (~10cm) is larger than the 2D slice thickness (2-3cm) in the SI direction, and there is room to acquire 3-dimensionally (Figure 6.1).

3D imaging not only enables imaging of normal brain regions, potentially covers lesion with larger areas, but also eased the burden of FOV prescription. The selection of FOV, which includes choice of slice thickness, and placing the slice right on top of the tumor region, can be challenging and often user-dependent. This is because frequently the coarse T_2-weighted reference scans, acquired before the ^{13}C injection, do not reflect lesions very well, and the user has to rely on the resampled T_2-FLAIR images from previous scans in patient database to prescribe FOV.

Figure 6.1 *The coil setup of brain imaging study consists of a clamshell transmit and an 8-channel phased array receiver. (Figure from brain imaging manual.)*

Transition from 2D to 3D acquisition means that the user only need to ensure that the FOV covers the entire brain, and determine an appropriate voxel size for sufficient SNR performance. Segmentation of tumor voxel and quantitative analysis can be done in processing using open-sourced SIVIC software and voxel-shifting

technique. Moreover, the 3D acquisition also enables utilization of the originally out-of-slice magnetization not accessed by the 2D slice EPSI acquisition scheme.

6.1.2 Strategy for sampling pattern design

Although the clinical setup, compared with animal study environment, is limited by lower relative lower RF power output and reduced coil sensitivity, there are some favorable aspects that can be exploited for performance. First of all, the transition from the animal DSE sequence with adiabatic refocusing to the FID sequence in human leads to a significant reduction in echo time TE. Moreover, the multi-channel capabilities (e.g. 8CH phased-array) may provide data redundancy to develop parallel imaging reconstruction techniques, as will be explained in the next section.

To accommodate for the length of the flyback EPSI readout and the random blip encode, the echo time for DSE sequence is TE_{DSE} = 250ms. For FID sequence, the echo time can be reduced to TE_{DSE} = 130ms using the shortened RF pulses and the same readout. If keeping the 2-second temporal resolution, the maximum number of phase encodes allowed in one timepoint increases from 8 in DSE to 15 in FID. Assuming we wanted to keep the undersampling ratio approximately the same, the extra phase encodes can be utilized toward a larger matrix size in space. A larger matrix can mean larger FOV with the same spatial resolution, or finer resolution with the same FOV.

Even with the additional TRs, the variable flip angle scheme can be recalculated accordingly such that the total magnetization usage in one timepoint

will remain the same. In this case, the total signal over a given coverage will also stay the same, and the theoretical SNR per voxel is only a function of the voxel size.
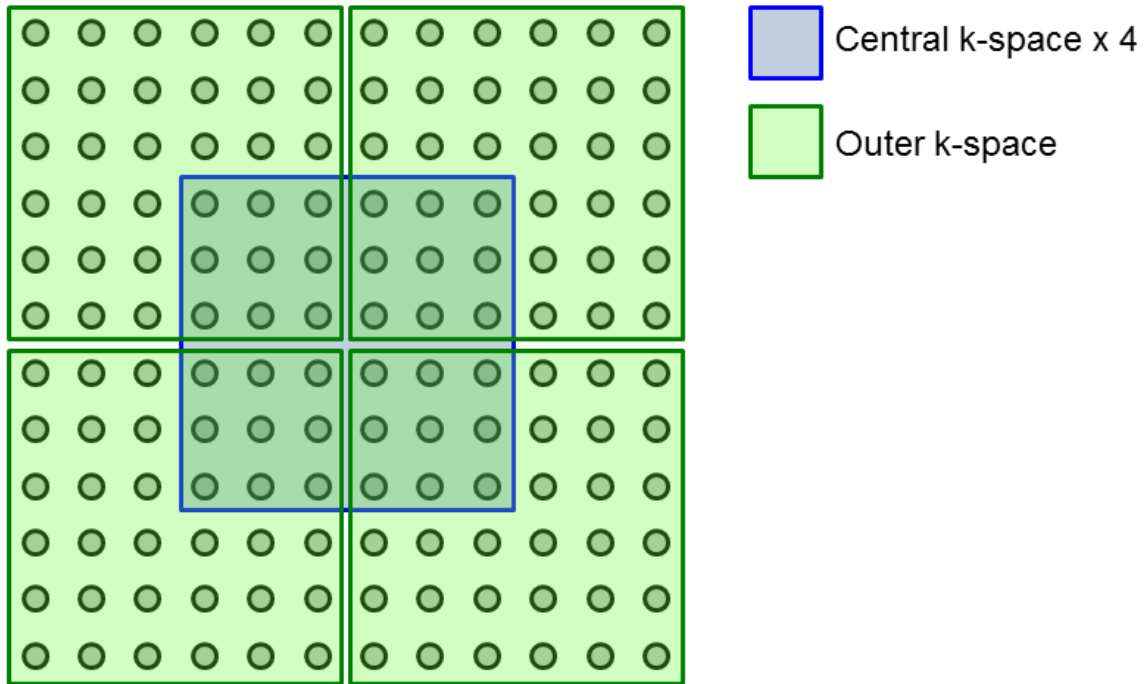
Figure 6.2 *Sampling pattern design for the 12x12 matrix used in TRAMP and human prostate imaging sequences. Each box represents a phase encode (TR). The central k-space box was covered 4 times, and the outer k-space box was covered once for each 8-TR timepoint. Note that the random blip pattern and the order of phase encode was different for each timepoint.*

6.1.3 Examples of new sampling pattern

First we would like to try designing a 16x16 in-plane matrix size. The 16x16 matrix translates to 256 encodes in the k_x-k_y plane. Compared to the original 12x12 matrix used for prostate imaging, which has 144 encodes (Figure 6.2), the number of encodes in the 16x16 matrix is 1.78 times that of 12x12. Now that we have room

for 15 TRs per timepoint rather than the original 8, that allows 1.87 times the number of encodes while retaining the same undersampling density. Therefore, the number of encodes should suffice for a 16x16 undersampling pattern without compromising the undersampling ratio and sampling density.

The original 12x12 undersampling scheme has a variable density sampling pattern, with the central k-space more densely sampled and the outer k-space more sparsely so (11). Out of the 8 TRs, 4 of them cover the central k-space, while the other 4 cover the outer k-space (Figure 6.2). To ensure temporal sparsity, the undersampling pattern in each timepoint is designed differently, and the order of each TR is also randomized across timepoints (12).
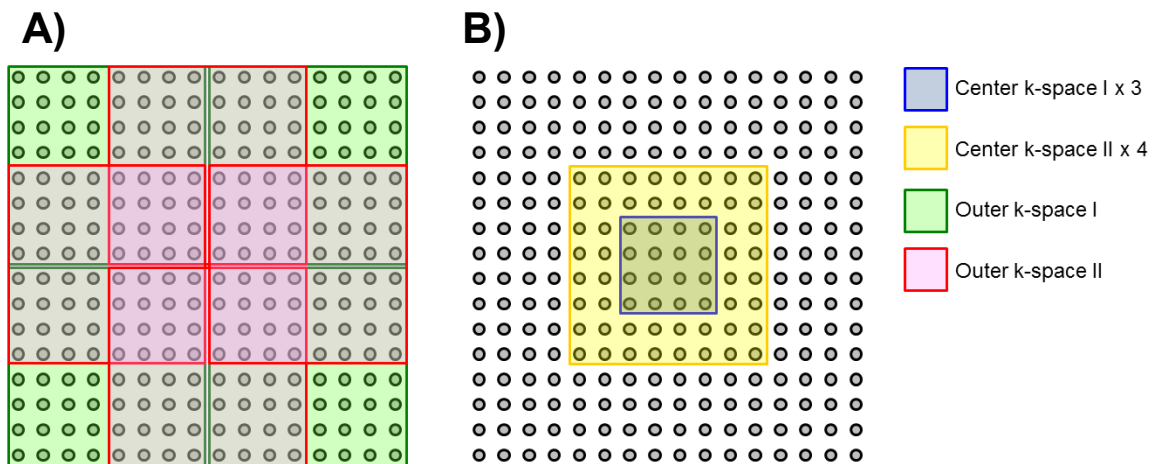
Figure 6.3 *The first sampling pattern design for the 16x16 matrix designed for brain imaging. Each box represents a phase encode (TR). The central k-space box was covered 3(blue) and 4(yellow) times, and the outer k-space box was covered once (green, red) for each 15-TR timepoint. This ensures that the center k-space received higher sampling density just like the prostate case.*

Here 2 new undersampling patterns for 16x16 matrix were presented as examples. In the first sampling pattern (Figure 6.3), the centermost 4x4 matrix (blue) was sampled in 3 TRs, and the center 8x8 matrix (yellow) in 4 TRs. The outer k-space 8x8 matrices (green and red) are each sampled once. Similar to the previous 12x12 scheme, this pattern ensures that the center k-space, where most HP-^{13}C signal is present, receives relatively high sampling density. Therefore, good SNR can be achieved. It also makes sure that the outer part of k-space is at least covered in one of the TRs for compressed-sensing reconstruction.
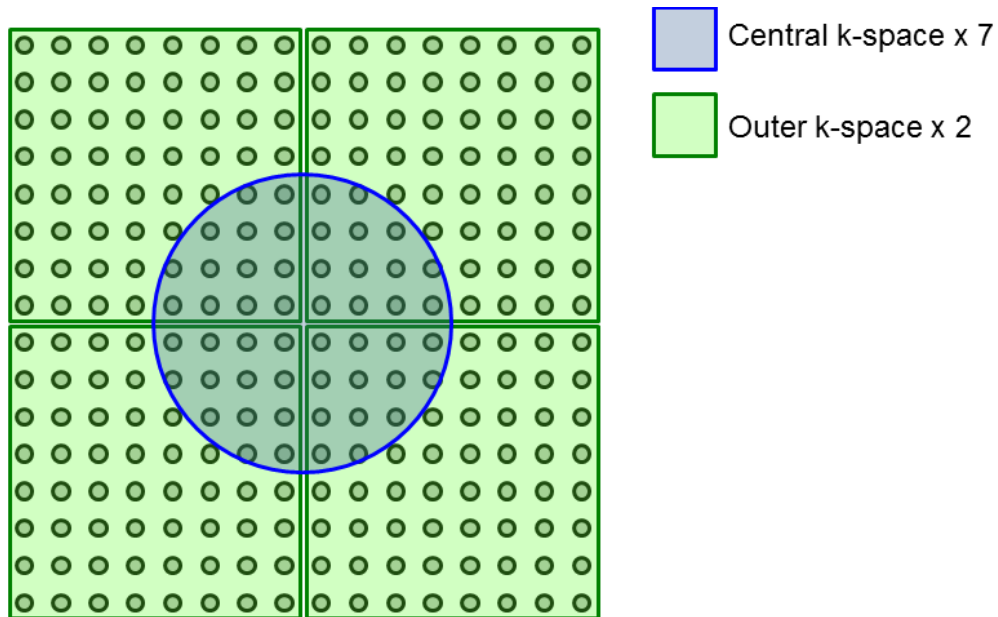
Figure 6.4 *The second sampling pattern design for the brain imaging 16x16 matrix. Each box or circle represents a phase encode (TR). The central k-space box was covered 7(blue) times, and the outer k-space box was covered twice (green) for each 15-TR timepoint.*

Sampling pattern 2 has more straightforward approach (Figure 6.4). The 8x8 outer k-space matrices (green) are each sampled in 2 TRs. The center k-space is

covered with a circle of radius 4.5 units, such that the area covered by the circle is equivalent to that of an 8x8 square. The circular area is repeatedly sampled in 7 TRs.

It is important to note that these new sampling pattern are enabled owing to the larger FOV for clinical scans versus animal, and the improved maximum gradient strength in the new 3T clinical MRI scanner (GE MR750, GE Healthcare, Waukesha WI). From the relation between k-space encode step and gradient strength, we have $\Delta k = (\gamma/2\pi)\cdot$blip area = 1/FOV, and therefore $\Delta k = 0.58$(G/cm) is required for one phase encode step given FOV = 4(cm). For the older 3T scanner, the max gradient strength of 4(G/cm) allows blip distance of 6 steps (i.e. a 7x7 matrix). Assuming same FOV, the max gradient strength of 5(G/cm) is equivalent to 8 steps, enabling a 9x9 matrix size. Therefore, it is safe to sample an 8x8 area in each TR.

With the high gradient strength, the new sampling pattern can achieve finer resolution with the mouse-sized FOV, assuming that the SNR is sufficiently high. In most cases, the head size of a patient is smaller than 24x20 (cm). While a 12x12 matrix provides spatial resolution of 2 (cm) isotropic, the 16x16 matrix can improve the resolution to 1.5(cm) isotropic. Moreover, rectangular matrix with different sizes in x and y, such as a 16x14 matrix, can also be designed, which can further reduce undersampling ratio compared to the original 12x12 or the new 16x16 sampling patterns.

6.1.4 Discussions

The compressed sensing undersampling technique enabled 18x acceleration in the 3D CS-EPSI sequence by random blip encoding in the k_x-k_y direction (11,12).

The new 16x16 sampling pattern was enabled by the increase in number of phase encodes (TRs) per timepoint in the FID acquisition mode and the shortened RF excitation pulses. According to Figure 3 from Larson et al (12), the RMS error that originated from compressed sensing reconstruction with an 18x undersampling is less than the RMS error with peak SNR of 50-60 (RMSE < 0.001). While the typical SNR observed from mouse studies is around 60-80 for both pyruvate and lactate, the SNR from human 3D clinical studies was found to be lower, with on average 45 for pyruvate and less than 10 for lactate. Therefore, the dominant source of variation in patients will be data noise rather than CS reconstruction error. The use of parallel imaging techniques, as will be discussed in Section 6.2 , can potentially further increase the undersampling ratio by utilizing the redundancy across the array element dimension.

The undersampling pattern and matrix design created flexibility in the scan parameters such as spatial resolution and FOV size. The new sampling strategy is particularly beneficial to HP-^{13}C brain imaging studies. They not only relieve the burden of FOV prescription for brain tumor scans, but allow one to go to finer spatial resolution. Moreover, these new sampling patterns can be readily applied to other imaging targets in human.

6.2 SAKE-like reconstruction for multichannel 3D MRSI data

In the beginning of this section, I'd like to acknowledge Dr. Peng Cao for developing the generalized SVD-based reconstruction algorithm, suggesting the idea of parallel imaging reconstruction using 3D CS-EPSI sequence, and generously

provided sample code off which this 3D multichannel reconstruction was implemented. I'd also like to thank Dr. Ilwoo Park for allowing and helping me acquire the world's first HP-^{13}C 3D dynamic human brain data on one of his glioblastoma patients, and for his insightful discussion and knowledge about brain tumor imaging in general. I cannot express my gratitude enough for Drs. Cao and Park's help to make this mini-project happen.

6.2.1 Introduction to SVD-based parallel reconstruction

Parallel imaging is an important sampling and reconstruction technique for multichannel MRI imaging. It utilizes the data redundancy across the coil and the sensitivity profile for accelerated acquisition and improved SNR. Conventional parallel imaging techniques require the *a priori* knowledge of coil sensitivity profile for reconstruction. Besides that, several papers reported auto-calibration reconstruction, where the coil sensitivity is jointly estimated with image data. Shin et al. proposed a calibration-less parallel imaging reconstruction (165). This technique, which they called simultaneous autocalibration and k-space estimation (SAKE) method, transforms the data into a block Hankel matrix form, and solve for a matrix completion problem.

Cao et al. further extended the SAKE method to randomized undersampling in the time (k_f) dimension (70). This enabled reconstruction of high-dimensional CSI dataset which includes spatial, spectral and temporal dimensions. The details of Cao's method can be found in their work, but the key theory and equations are excerpted here

A)

Undersampled k-space

Cao et al., *MRM*, 2016

B)

High Performance "Grid"

slice 1
slice 2
⋮
slice n

singular value thresholding

1st stage processing → 2nd stage processing
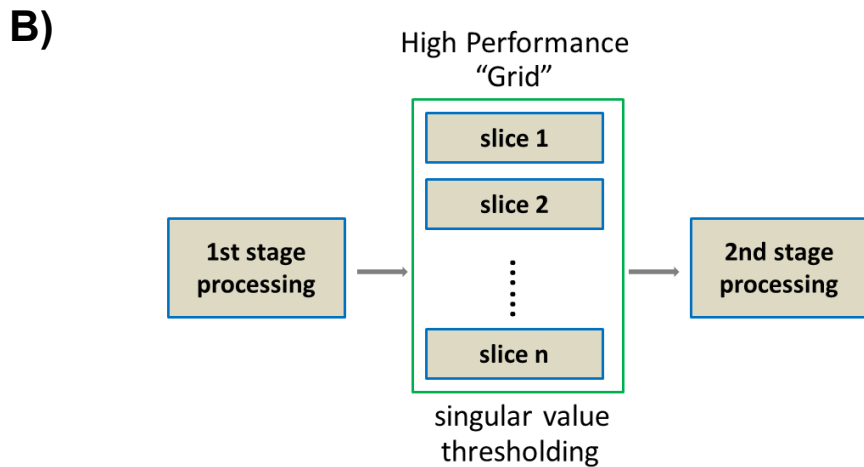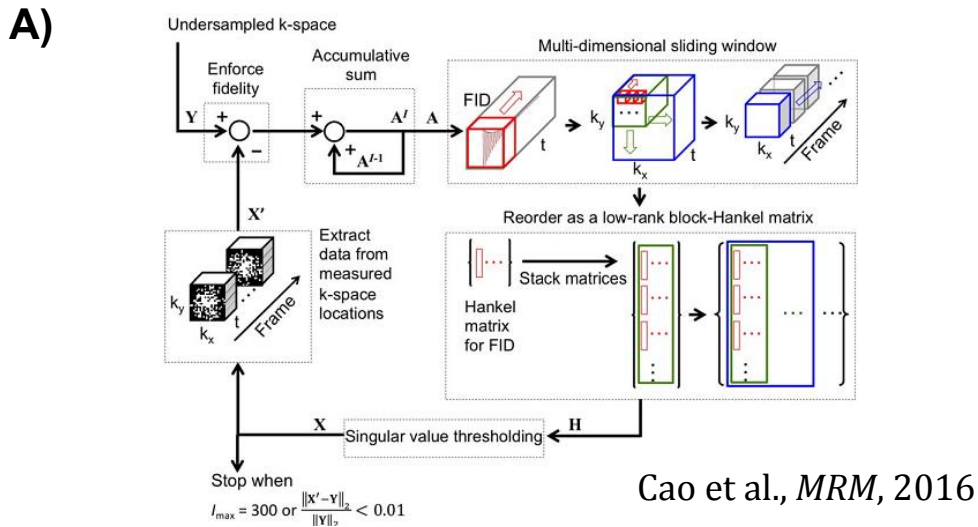
Figure 6.5 A) *The SVD-based reconstruction utilized the singular value thresholding on the Hankel matrix of the undersampled dataset. The reconstruction is achieved by iterative thresholding and enforcing data consistency. (70)* ***B)*** *The UCSF's high performance "Grid" enabled the distribution of reconstruction into paralleled tasks, and therefore improves overall efficiency.*

The k-space signal $s_l(k_x,k_y,k_z,t)$ can be written as a linear combination of spectral-spatial peaks with Lorentzian lineshape. Applying a sliding-window block-Hankel transform on this dataset generates the block-Hankel matrix representation of such dataset.

149

$$H = \sum_{l=1}^{L} H_l$$

Here the block Hankel matrix **H** is represented as a linear combination of

spatial-spectral peaks **H**l, where L is the total number of spatial-spectral peaks in the

k_x-k_y-k_z-k_f space. By matrix properties, rank of matrix **H** is smaller than L.

Reconstructing of the undersampled dataset becomes a matrix completion problem

for its block-Hankel representation, which can be formulated as follows.

$$\arg \min_x \|H(X)\|, \text{ s.t. } M(X) = Y$$

where M is the k-space undersampling operator, H is the block-Hankel transform

operator, **X** and **Y** are the reconstructed and the undersampled datasets,

respectively. The matrix completion can be solved by an iterative singular value

thresholding and data-consistency enforcing algorithm, as described by Cao (70).

6.2.2 Application of SVD-based reconstruction to 3D CS-EPSI

Cao et al. reported that a matrix of size 8x8x512x20 for an undersampled 2D-

CSI dataset was reconstructed using SVD-based algorithm in approximately 50

minutes. An undersampled 3D dataset may need extra computational power and

longer time for reconstruction. The current 3D dynamic sequence for prostate

imaging presents a 5-dimensional dataset (x,y,z,f,time). The matrix size for an 8-

channel data, for instance, will therefore be 12x12x16x59x18x8(coils), or

equivalently about 32 times that of Cao's 2D-CSI dataset.

In order to improve computational power, we utilized UCSF Radiology's High

Performance Computation (HPC), also known as the "Grid." The idea is similar to the

parallel processing toolbox provided by MATLAB. Instead, the Grid is design to divide the reconstruction task to several distributed servers on the network, with each server assigned one or multiple tasks based on the resource allocation. We divide the task along the z (typically SI) direction, on which the 3D CS-EPSI is fully sampled by the EPSI readout. Each task is then automatically assigned to a server on the Radiology network, while one server can receive multiple tasks at the same time if the resources allow.

Using a retrospectively-undersampled dataset with the matrix size of prostate imaging, the total computation time would have been approximately 100 hours (using 150 iterations). First we run the reconstruction on a single workstation using MATLAB's parallel toolbox, and found that the reconstruction takes approximately 3-4 hours, which is shorter than the anticipated time. This could be due to the smaller size in the time (FID) dimension, and the acceleration by parallel toolbox. The reconstruction routine is than transplanted onto the Grid, where it was divided into 16 slices, which may further reduce the total computational time. Interestingly, we found that the reconstruction still takes around 3 hours on the Grid. A careful examination of the process log revealed that while some servers finish the task very efficiently, the overall job has to wait for the slower servers. In the future, it might be beneficial to optimize the reconstruction algorithm for speed, and to improve resource allocation for higher efficiency.

6.2.3 SVD parallel reconstruction versus channel-by-channel L1-minimization

A)

B)
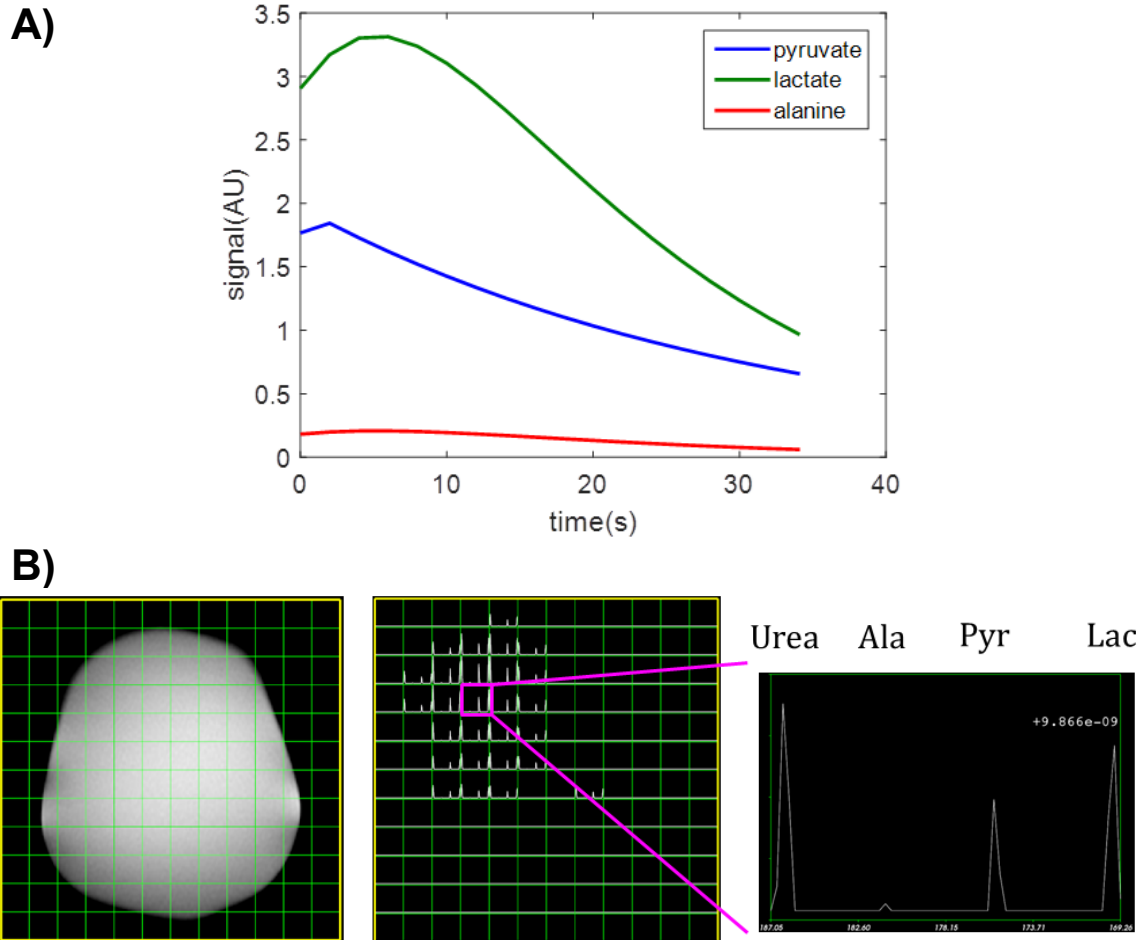
Figure 6.6 A) *A simulation dynamic curve for pyruvate, lactate and alanine was generated using a three-site exchange model with boxcar input function.* ***B)*** *The simulation dynamics was weighted by sensitivity map for each coil element to generate spectra over the head phantom. The Lorentzian linewidth was set to 0.8(ppm).*

To compare the SVD reconstruction to the conventional L1-minimization algorithm, a "simulation" dataset was created from a 3D phantom dataset using an ethylene glycol head phantom, clamshell transmit and 8-channel array receiver. The sensitivity profile was extracted from the head phantom dataset. The "dynamic" curve of pyruvate metabolism was generated by simulation using a two-
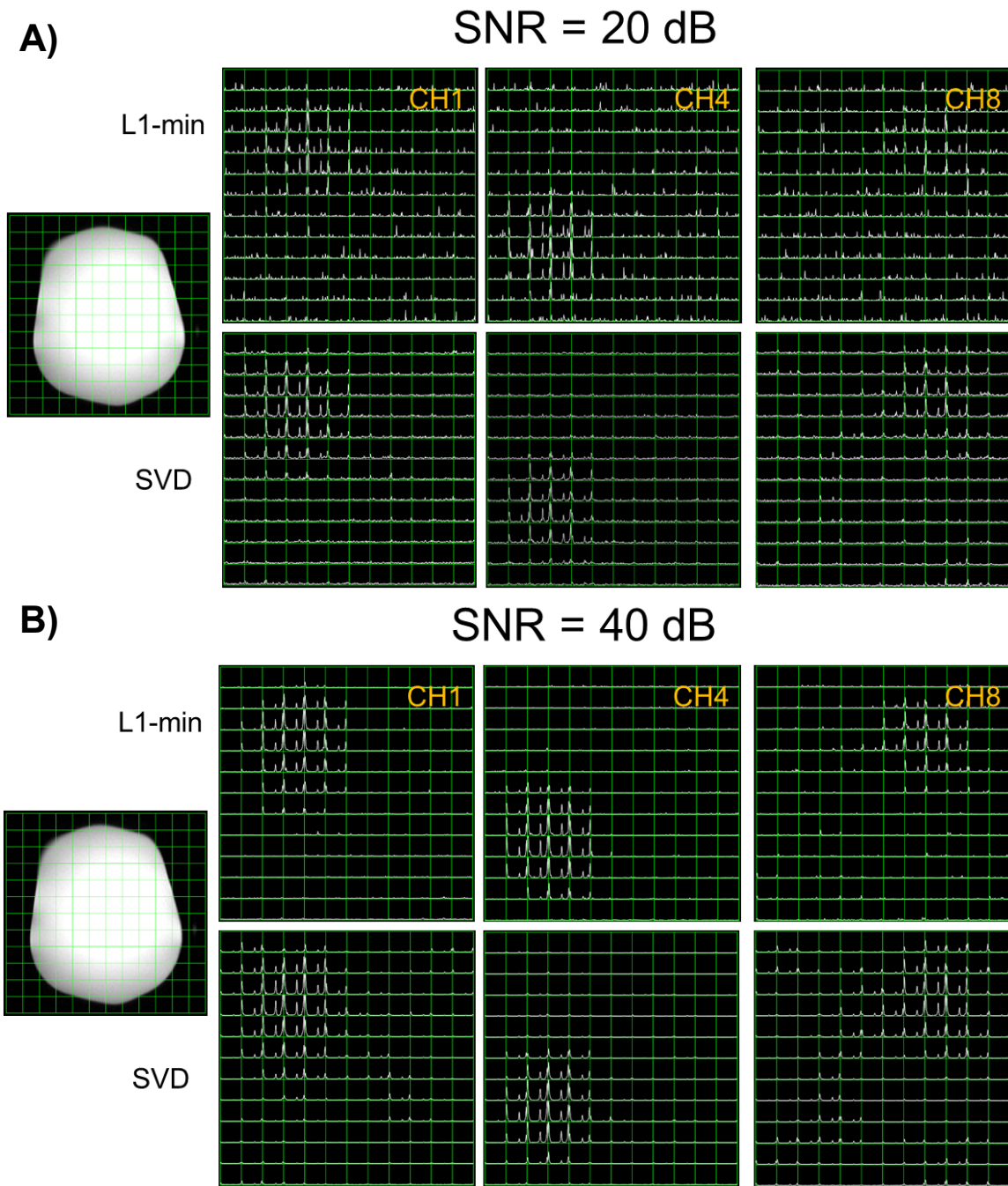
Figure 6.7 *Reconstruction of undersampled dataset using channel-by-channel L1-minimization CS algorithm versus SVD-based parallel reconstruction for data with added Gaussian noise **A)** 20dB and **B)** 40dB. Qualitatively the SVD reconstruction gives much less "speckle"-like noise at 20dB noise, while the performance of the two is comparable at 40dB.*

compartment three-site exchange model similar to Zierhut et al (163) and the variable flip angle scheme used for TRAMPs (Figure 6.6A). A urea dynamic curve was also generated using the standard Tofts signal model (115). The dynamics is then weighted by the sensitivity profile to create the simulation dataset. For HP-^{13}C pyruvate, lactate and urea, the chemical shift on the spectra was set based on average of in vivo datasets acquired on TRAMP mouse (Figure 6.6B). For each metabolite peak, the lineshape is Lorentzian with 0.8 ppm FWHM linewidth, determined based on what we observed on clinical patients.

White Gaussian noise was introduced to the originally noiseless 5D dataset, and the dataset was undersampled using the standard undersampling pattern for clinical HP-^{13}C prostate imaging. This was formulated as,

$$S_{simulation}(t) = S_{noiseless}(t) + n(t)$$

The noise was set such that peak SNR in the dataset was 10-45dB. Ideally the system noise would have been better modelled by a Rician distribution, but Gaussian noise model was applied here for the sake of simplicity and easy analysis. The original noiseless dataset can be found in Figure 6.6B. The matrix size was 12x12x16x59x18x8 for this simulation brain dataset.

Reconstruction using the new SVD-based algorithm and the conventional channel-by-channel L1-minimization both takes about 3-4 hours. The SNR=20dB dataset was depicted in Figure 6.7A. As can be seen in the spectroscopic dataset, the L1-minimization gives more "speckle"-like noise, while the SVD reconstruction appears to have much lower noise. The SNR=40dB dataset (Figure 6.7B) sees more similar performance between the two reconstruction methods. The SVD

154

reconstruction appears to give some "ghost" voxel artifacts on the opposite end of coil sensitive region, especially on Channel 8. This is due to the aliasing in coil sensitivity profile. In this case, the simulation-generated dataset needs to have an improved sensitivity map that excludes aliasing.
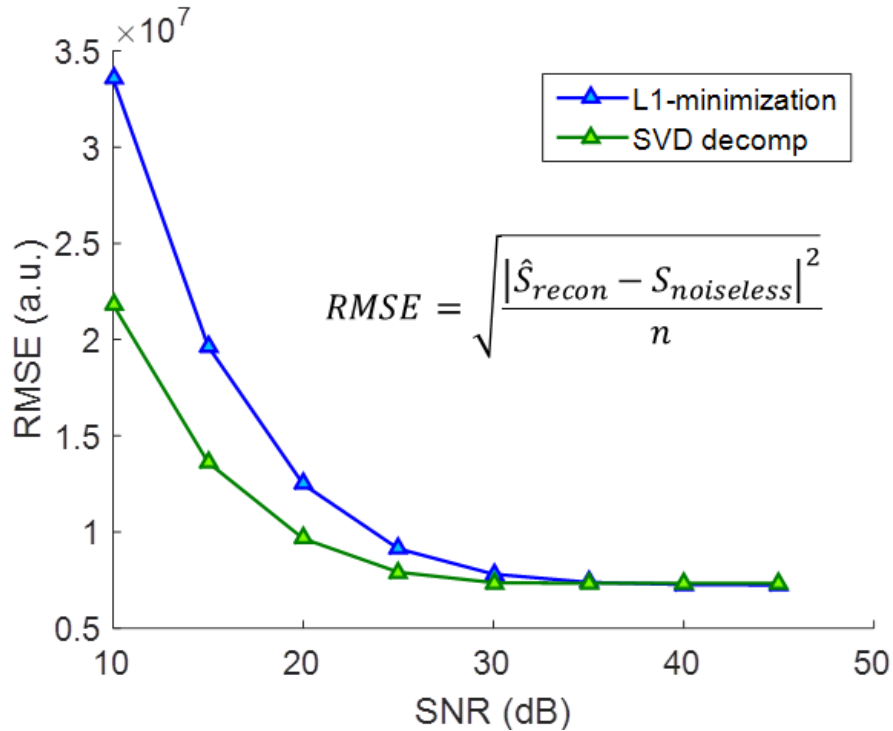
Figure 6.8 *The RMS error between simulation dataset with different SNR versus the noiseless dataset. The SVD-based reconstruction gives less RMSE in the low-SNR region (10-30dB), while the two reconstruction performs similarly at high SNR (>35dB). This can be important given reduced sensitivity and relatively low SNR in some clinical setups.*

The root mean square error (RMSE) between "noiseless" fully-sampled simulated dataset and the reconstructed dataset can serve as a benchmark for reconstruction error. Figure 6.8 illustrates the RMSE for the two methods under different peak noise SNR. With SNR = 10dB, the RMSE of L1-minimization algorithm was more than 1.6x that of the SVD parallel reconstruction. As anticipated, in high

SNR region (SNR>35dB), no significant difference in RMSE was found between the two methods. This is due to the inherent variation and bias that comes from reconstructing an undersampled dataset. The differential performance in low-SNR regions can be very important, especially with the generally reduced sensitivity in clinical setup, and the SNR-limited metabolites such as lactate and bicarbonate in some cases.
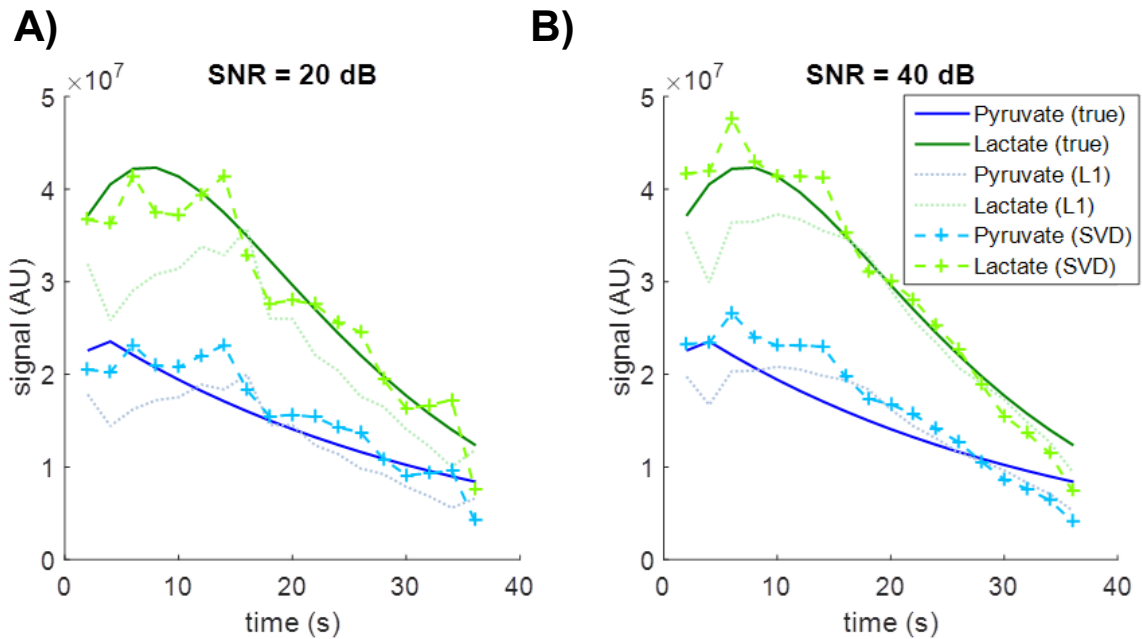
Figure 6.9 *Reconstructed dynamic curve at SNR **A)** 20dB and **B)** 40dB. While the curves from L1-minimization reconstruction appears slightly smoother, that from SVD reconstruction has smaller bias against the noiseless simulation curve.*

A closer examination of the temporal dimension was shown in Figure 6.9. Compared against the metabolite dynamics of pyruvate and lactate in the "noiseless" curves, the SVD-reconstructed dynamics seems to have a smaller bias (thick dashed line), while the L1-reconstructed curve is slightly smoother (thin dashed line).

Next we investigated the quantitative accuracy of the two reconstruction method in terms of k_{PL} estimation. The pyruvate-to-lactate exchange dynamics was fit to the same kinetic model that generated the "noiseless" data. In Figure 6.10, The k_{PL}
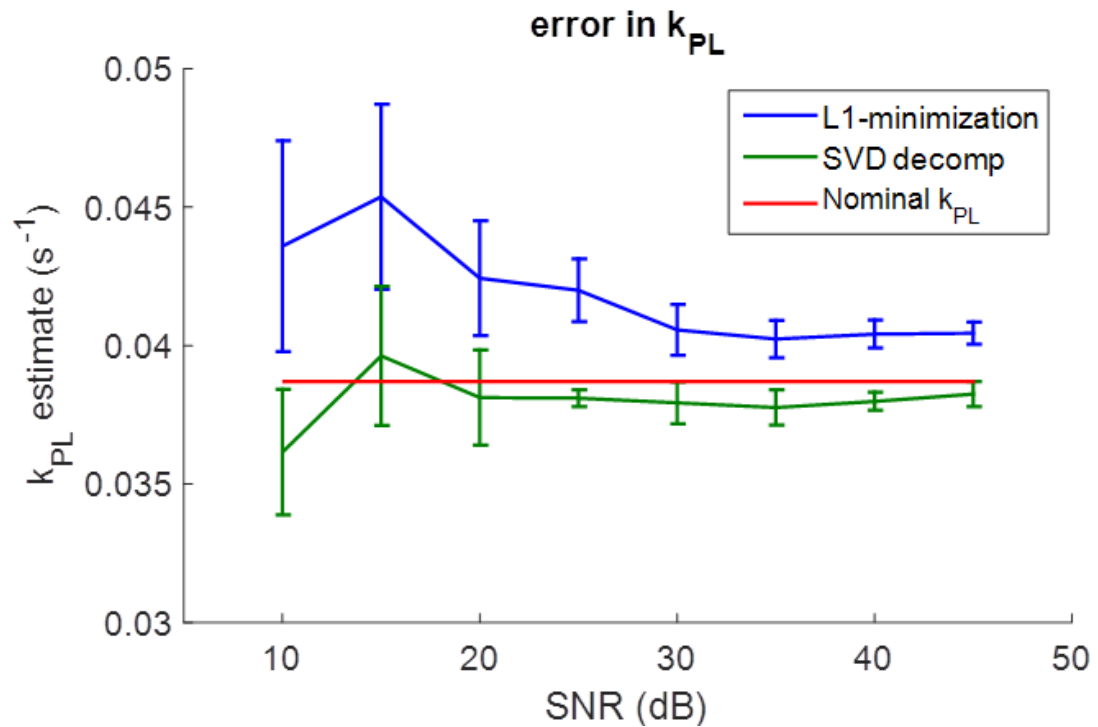
Figure 6.10 *The bias in k_{PL} was much smaller in the SVD-reconstructed dataset, while L1 and SVD perform similarly in terms of error.*

fits from both reconstruction methods were compared to the nominal k_{PL} used to generate the data. As it turns out, the bias in k_{PL} was much smaller in the SVD-reconstructed dataset, while both methods perform similarly in terms of error. Due to the computational cost, only 3 simulations were conducted for each SNR. Increasing the repetitions of simulation may provide a clearer picture about the quantitative performance of the two methods.

6.2.4 Human brain 3D dynamic HP-^{13}C imaging – from phase II clinical study

Introduction: HP-^{13}C studies on rat with human glioblastoma (GBM) xenograft suggested that increased lactate production has great potential to serve as a key biomarker for clinical assessment of prognosis and evaluating response to therapy (42). A 2D dynamic EPSI sequence is shown to consistently acquire HP-^{13}C spectroscopic images of brain tumor with good SNR. Preliminary findings suggested that the tumor region had higher lactate/bicarbonate ratio, while the contra-lateral brain showed higher lactate/pyruvate ratio. (185)
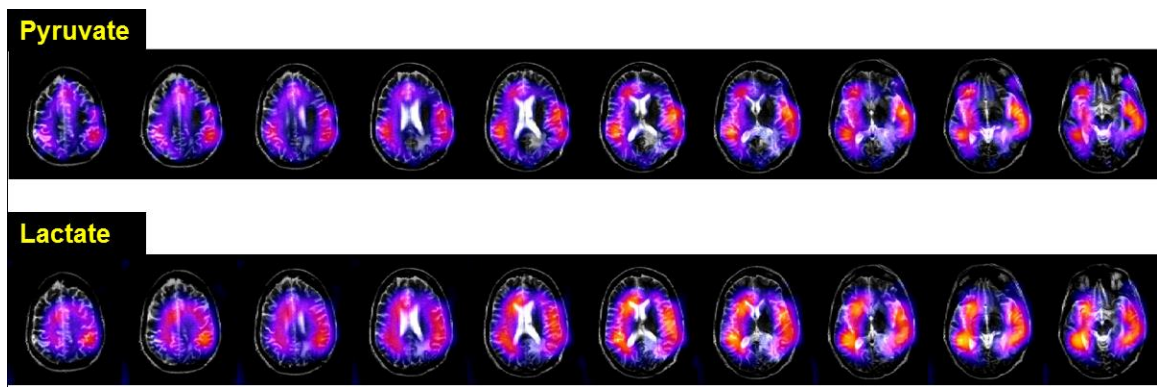
Figure 6.11 This GBM patient was imaged using 3D dynamic CS-EPSI sequence. Reconstruction was performed using the SVD-based method. Here the area under time curve (AUC) was overlaid over T$_2$-FSE anatomical references. Regions of HP-^{13}C pyruvate and lactate distribution were consistent with finding from our 2D EPSI images.

As described in Section 6.1, it would ultimately be beneficial to move to a full 3D acquisition for extra information in the normal brain as control, in addition to efficiently usage of magnetization in the whole brain. In this study, a GBM patient

was scanned using the 3D dynamic CS-EPSI sequence, and reconstruction was conducted by the SVD-based parallel imaging algorithm.

Methods: The HP-^{13}C clinical brain imaging setup includes a clamshell coil for transmit and an 8-channel array coil for receive. GMP [1-^{13}C]pyruvic acid was polarized in a 5T SpinLab polarizer for 2.5 hours, yielding 48.6% polarization of 232mM pyruvate and met all pharmacy specifications prior to injection for the clinical trial study conducted in accordance with the approved IND protocol. 32ml of pyruvate solution was injected at a rate of 5ml/s, followed by saline flush.

A patient with GBM was the subject of this study. The parameters for the 3D CS-EPSI sequence (11,12) were matrix size = 12x12x16, TR = 150ms, TE = 3.4ms, spatial resolution = 2cm isotropic, temporal resolution = 3s, FOV = 24x24x32(cm), spectral BW = 581Hz, acquisition window = 72s. A constant 10° flip angle was applied to all metabolites.

All simulations and the SVD parallel reconstruction was realized using MATLAB and conducted on UCSF's Radiology High-Performance Computing platform (the "Grid"). A three-site kinetic model with a boxcar input function, similar to the one reported by Zierhut et al. (163), was applied for quantitative estimation of pyruvate-to-lactate conversion rate k_{PL}.

Results and Discussions: For the clinical research glioblastoma imaging, the reconstruction on the HPC Grid required approximately 3.2 hours for the 6 dimensional dataset (x,y,z,f,temporal,coil) with a matrix size of 12x12x16x59x24x8. The efficiency of this reconstruction routine is dependent on many factors. First of all, a good strategy is essential to breakdown the reconstruction job into paralleled

A)

Pyruvate

Lactate

B)

lac   pyr

$k_{PL} = 0.0319$ (s^{-1})

184   172
Chemical shift (ppm)

C)
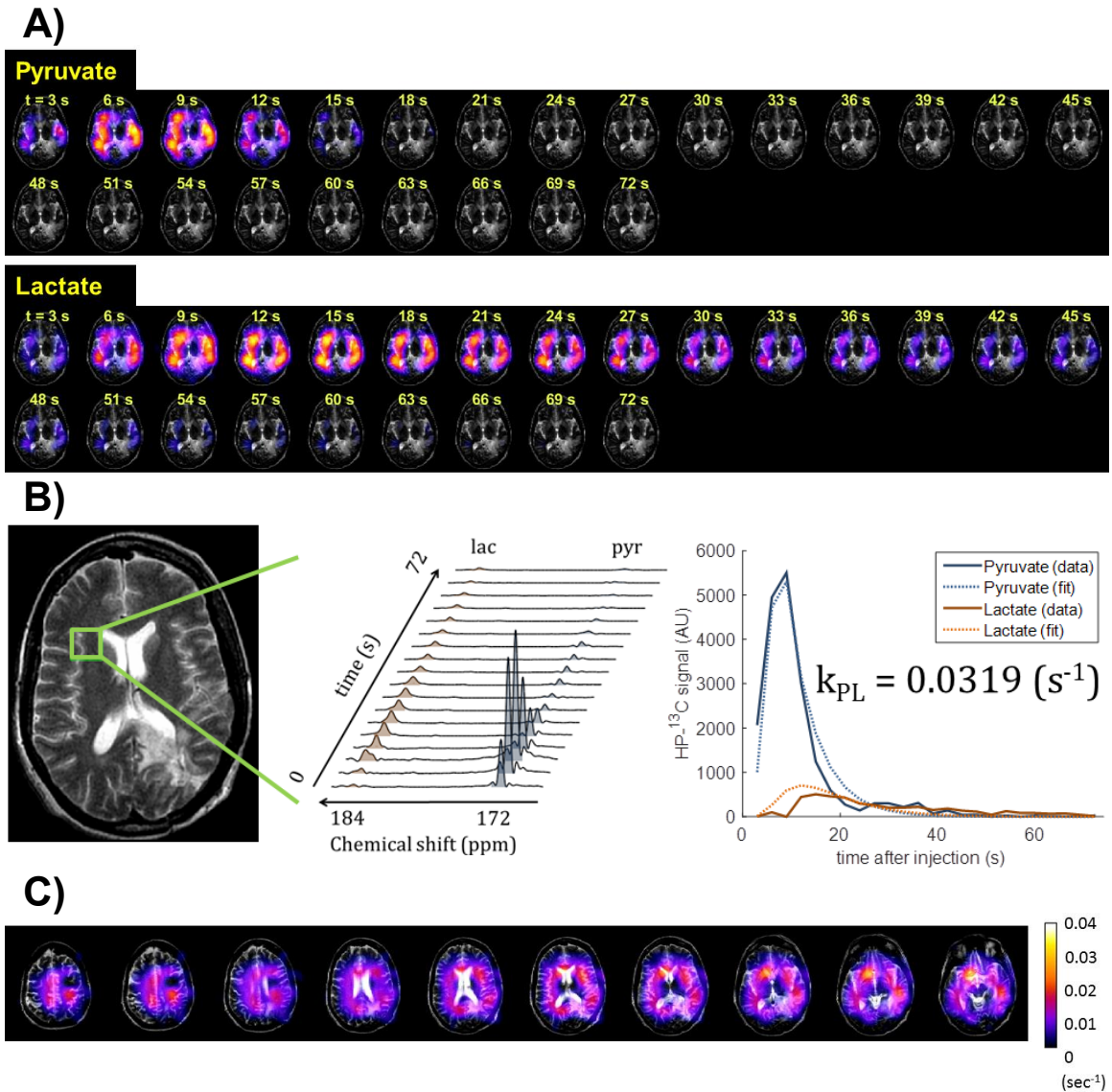
Figure 6.12 A) Pyruvate and lactate dynamics in this patient with GBM. The dynamics shows the conversion of pyruvate to lactate. B) Dynamic spectra from a voxel in normal brain region shows pyruvate bolus arrival at around 5-15 s from the end of injection, and lactate conversion observed beginning from 10s. C) Map of k_{PL} is consistent with 2D EPSI findings.

tasks. Moreover, the size of Hankel matrix and the number of singular values

included will determine allocation of resources, and thereby the computational

speed. Also, the number of iterations presents a key trade-off between dataset convergence and total reconstruction time.

The map of HP-^{13}C pyruvate and lactate signal area under time curve was depicted in Figure 6.11. The localization of metabolites in the brain is consistent with findings from previous 2D-dynamic EPSI images (185), suggesting that the new 3D dynamic acquisition and reconstruction strategies is able to adequately reflect the *in vivo* distribution of these biomarkers. The dynamic distribution of biomarkers are also shown in Figure 6.12A. Temporal dynamics of pyruvate and lactate was selected from a highly-perfused voxel in normal regions (Figure 6.12B). Pyruvate bolus arrival was observed between 5-20 sec from the end of injection, and lactate conversion was seen after 10 sec. The k_{PL} estimated from this voxel was 0.0319, consistent with previous human data, and the k_{PL} map (Figure 6.12C) was also consistent with 2D-EPSI findings.

Conclusions: The 3D dynamic CS-EPSI sequence, combined with SVD-based reconstruction on a high-performance computing platform created an efficient way of parallel imaging HP-^{13}C metabolism in human brain as an example, and is potentially applicable to other imaging targets.

6.3 Longitudinal Imaging of Prostate Cancer Patients using Hyperpolarized-^{13}C 3D Dynamic MRSI Techniques

6.3.1 Introduction

Hyperpolarized ^{13}C MRI is a new molecular imaging technology that provides more than 50,000x fold increase in signal for detection of pyruvate-lactate metabolism in patients (96). The 3D dynamic compressed-sensing EPSI (CS-EPSI) sequence was found to reproducibly provide good SNR with high spatiotemporal resolution in prostate cancer studies (180).

A pressing need in clinical management of prostate cancer is to non-invasively detect its aggressiveness, follow progression, and monitor treatment response. In Figure 1, a patient with biopsy-confirmed Gleason 4+5, 4+4 and 4+3 prostate cancer was studied using HP-^{13}C MRI before and after undergoing androgen deprivation therapy (ADT), and notable reduction in pyruvate-to-lactate metabolism was detected in the follow-up scan.

6.3.2 Materials and Methods

Pulse Sequences: The CS-ESPI sequence provided 3D dynamic imaging with high spatiotemporal resolution (11,12) including a multiband B_1^+-insensitive variable flip angle scheme (Section 5.5). Parameters included TR = 150ms, TE = 4.0ms, spatial resolution: 0.5cm^3 with FOV=9.6x9.6x12.8cm, temporal resolution = 2s, acquisition window = 42s.

HP MR experiments: GMP [1-^{13}C]pyruvic acid was polarized in a 5T Spinlab

polarizer for 2.5-3 hours (pre-therapy study: 245mM pyruvate, 36% polarization;

follow-up:226mM, 45%) and met all pharmacy specifications prior to injection for

Figure 6.13 A) *Patient with biopsy-confirmed Gleason 4+5, 4+4 and 4+3 prostate cancer involving a majority of the left lobe of the prostate and extending into the right peripheral zone. In the baseline study, the pyruvate-to-lactate conversion rate k_{PL} was 0.0273 (s^{-1}) over the tumor, and the regions of high k_{PL}, restricted diffusion (ADC=930), and low T2w intensity were consistent with biopsy findings.* ***B)*** *Follow-up after patient received ADT, the k_{PL} value substantially reduced to 0.0075 (s^{-1}), approximately 1/4 the baseline study. In tumor region, there was negligible change in tumor size on the T2w images, and only modest change in ADC, suggesting that HP-^{13}C can detect early treatment response.*

the clinical trial study conducted in accordance with the approved IND protocol. The

patient in Figure 6.13 received ADT with LHRH analogue, and underwent follow-up

study 6 weeks after the baseline scan.

Data Processing: HP-^{13}C MRSI datasets were reconstructed and processed using

MATLAB in combination with open-sourced SIVIC for display (114). k$_{PL}$ was

estimated using a three-site kinetic model with a boxcar input function (163).
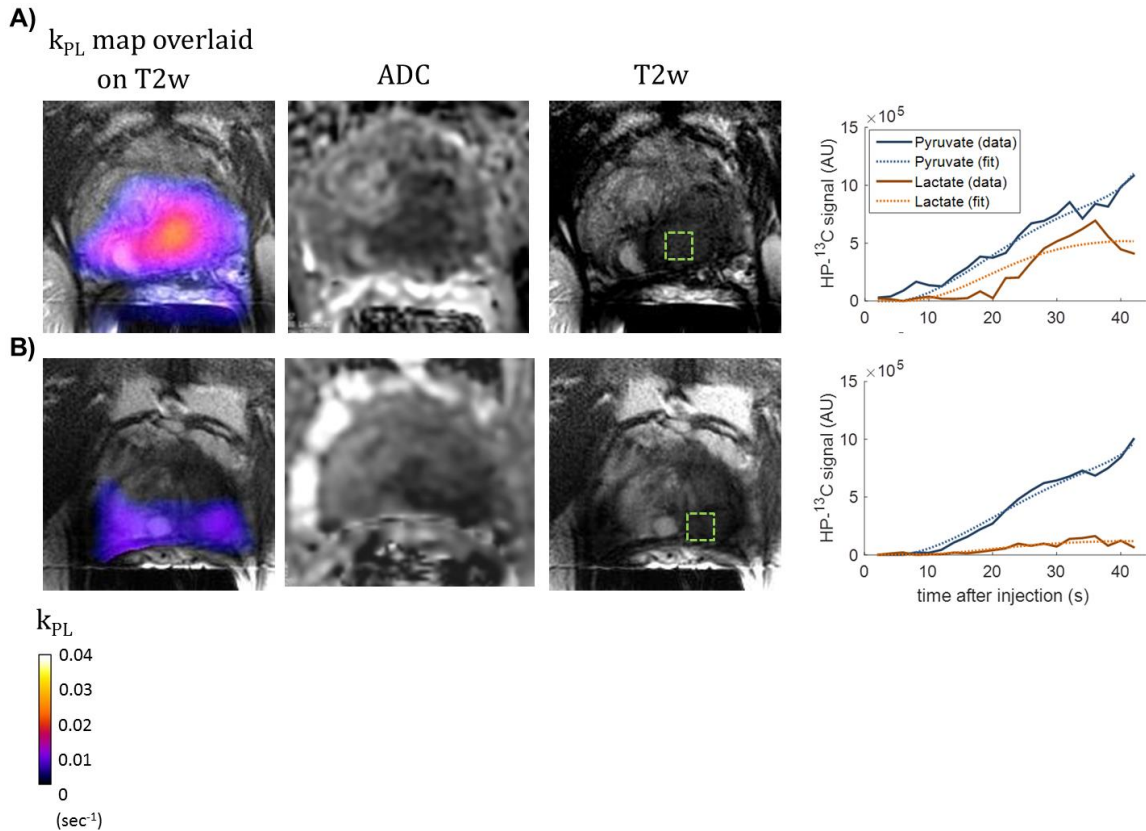
6.3.3 Results and Discussions

Figure 6.13 show data from a patient with biopsy-confirmed Gleason 4+5,

4+4 and 4+3 prostate cancer involving a majority of the left lobe of the prostate and

extending into the right peripheral zone. In the baseline study (Figure 6.13A), the

pyruvate-to-lactate conversion rate k$_{PL}$ was 0.0273 (s^{-1}) over the tumor, and the

regions of high k$_{PL}$, restricted diffusion (ADC=930), and low T2w intensity were

consistent with biopsy findings. The patient underwent ADT and docetaxel therapy,

and returned for follow-up scan 6 weeks after the baseline. In tumor region (Figure

6.13B), the k$_{PL}$ value substantially reduced to 0.0075 (s^{-1}), approximately 1/4 that of

the baseline study. Notably, on the follow-up scan there was negligible change in

tumor size on the T2w images, and only modest change in ADC was detected in

tumor region.

Therefore, this study indicated that the combination HP-^{13}C MRI and kinetic

models enabled quantitative detection of prostate cancer metabolism in patients.

More importantly, this outcome supported the role of HP-^{13}C MRI as a means to

detect early metabolic response prior to ascertainment of response using RECIST criteria (186).

6.3.4 Conclusions

The 3D dynamic HP-^{13}C MRI enabled non-invasive metabolic monitoring of treatment response in clinical prostate cancer, and has great potential to be integrated into the multi-parametric MRI of prostate malignancies.

Chapter 7 Conclusions

This dissertation project focused on translation of HP-^{13}C MRI from preclinical applications to a phase II clinical study. It consists of both technical developments and biomedical HP-^{13}C MRI research of human prostate cancer.

In Chapter 3, imaging and pathological studies were conducted on 19 transgenic mice of prostate cancer. Significant differences in pyruvate-to-lactate conversion were found between high- and low-grade tumor, which correlates well with pathological, gene expression, and isoenzyme activity assays.

Chapter 4 presents the first prostate patient study in a phase II clinical trial using the techniques developed through my dissertation project. This clinical research study was an integration of efforts including the preparation of sterile ^{13}C pyruvate sample by my pharmacy colleagues, the use of Spinlab polarizer, new coil setup for human data acqusisitions, and advanced compressed sensing 3D dynamic

MR sequence. Also included are the methods for image reconstruction and quantitative analysis used in phase II prostate study.

In Chapter 5, past quantitative methods were summarized for estimation HP-^{13}C metabolism and perfusion. HP-^{13}C imaging is a very interesting embodiment of Schrodinger's cat - observation of a state disrupts the state itself. Observation of chemical pools by pulse-and-acquire induces loss of HP-^{13}C magnetization. Therefore, a good strategy is essential to efficiently use magnetization, and a good model is a requisite to minimize the loss of information. Dynamic exchange models were proposed for both TRAMP animal imaging and clinical exams, and Akaike's information criterion was applied to select a model with relatively minimal information loss.

Finally, Chapter 6 summarizes some current and future works which includes new sampling pattern design for the 3D CS-EPSI sequence, and SVD parallel reconstruction for multi-channel MRSI brain data. Longitudinal imaging outcomes are also included for a prostate cancer patient before and after androgen deprivation therapy, where substantial reduction in k_{PL} can be a marker for early response of treatment.

HP-^{13}C MRI is an emerging molecular imaging that clearly could have wide research applications for cancer, diabetes, cardiovascular, inflammation and many other diseases that are associated with metabolic changes. Particularly for cancer, phase II clinical trial research studies of prostate, brain and liver have demonstrated its capabilities to provide high-quality data with reproducible quantitative outcomes. Such outcomes indicated the great potential of HP-^{13}C MRI to detect

cancer aggressiveness, follow progression, and monitor treatment response and metastases.

In the future, HP-^{13}C MRI of patients can be further advanced by the use of array coils for larger coverage, improved sensitivity, and parallel imaging for speed. New 3D sequence with improved under-sampling and flip angle design will allow even better SNR efficiency and faster acquisition. Moreover, the diversity of HP-^{13}C probes can provide wide variety of pathophysiological information ranging from metabolism, perfusion, pH, and even genetic and enzymatic pathways at a molecular level. Implementation of next-generation polarizers may provide high success rate of HP-^{13}C studies, and enable easier translation of experimental probes to clinical exams. Lastly, a HP-^{13}C patient database can be established to incorporate all the HP-^{13}C exams, multi-parametric MRI, and pathological data to allow correlation across a larger group of subjects using advanced analytic tools.

References

1. Ardenkjaer-Larsen JH, Fridlund B, Gram A, Hansson G, Hansson L, Lerche MH, *et al.* Increase in signal-to-noise ratio of > 10,000 times in liquid-state NMR. Proc Natl Acad Sci U S A **2003**;100:10158-63

2. Kohler SJ, Yen Y, Wolber J, Chen AP, Albers MJ, Bok R, *et al.* In vivo 13 carbon metabolic imaging at 3T with hyperpolarized 13C-1-pyruvate. Magn Reson Med **2007**;58:65-9

3. Kim JW, Dang CV. Cancer's molecular sweet tooth and the Warburg effect. Cancer Res **2006**;66:8927-30

4. Warburg O. On the origin of cancer cells. Science **1956**;123:309-14

5. Albers MJ, Bok R, Chen AP, Cunningham CH, Zierhut ML, Zhang VY, *et al.* Hyperpolarized 13C lactate, pyruvate, and alanine: noninvasive biomarkers for prostate cancer detection and grading. Cancer Res **2008**;68:8607-15

6. Keshari KR, Sriram R, Van Criekinge M, Wilson DM, Wang ZJ, Vigneron DB, *et al.* Metabolic reprogramming and validation of hyperpolarized 13C lactate as a prostate cancer biomarker using a human prostate tissue slice culture bioreactor. Prostate **2013**;73:1171-81

7. Society AC. Cancer Facts & Figures 2017. American Cancer Society **2017**

8. Ramon J, Denis LJ. Prostate Cancer. Springer-Verlag Berlin Heidelberg; 2007.

9. Dall'Era MA, Cooperberg MR, Chan JM, Davies BJ, Albertsen PC, Klotz LH, *et al.* Active surveillance for early-stage prostate cancer - Review of the current literature. Cancer **2008**;112:1650-9

10. Lu-Yao GL, Albertsen PC, Moore DF, Shih WC, Lin Y, DiPaola RS, *et al.* Outcomes of Localized Prostate Cancer Following Conservative Management. Jama-J Am Med Assoc **2009**;302:1202-9

11. Hu S, Lustig M, Balakrishnan A, Larson PEZ, Bok R, Kurhanewicz J, *et al.* 3D Compressed Sensing for Highly Accelerated Hyperpolarized C-13 MRSI With In Vivo Applications to Transgenic Mouse Models of Cancer. Magnet Reson Med **2010**;63:312-21

12. Larson PEZ, Hu S, Lustig M, Kerr AB, Nelson SJ, Kurhanewicz J, *et al.* Fast Dynamic 3D MR Spectroscopic Imaging With Compressed Sensing and Multiband Excitation Pulses for Hyperpolarized C-13 Studies. Magnet Reson Med **2011**;65:610-9

13. Xing Y, Reed GD, Pauly JM, Kerr AB, Larson PEZ. Optimal variable flip angle schemes for dynamic acquisition of exchanging hyperpolarized substrates. J Magn Reson **2013**;234:75-81

14. Cunningham CH, Chen AP, Albers MJ, Kurhanewicz J, Hurd RE, Yen YF, *et al.* Double spin-echo sequence for rapid spectroscopic imaging of hyperpolarized C-13. J Magn Reson **2007**;187:357-62

15. Hu S, Lustig M, Chen AP, Crane J, Kerr A, Kelley DAC, *et al.* Compressed sensing for resolution enhancement of hyperpolarized C-13 flyback 3D-MRSI. J Magn Reson **2008**;192:258-64

16. Nishimura DG. Principles of magnetic resonance imaging. Stanford University; 1996.

17. Levitt MH. Spin Dynamics: Basics of Nuclear Magnetic Resonance. Wiley; 2001.

18. Korosec FR, Frayne R, Grist TM, Mistretta CA. Time-resolved contrast-enhanced 3D MR angiography. Magnet Reson Med **1996**;36:345-51

19. Prince MR, Narasimham DL, Stanley JC, Chenevert TL, Williams DM, Marx V, *et al.* Breath-Hold Gadolinium-Enhanced Mr-Angiography of the Abdominal-Aorta and Its Major Branches. Radiology **1995**;197:785-92

20. Logothetis NK, Pauls J, Augath M, Trinath T, Oeltermann A. Neurophysiological investigation of the basis of the fMRI signal. Nature **2001**;412:150-7

21. Rombouts SARB, Barkhof F, Scheltens P. Clinical Applications of Functional Brain MRI. OUP Oxford; 2007.

22. Cline HE, Schenck JF, Hynynen K, Watkins RD, Souza SP, Jolesz FA. Mr-Guided Focused Ultrasound Surgery. J Comput Assist Tomo **1992**;16:956-65

23. Hynynen K, Pomeroy O, Smith DN, Huber PE, McDannold NJ, Kettenbach J, *et al.* MR imaging-guided focused ultrasound surgery of fibroadenomas in the breast: A feasibility study. Radiology **2001**;219:176-85

24. Kurhanewicz J, Swanson MG, Nelson SJ, Vigneron DB. Combined magnetic resonance imaging and spectroscopic imaging approach to molecular imaging of prostate cancer. J Magn Reson Imaging **2002**;16:451-63

25. Kurhanewicz J, Vigneron DB, Hricak H, Narayan P, Carroll P, Nelson SJ. Three-dimensional H-1 MR spectroscopic imaging of the in situ human prostate with high (0.24-0.1-cm(3)) spatial resolution. Radiology **1996**;198:795-805

26. Comment A, Merritt ME. Hyperpolarized Magnetic Resonance as a Sensitive Detector of Metabolic Function. Biochemistry-Us **2014**;53:7333-57

27. Noggle J. The nuclear Overhauser effect. Elsevier; 2012.

28. Overhauser AW. Polarization of Nuclei in Metals. Physical Review **1953**;92:411-5

29. Golman K, Olsson LE, Axelsson O, Mansson S, Karlsson M, Petersson JS. Silvanus Thompson Memorial Lecture Molecular imaging using hyperpolarized C-13. Brit J Radiol **2003**;76:S118-S27

30. Ardenkjaer-Larsen JH. On the present and future of dissolution-DNP. J Magn Reson **2016**;264:3-12

31. Hu S, Larson PEZ, VanCriekinge M, Leach AM, Park I, Leon C, *et al.* Rapid sequential injections of hyperpolarized [1-C-13]pyruvate in vivo using a sub-kelvin, multi-sample DNP polarizer. Magn Reson Imaging **2013**;31:490-6

32. Heiden MGV, Cantley LC, Thompson CB. Understanding the Warburg Effect: The Metabolic Requirements of Cell Proliferation. Science **2009**;324:1029-33

33. Altenberg B, Greulich KO. Genes of glycolysis are ubiquitously overexpressed in 24 cancer classes. Genomics **2004**;84:1014-20

34. Gatenby RA, Gillies RJ. Why do cancers have high aerobic glycolysis? Nat Rev Cancer **2004**;4:891-9

35. Kuhajda FP. Fatty-acid synthase and human cancer: new perspectives on its role in tumor biology. Nutrition **2000**;16:202-8

36.   Mankoff DA, Dunnwald LK, Gralow JR, Ellis GK, Charlop A, Lawton TJ, *et al.* Blood flow and metabolism in locally advanced breast cancer: Relationship to response to therapy. J Nucl Med **2002**;43:500-9

37.   Mankoff DA, Dunnwald LK, Partridge SC, Specht JM. Blood Flow-Metabolism Mismatch: Good for the Tumor, Bad for the Patient. Clin Cancer Res **2009**;15:5294-6

38.   Milosevic M, Warde P, Menard C, Chung P, Toi A, Ishkanian A, *et al.* Tumor Hypoxia Predicts Biochemical Failure following Radiotherapy for Clinically Localized Prostate Cancer. Clin Cancer Res **2012**;18:2108-14

39.   Korenchan DE, Flavell RR, Baligand C, Sriram R, Neumann K, Sukumar S, *et al.* Dynamic nuclear polarization of biocompatible C-13-enriched carbonates for in vivo pH imaging. Chem Commun **2016**;52:3030-3

40.   Keshari KR, Kurhanewicz J, Bok R, Larson PEZ, Vigneron DB, Wilson DM. Hyperpolarized C-13 dehydroascorbate as an endogenous redox sensor for in vivo metabolic imaging. P Natl Acad Sci USA **2011**;108:18606-11

41.   von Morze C, Bok RA, Reed GD, Ardenkjaer-Larsen JH, Kurhanewicz J, Vigneron DB. Simultaneous Multiagent Hyperpolarized C-13 Perfusion Imaging. Magnet Reson Med **2014**;72:1599-609

42.   Park I, Bok R, Ozawa T, Phillips JJ, James CD, Vigneron DB, *et al.* Detection of early response to temozolomide treatment in brain tumors using hyperpolarized 13C MR metabolic imaging. J Magn Reson Imaging **2011**;33:1284-90

43.   Laustsen C, Lycke S, Palm F, Ostergaard JA, Bibby BM, Norregaard R, *et al.* High altitude may alter oxygen availability and renal metabolism in diabetics as measured by hyperpolarized [1-C-13]pyruvate magnetic resonance imaging. Kidney Int **2014**;86:67-74

44.   Reed GD, von Morze C, Verkman AS, Koelsch BL, Chaumeil MM, Lustig M, *et al.* Imaging Renal Urea Handling in Rats at Millimeter Resolution Using Hyperpolarized Magnetic Resonance Relaxometry. Tomography **2016**;2:125-37

45.   Park I, Larson PEZ, Zierhut ML, Hu S, Bok R, Ozawa T, *et al.* Hyperpolarized C-13 magnetic resonance metabolic imaging: application to brain tumors. Neuro-Oncology **2010**;12:133-44

46.   Cunningham CH, Lau JYC, Chen AP, Geraghty BJ, Perks WJ, Roifman I, *et al.* Hyperpolarized C-13 Metabolic MRI of the Human Heart Initial Experience. Circ Res **2016**;119:1177-82

47.   Lau AZ, Chen AP, Ghugre NR, Ramanan V, Lam WW, Connelly KA, *et al.* Rapid Multislice Imaging of Hyperpolarized C-13 Pyruvate and Bicarbonate in the Heart. Magnet Reson Med **2010**;64:1323-31

48.   Korenchan DE, Taglang C, Von Morze C, Blecha JE, Gordon J, Sriram R, *et al.* Dicarboxylic Acids as pH Sensors for Hyperpolarized 13C Magnetic Resonance Spectroscopic Imaging. Analyst **2017**

49.   Lau AZ, Miller JJ, Tyler DJ. Mapping of intracellular pH in the in vivo rodent heart using hyperpolarized [1-13C]pyruvate. Magn Reson Med **2016**

50. Keshari KR, Wilson DM. Chemistry and biochemistry of C-13 hyperpolarized magnetic resonance using dynamic nuclear polarization. Chem Soc Rev **2014**;43:1627-59

51. Geraghty BJ, Lau JY, Chen AP, Cunningham CH. Accelerated 3D echo-planar imaging with compressed sensing for time-resolved hyperpolarized 13 C studies. Magn Reson Med **2017**;77:538-46

52. Gordon JW, Vigneron DB, Larson PE. Development of a symmetric echo planar imaging framework for clinical translation of rapid dynamic hyperpolarized 13 C imaging. Magn Reson Med **2017**;77:826-32

53. Milshteyn E, von Morze C, Reed GD, Shang H, Shin PJ, Zhu Z, *et al.* Development of high resolution 3D hyperpolarized carbon-13 MR molecular imaging techniques. Magn Reson Imaging **2017**;38:152-62

54. Reed G, von Morze C, Bok R, Koelsch B, Smith K, van Criekinge M, *et al.* High Resolution C-13 MRI with Hyperpolarized [C-13,N-15] Urea. Med Phys **2013**;40

55. Larson PEZ, Bok R, Kerr AB, Lustig M, Hu S, Chen AP, *et al.* Investigation of Tumor Hyperpolarized [1-C-13]-Pyruvate Dynamics Using Time-Resolved Multiband RF Excitation Echo-Planar MRSI. Magnet Reson Med **2010**;63:582-91

56. Yen YF, Kohler SJ, Chen AP, Tropp J, Bok R, Wolber J, *et al.* Imaging Considerations for In Vivo (13)C Metabolic Mapping Using Hyperpolarized (13)C-Pyruvate. Magnet Reson Med **2009**;62:1-10

57. Levin YS, Mayer D, Yen YF, Hurd RE, Spielman DM. Optimization of fast spiral chemical shift imaging using least squares reconstruction: Application for hyperpolarized C-13 metabolic imaging. Magnet Reson Med **2007**;58:245-52

58. Mayer D, Yen YF, Tropp J, Pfefferbaum A, Hurd RE, Spielman DM. Application of Subsecond Spiral Chemical Shift Imaging to Real-Time Multislice Metabolic Imaging of the Rat In Vivo after Injection of Hyperpolarized (13)C(1)-Pyruvate. Magnet Reson Med **2009**;62:557-64

59. Jiang WW, Lustig M, Larson PEZ. Concentric Rings K-Space Trajectory for Hyperpolarized C-13 MR Spectroscopic Imaging. Magnet Reson Med **2016**;75:19-31

60. Gordon J, Fain SB, Johnson K. Direct estimation of hyperpolarized metabolites with IDEAL spiral CSI. 2012. p 4299.

61. Wiesinger F, Weidl E, Menzel MI, Janich MA, Khegai O, Glaser SJ, *et al.* IDEAL spiral CSI for dynamic metabolic MR imaging of hyperpolarized [1-13C]pyruvate. Magnet Reson Med **2012**;68:8-16

62. Gordon JW, Niles DJ, Fain SB, Johnson KM. Joint spatial-spectral reconstruction and k-t spirals for accelerated 2D spatial/1D spectral imaging of 13C dynamics. Magn Reson Med **2014**;71:1435-45

63. Nishimura DG, Irarrazabal P, Meyer CH. A Velocity K-Space Analysis of Flow Effects in Echo-Planar and Spiral Imaging. Magnet Reson Med **1995**;33:549-56

64. Golman K, Petersson JS, Magnusson P, Johansson E, Akeson P, Chai CM, *et al.* Cardiac metabolism measured noninvasively by hyperpolarized C-13 MRI. Magnet Reson Med **2008**;59:1005-13

65. Cunningham CH, Chen AP, Lustig M, Hargreaves BA, Lupo J, Xu D, *et al.* Pulse sequence for dynamic volumetric imaging of hyperpolarized metabolic products. J Magn Reson **2008**;193:139-46

66. Dixon WT. Simple Proton Spectroscopic Imaging. Radiology **1984**;153:189-94

67. Lustig M, Donoho D, Pauly JM. Sparse MRI: The application of compressed sensing for rapid MR imaging. Magnet Reson Med **2007**;58:1182-95

68. Feng YS, Gordon JW, Shin PJ, von Morze C, Lustig M, Larson PEZ, *et al.* Development and testing of hyperpolarized C-13 MR calibrationless parallel imaging. J Magn Reson **2016**;262:1-7

69. Gordon JW, Feng Y, Shin P, Vigneron DB, Larson PEZ. 3D Hyperpolarized C-13 EPI with Calibrationless Parallel Imaging. ISMRM. Hawaii, HI2017.

70. Cao P, Shin PJ, Park I, Najac C, Marco-Rius I, Vigneron DB, *et al.* Accelerated High-Bandwidth MR Spectroscopic Imaging Using Compressed Sensing. Magnet Reson Med **2016**;76:369-79

71. Wolf AMD, Wender RC, Etzioni RB, Thompson IM, D'Amico AV, Volk RJ, *et al.* American Cancer Society Guideline for the Early Detection of Prostate Cancer Update 2010. Ca-Cancer J Clin **2010**;60:70-98

72. Catalona WJ, Richie JP, Ahmann FR, Hudson MA, Scardino PT, Flanigan RC, *et al.* Comparison of Digital Rectal Examination and Serum Prostate Specific Antigen in the Early Detection of Prostate Cancer: Results of a Multicenter Clinical Trial of 6,630 Men. J Urol **2017**;197:S200-S7

73. Friedman GD, Hiatt RA, Quesenberry CP, Jr., Selby JV. Case-control study of screening for prostatic cancer by digital rectal examinations. Lancet **1991**;337:1526-9

74. Stephenson RA. Prostate cancer trends in the era of prostate-specific antigen. An update of incidence, mortality, and clinical factors from the SEER database. Urol Clin North Am **2002**;29:173-81

75. Fradet V, Kurhanewicz J, Cowan JE, Karl A, Coakley FV, Shinohara K, *et al.* Prostate Cancer Managed with Active Surveillance: Role of Anatomic MR Imaging and MR Spectroscopic Imaging. Radiology **2010**;256:176-83

76. Kurhanewicz J, Vigneron DB. Magnetic Resonance Spectroscopy of Prostate Cancer. eMagRes **2016**

77. Denmeade SR, Isaacs JT. A history of prostate cancer treatment. Nat Rev Cancer **2002**;2:389-96

78. Mostaghel EA, Page ST, Lin DW, Fazli L, Coleman IM, True LD, *et al.* Intraprostatic androgens and androgen-regulated gene expression persist after testosterone suppression: therapeutic implications for castration-resistant prostate cancer. Cancer Res **2007**;67:5033-41

79. D'Amico AV, Whittington R, Malkowicz SB, Schultz D, Blank K, Broderick GA, *et al.* Biochemical outcome after radical prostatectomy, external beam radiation therapy, or interstitial radiation therapy for clinically localized prostate cancer. Jama-J Am Med Assoc **1998**;280:969-74

80. Menon M, Shrivastava A, Tewari A, Sarle R, Hemal A, Peabody JO, *et al.* Laparoscopic and robot assisted radical prostatectomy: establishment of a

structured program and preliminary analysis of outcomes. J Urol **2002**;168:945-9

81.   Brierley JD, Gospodarowicz MK, Wittekind C. TNM classification of malignant tumours. John Wiley & Sons; 2016.

82.   Tewari AK. Prostate cancer: A comprehensive perspective. Springer Science & Business Media; 2013.

83.   Epstein JI, Amin MB, Reuter VE, Humphrey PA. Contemporary Gleason Grading of Prostatic Carcinoma: An Update With Discussion on Practical Issues to Implement the 2014 International Society of Urological Pathology (ISUP) Consensus Conference on Gleason Grading of Prostatic Carcinoma. Am J Surg Pathol **2017**;41:e1-e7

84.   Carter HB, Hamper UM, Sheth S, Sanders RC, Epstein JI, Walsh PC. Evaluation of transrectal ultrasound in the early detection of prostate cancer. J Urol **1989**;142:1008-10

85.   Lee F, Gray JM, McLeary RD, Meadows TR, Kumasaka GH, Borlaza GS*, et al.* Transrectal ultrasound in the diagnosis of prostate cancer: location, echogenicity, histopathology, and staging. Prostate **1985**;7:117-29

86.   Bostwick DG. Grading prostate cancer. Am J Clin Pathol **1994**;102:S38-56

87.   Noguchi M, Stamey TA, McNEAL JE, Yemoto CM. Relationship between systematic biopsies and histological features of 222 radical prostatectomy specimens: lack of prediction of tumor significance for men with nonpalpable prostate cancer. The Journal of urology **2001**;166:104-10

88.   Steinberg DM, Sauvageot J, Piantadosi S, Epstein JI. Correlation of prostate needle biopsy and radical prostatectomy Gleason grade in academic and community settings. Am J Surg Pathol **1997**;21:566-76

89.   Beltran H, Yelensky R, Frampton GM, Park K, Downing SR, MacDonald TY*, et al.* Targeted next-generation sequencing of advanced prostate cancer identifies potential therapeutic targets and disease heterogeneity. Eur Urol **2013**;63:920-6

90.   Kantoff PW, Higano CS, Shore ND, Berger ER, Small EJ, Penson DF*, et al.* Sipuleucel-T immunotherapy for castration-resistant prostate cancer. N Engl J Med **2010**;363:411-22

91.   Kurhanewicz J, Vigneron DB. Advances in MR spectroscopy of the prostate. Magn Reson Imaging Clin N Am **2008**;16:697-710, ix-x

92.   Haider MA, van der Kwast TH, Tanguay J, Evans AJ, Hashmi AT, Lockwood G, *et al.* Combined T2-weighted and diffusion-weighted MRI for localization of prostate cancer. AJR Am J Roentgenol **2007**;189:323-8

93.   Noworolski S, Henry R, Vigneron D, Kurhanewicz J. Dynamic contrast-enhanced MRI in normal and abnormal prostate tissues as defined by biopsy, MRI, and 3D MRSI. Magnet Reson Med **2005**;53:249-55

94.   Coakley FV, Kurhanewicz J, Lu Y, Jones KD, Swanson MG, Chang SD*, et al.* Prostate cancer tumor volume: measurement with endorectal MR and MR spectroscopic imaging. Radiology **2002**;223:91-7

95.   Tran TKC, Vigneron DB, Sailasuta N, Tropp J, Le Roux P, Kurhanewicz J*, et al.* Very selective suppression pulses for clinical MRSI studies of brain and prostate cancer. Magnet Reson Med **2000**;43:23-33

96.   Nelson SJ, Kurhanewicz J, Vigneron DB, Larson PE, Harzstark AL, Ferrone M, *et al.* Metabolic imaging of patients with prostate cancer using hyperpolarized [1-(1)(3)C]pyruvate. Sci Transl Med **2013**;5:198ra08

97.   Society AC. Cancer facts & figures. The Society; 2015.

98.   Eggener SE, Mueller A, Berglund RK, Ayyathurai R, Soloway C, Soloway MS, *et al.* A multi-institutional evaluation of active surveillance for low risk prostate cancer. J Urol **2013**;189:S19-25; discussion S

99.   Chang ST, Westphalen AC, Jha P, Jung AJ, Carroll PR, Kurhanewicz J, *et al.* Endorectal MRI and MR spectroscopic imaging of prostate cancer: developing selection criteria for MR-guided focal therapy. J Magn Reson Imaging **2014**;39:519-25

100. Muller BG, Futterer JJ, Gupta RT, Katz A, Kirkham A, Kurhanewicz J, *et al.* The role of magnetic resonance imaging (MRI) in focal therapy for prostate cancer: recommendations from a consensus panel. BJU Int **2014**;113:218-27

101. Keshari KR, Sriram R, Van Criekinge M, Wilson DM, Wang ZJ, Vigneron DB, *et al.* Metabolic Reprogramming and Validation of Hyperpolarized 13C Lactate as a Prostate Cancer Biomarker Using a Human Prostate Tissue Slice Culture Bioreactor. The Prostate **2013**;73:1171-81

102. Wilson DM, Kurhanewicz J. Hyperpolarized 13C MR for molecular imaging of prostate cancer. J Nucl Med **2014**;55:1567-72

103. Costello LC, Franklin RB, Zou J, Feng P, Bok R, Swanson MG, *et al.* Human prostate cancer ZIP1/zinc/citrate genetic/metabolic relationship in the TRAMP prostate cancer animal model. Cancer Biol Ther **2011**;12:1078-84

104. Gingrich JR, Barrios RJ, Foster BA, Greenberg NM. Pathologic progression of autochthonous prostate cancer in the TRAMP model. Prostate Cancer Prostatic Dis **1999**;2:70-5

105. Kurhanewicz J, Vigneron DB, Brindle K, Chekmenev EY, Comment A, Cunningham CH*, et al.* Analysis of Cancer Metabolism by Imaging Hyperpolarized Nuclei: Prospects for Translation to Clinical Research. Neoplasia **2011**;13:81-97

106. Beauregard JM, Williams SG, Degrado TR, Roselt P, Hicks RJ. Pilot comparison of F-fluorocholine and F-fluorodeoxyglucose PET/CT with conventional imaging in prostate cancer. J Med Imaging Radiat Oncol **2010**;54:325-32

107. Farsad M, Schiavina R, Franceschelli A, Sanguedolce F, Castellucci P, Bertaccini A*, et al.* Positron-emission tomography in imaging and staging prostate cancer. Cancer Biomark **2008**;4:277-84

108. Kim J-w, Gardner LB, Dang CV. Oncogenic alterations of metabolism and the Warburg effect. Drug Discovery Today: Disease Mechanisms **2005**;2:233-8

109. Larson PE, Hu S, Lustig M, Kerr AB, Nelson SJ, Kurhanewicz J, *et al.* Fast dynamic 3D MR spectroscopic imaging with compressed sensing and multiband excitation pulses for hyperpolarized 13C studies. Magn Reson Med **2011**;65:610-9

110. Bahrami N, Swisher CL, Von Morze C, Vigneron DB, Larson PE. Kinetic and perfusion modeling of hyperpolarized (13)C pyruvate and urea in cancer with arbitrary RF flip angles. Quant Imaging Med Surg **2014**;4:24-32

111. Wilson DM, Keshari KR, Larson PE, Chen AP, Hu S, Van Criekinge M, *et al.* Multi-compound polarization by DNP allows simultaneous assessment of multiple enzymatic activities in vivo. J Magn Reson **2010**;205:141-7

112. von Morze C, Larson PEZ, Hu S, Keshari K, Wilson DM, Ardenkjaer-Larsen JH, *et al.* Imaging of blood flow using hyperpolarized [13C]Urea in preclinical cancer models. J Magn Reson Imaging **2011**;33:692-7

113. Hu S, Lustig M, Balakrishnan A, Larson PE, Bok R, Kurhanewicz J, *et al.* 3D compressed sensing for highly accelerated hyperpolarized (13)C MRSI with in vivo applications to transgenic mouse models of cancer. Magn Reson Med **2010**;63:312-21

114. Crane JC, Olson MP, Nelson SJ. SIVIC: Open-Source, Standards-Based Software for DICOM MR Spectroscopy Workflows. Int J Biomed Imaging **2013**;2013:169526

115. Tofts PS, Brix G, Buckley DL, Evelhoch JL, Henderson E, Knopp MV, *et al.* Estimating kinetic parameters from dynamic contrast-enhanced T(1)-weighted MRI of a diffusable tracer: standardized quantities and symbols. J Magn Reson Imaging **1999**;10:223-32

116. Swisher CL, Larson PEZ, Kruttwig K, Kerr AB, Hu S, Bok RA, *et al.* Quantitative measurement of cancer metabolism using stimulated echo hyperpolarized carbon-13 MRS. Magnet Reson Med **2014**;71:1-11

117. Feron O. Pyruvate into lactate and back: From the Warburg effect to symbiotic energy fuel exchange in cancer cells. Radiother Oncol **2009**;92:329-33

118. Hirschhaeuser F, Sattler UG, Mueller-Klieser W. Lactate: a metabolic key player in cancer. Cancer Res **2011**;71:6921-5

119. Petrelli F, Cabiddu M, Coinu A, Borgonovo K, Ghilardi M, Lonati V, *et al.* Prognostic role of lactate dehydrogenase in solid tumors: a systematic review and meta-analysis of 76 studies. Acta Oncol **2015**;54:961-70

120. Wulaningsih W, Holmberg L, Garmo H, Malmstrom H, Lambe M, Hammar N, *et al.* Serum lactate dehydrogenase and survival following cancer diagnosis. Br J Cancer **2015**;113:1389-96

121. Ryan CJ, Smith MR, Fizazi K, Saad F, Mulders PF, Sternberg CN, *et al.* Abiraterone acetate plus prednisone versus placebo plus prednisone in chemotherapy-naive men with metastatic castration-resistant prostate cancer (COU-AA-302): final overall survival analysis of a randomised, double-blind, placebo-controlled phase 3 study. Lancet Oncol **2015**;16:152-60

122. DeBerardinis RJ, Thompson CB. Cellular Metabolism and Disease: What Do Metabolic Outliers Teach Us? Cell **2012**;148:1132-44

123. Kroemer G, Pouyssegur J. Tumor cell metabolism: Cancer's Achilles' heel. Cancer Cell **2008**;13:472-82

124. Tessem MB, Swanson MG, Keshari KR, Albers MJ, Joun D, Tabatabai ZL, *et al.* Evaluation of lactate and alanine as metabolic biomarkers of prostate cancer using H-1 HR-MAS spectroscopy of biopsy tissues. Magnet Reson Med **2008**;60:510-6

125. Nelson SJ, Kurhanewicz J, Vigneron DB, Larson PEZ, Harzstark AL, Ferrone M, *et al.* Metabolic Imaging of Patients with Prostate Cancer Using Hyperpolarized [1-C-13]Pyruvate. Sci Transl Med **2013**;5

126. Dimmer KS, Friedrich B, Lang F, Deitmer JW, Broer S. The low-affinity monocarboxylate transporter MCT4 is adapted to the export of lactate in highly glycolytic cells. Biochem J **2000**;350 Pt 1:219-27

127. Parks SK, Chiche J, Pouyssegur J. Disrupting proton dynamics and energy metabolism for cancer therapy. Nat Rev Cancer **2013**;13:611-23

128. Korenchan D, Flavell R, Baligand C, Sriram R, Neumann K, Sukumar S, *et al.* Dynamic nuclear polarization of biocompatible 13 C-enriched carbonates for in vivo pH imaging. Chemical Communications **2016**

129. Estrella V, Chen T, Lloyd M, Wojtkowiak J, Cornnell HH, Ibrahim-Hashim A, *et al.* Acidity generated by the tumor microenvironment drives local invasion. Cancer Res **2013**;73:1524-35

130. Gatenby RA, Gawlinski ET, Gmitro AF, Kaylor B, Gillies RJ. Acid-mediated tumor invasion: a multidisciplinary study. Cancer Res **2006**;66:5216-23

131. Fukumura D, Xu L, Chen Y, Gohongi T, Seed B, Jain RK. Hypoxia and acidosis independently up-regulate vascular endothelial growth factor transcription in brain tumors in vivo. Cancer Res **2001**;61:6020-4

132. Lardner A. The effects of extracellular pH on immune function. J Leukoc Biol **2001**;69:522-30

133. Coller HA. Is Cancer a Metabolic Disease? Am J Pathol **2014**;184:4-17

134. Dhup S, Dadhich RK, Porporato PE, Sonveaux P. Multiple biological activities of lactic acid in cancer: influences on tumor growth, angiogenesis and metastasis. Curr Pharm Des **2012**;18:1319-30

135. Wang L, Chen Z, Wang Q, Cao W, Jian Y, Wang S, *et al.* [Expression of hypoxia-inducible factor 1 alpha and vascular endothelial growth factor in prostate cancer and its significance]. Zhonghua nan ke xue= National journal of andrology **2006**;12:57-9

136. Matsumoto S, Batra S, Saito K, Yasui H, Choudhuri R, Gadisetti C, *et al.* Antiangiogenic agent sunitinib transiently increases tumor oxygenation and suppresses cycling hypoxia. Cancer Res **2011**;71:6350-9

137. Oto A, Yang C, Kayhan A, Tretiakova M, Antic T, Schmid-Tannwald C, *et al.* Diffusion-Weighted and Dynamic Contrast-Enhanced MRI of Prostate Cancer: Correlation of Quantitative MR Parameters With Gleason Score and Tumor Angiogenesis. Am J Roentgenol **2011**;197:1382-90

138. Peng YH, Jiang YL, Yang C, Brown JB, Antic T, Sethi I, *et al.* Quantitative Analysis of Multiparametric Prostate MR Images: Differentiation between Prostate Cancer and Normal Tissue and Correlation with Gleason Score-A Computer-aided Diagnosis Development Study. Radiology **2013**;267:787-96

139. Cunningham CH, Chen AP, Albers MJ, Kurhanewicz J, Hurd RE, Yen YF, *et al.* Double spin-echo sequence for rapid spectroscopic imaging of hyperpolarized 13C. J Magn Reson **2007**;187:357-62

140. Kazan SM, Reynolds S, Kennerley A, Wholey E, Bluff JE, Berwick J, *et al.* Kinetic Modeling of Hyperpolarized C-13 Pyruvate Metabolism in Tumors

Using a Measured Arterial Input Function. Magnet Reson Med **2013**;70:943-53

141. Khegai O, Schulte RF, Janich MA, Menzel MI, Farrell E, Otto AM, *et al.* Apparent rate constant mapping using hyperpolarized [1-C-13]pyruvate. Nmr Biomed **2014**;27:1256-65

142. Bankson JA, Walker CM, Ramirez MS, Stefan W, Fuentes D, Merritt ME, *et al.* Kinetic Modeling and Constrained Reconstruction of Hyperpolarized [1-C-13]-Pyruvate Offers Improved Metabolic Imaging of Tumors. Cancer Research **2015**;75:4708-17

143. Brindle K. New approaches for imaging tumour responses to treatment. Nat Rev Cancer **2008**;8:94-107

144. Day SE, Kettunen MI, Gallagher FA, Hu DE, Lerche M, Wolber J, *et al.* Detecting tumor response to treatment using hyperpolarized C-13 magnetic resonance imaging and spectroscopy (vol 13, pg 1382, 2007). Nat Med **2007**;13:1521-

145. Golman K, in't Zandt R, Lerche M, Pehrson R, Ardenkjaer-Larsen JH. Metabolic imaging by hyperpolarized C-13 magnetic resonance imaging for in vivo tumor diagnosis. Cancer Research **2006**;66:10855-60

146. Golman K, in't Zandt R, Thaning M. Real-time metabolic imaging. P Natl Acad Sci USA **2006**;103:11270-5

147. Ishii M, Emami K, Kadlecek S, Petersson JS, Golman K, Vahdat V, *et al.* Hyperpolarized C-13 MRI of the pulmonary vasculature and parenchyma. Magnet Reson Med **2007**;57:459-63

148. Merritt ME, Harrison C, Storey C, Jeffrey FM, Sherry AD, Malloy CR. Hyperpolarized C-13 allows a direct measure of flux through a single enzyme-catalyzed step by NMR. P Natl Acad Sci USA **2007**;104:19773-7

149. Nelson SJ, Vigneron D, Kurhanewicz J, Chen A, Bok R, Hurd R. DNP-hyperpolarized C-13 magnetic resonance metabolic imaging for cancer applications. Appl Magn Reson **2008**;34:533-44

150. Wang L, Hricak H, Kattan MW, Chen HN, Scardino PT, Kuroiwa K. Prediction of organ-confined prostate cancer: Incremental value of MR imaging and MR spectroscopic imaging to staging nomograms. Radiology **2006**;238:597-603

151. Bill-Axelson A, Holmberg L, Ruutu M, Haggman M, Andersson SO, Bratell S, *et al.* Radical prostatectomy versus watchful waiting in early prostate cancer. New Engl J Med **2005**;352:1977-84

152. Carroll PR. Early stage prostate cancer - Do we have a problem with over-detection, overtreatment or both? J Urology **2005**;173:1061-2

153. Draisma G, Boer R, Otto SJ, van der Cruijsen IW, Damhuis RAM, Schroder FH, *et al.* Lead times and overdetection due to prostate-specific antigen screening: Estimates from the European randomized study of screening for prostate cancer. J Natl Cancer I **2003**;95:868-78

154. Etzioni R, Penson DF, Legler JM, Di Tommaso D, Boer R, Gann PH, *et al.* Overdiagnosis due to prostate-specific antigen screening: lessons from US prostate cancer incidence trends. J Natl Cancer I **2002**;94:981-90

155. Johansson JE, Andren O, Andersson SO, Dickman PW, Holmberg L, Magnuson A, *et al.* Natural history of early, localized prostate cancer. Jama-J Am Med Assoc **2004**;291:2713-9

156. Dafni H, Larson PEZ, Hu S, Yoshihara HAI, Ward CS, Venkatesh HS, *et al.* Hyperpolarized C-13 Spectroscopic Imaging Informs on Hypoxia-Inducible Factor-1 and Myc Activity Downstream of Platelet-Derived Growth Factor Receptor. Cancer Research **2010**;70:7400-10

157. Josan S, Yen YF, Hurd R, Pfefferbaum A, Spielman D, Mayer D. Application of double spin echo spiral chemical shift imaging to rapid metabolic mapping of hyperpolarized [1-(1)(3)C]-pyruvate. J Magn Reson **2011**;209:332-6

158. Lodi A, Woods SM, Ronen SM. Treatment with the MEK inhibitor U0126 induces decreased hyperpolarized pyruvate to lactate conversion in breast, but not prostate, cancer cells. Nmr in Biomedicine **2013**;26:299-306

159. Hu S, Chen AP, Zierhut ML, Bok R, Yen YF, Schroeder MA, *et al.* In Vivo Carbon-13 Dynamic MRS and MRSI of Normal and Fasted Rat Liver with Hyperpolarized C-13-Pyruvate. Mol Imaging Biol **2009**;11:399-407

160. Schroeder MA, Lau AZ, Chen AP, Gu Y, Nagendran J, Barry J, *et al.* Hyperpolarized 13C magnetic resonance reveals early-and late-onset changes to in vivo pyruvate metabolism in the failing heart. European journal of heart failure **2013**;15:130-40

161. Chen YR, Kim H, Bok R, Sukumar S, Mu X, Sheldon RA, *et al.* Pyruvate to Lactate Metabolic Changes during Neurodevelopment Measured Dynamically Using Hyperpolarized C-13 Imaging in Juvenile Murine Brain. Dev Neurosci-Basel **2016**;38:34-40

162. Maidens J, Gordon JW, Arcak M, Larson PEZ. Optimizing Flip Angles for Metabolic Rate Estimation in Hyperpolarized Carbon-13 MRI. Ieee T Med Imaging **2016**;35:2403-12

163. Zierhut ML, Yen YF, Chen AP, Bok R, Albers MJ, Zhang V, *et al.* Kinetic modeling of hyperpolarized 13C1-pyruvate metabolism in normal rats and TRAMP mice. J Magn Reson **2010**;202:85-92

164. Noworolski SM, Reed GD, Kurhanewicz J, Vigneron DB. Post-Processing Correction of the Endorectal Coil Reception Effects in MR Spectroscopic Imaging of the Prostate. J Magn Reson Imaging **2010**;32:654-62

165. Shin PJ, Larson PE, Ohliger MA, Elad M, Pauly JM, Vigneron DB, *et al.* Calibrationless parallel imaging reconstruction based on structured low-rank matrix completion. Magn Reson Med **2014**;72:959-70

166. Semenza GL. HIF-1: upstream and downstream of cancer metabolism. Curr Opin Genet Dev **2010**;20:51-6

167. Harrison C, Yang C, Jindal A, DeBerardinis RJ, Hooshyar MA, Merritt M, *et al.* Comparison of kinetic models for analysis of pyruvate-to-lactate exchange by hyperpolarized 13 C NMR. NMR Biomed **2012**;25:1286-94

168. de Langen AJ, van den Boogaart VE, Marcus JT, Lubberink M. Use of H2(15)O-PET and DCE-MRI to measure tumor blood flow. Oncologist **2008**;13:631-44

169. Wilson CB, Lammertsma AA, McKenzie CG, Sikora K, Jones T. Measurements of blood flow and exchanging water space in breast tumors using positron emission tomography: a rapid and noninvasive dynamic method. Cancer Res **1992**;52:1592-7

170. Tang SY, Jiang WW, Chen HY, Bok R, Vigneron DB, Larson PEZ. A 2DRF pulse sequence for bolus tracking in hyperpolarized C-13 imaging. Magnet Reson Med **2015**;74:506-12

171. Young H, Baum R, Cremerius U, Herholz K, Hoekstra O, Lammertsma A, *et al.* Measurement of clinical and subclinical tumour response using [18 F]-fluorodeoxyglucose and positron emission tomography: review and 1999 EORTC recommendations. European journal of cancer **1999**;35:1773-82

172. Akaike H. A new look at the statistical model identification. IEEE transactions on automatic control **1974**;19:716-23

173. Burnham KP, Anderson DR. Model selection and multimodel inference: a practical information-theoretic approach. Springer Science & Business Media; 2003.

174. Shannon CE. A mathematical theory of communication. ACM SIGMOBILE Mobile Computing and Communications Review **2001**;5:3-55

175. Kullback S, Leibler RA. On information and sufficiency. The annals of mathematical statistics **1951**;22:79-86

176. Tofts PS. T1-weighted DCE imaging concepts: modelling, acquisition and analysis. signal **2010**;500:400

177. Parker GJ, Buckley DL. Tracer kinetic modelling for T1-weighted DCE-MRI. Dynamic contrast-enhanced magnetic resonance imaging in oncology: Springer; 2005. p 81-92.

178. Nagashima K. Optimum pulse flip angles for multi-scan acquisition of hyperpolarized NMR and MRI. J Magn Reson **2008**;190:183-8

179. Gordon JW, Milshteyn E, Marco-Rius I, Ohliger M, Vigneron DB, Larson PE. Mis-estimation and bias of hyperpolarized apparent diffusion coefficient measurements due to slice profile effects. Magn Reson Med **2016**

180. Chen H-Y, Larson PEZ, Gordon JW, Bok RA, Ferrone M, van Criekinge M, *et al.* 3D Dynamic Hyperpolarized 13C-Pyruvate MR Metabolic Imaging of Human Prostate Cancer. ISMRM. Singapore2016.

181. Gordon JW, Niles DJ, Adamson EB, Johnson KM, Fain SB. Application of flow sensitive gradients for improved measures of metabolism using hyperpolarized (13) c MRI. Magn Reson Med **2016**;75:1242-8

182. Marjańska M, Iltis I, Shestov AA, Deelchand DK, Nelson C, Uğurbil K, *et al.* In vivo 13 C spectroscopy in the rat brain using hyperpolarized [1-13 C] pyruvate and [2-13 C] pyruvate. J Magn Reson **2010**;206:210-8

183. Yen YF, Le Roux P, Mayer D, King R, Spielman D, Tropp J, *et al.* T2 relaxation times of 13C metabolites in a rat hepatocellular carcinoma model measured in vivo using 13C-MRS of hyperpolarized [1-13C] pyruvate. NMR in Biomedicine **2010**;23:414-23

184. Chen AP, Tropp J, Hurd RE, Van Criekinge M, Carvajal LG, Xu D, *et al.* In vivo hyperpolarized 13C MR spectroscopic imaging with 1H decoupling. J Magn Reson **2009**;197:100-6

185. Park I, Larson PE, Gordon J, Carvajal L, Chen H-Y, VanCriekinge M, *et al.* Dynamic Hyperpolarized 13C Metabolic Imaging of Patients with Brain Tumors. ISMRM. Hawaii, HI2017.

186. Eisenhauer EA, Therasse P, Bogaerts J, Schwartz LH, Sargent D, Ford R, *et al.* New response evaluation criteria in solid tumours: revised RECIST guideline (version 1.1). Eur J Cancer **2009**;45:228-47
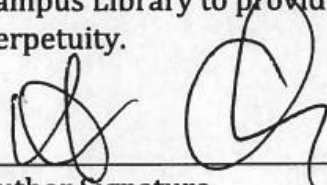
Publishing Agreement

It is the policy of the University to encourage the distribution of all theses, dissertations, and manuscripts. Copies of all UCSF theses, dissertations, and manuscripts will be routed to the library via the Graduate Division. The library will make all theses, dissertations, and manuscripts accessible to the public and will preserve these to the best of their abilities, in perpetuity.

Please sign the following statement:

I hereby grant permission to the Graduate Division of the University of California, San Francisco to release copies of my thesis, dissertation, or manuscript to the Campus Library to provide access and preservation, in whole or in part, in perpetuity.

_____   3/25/17
Author Signature   Date